The Big Flare-Up Theory: Quantum Genesis of an Infinite Universe
A Unified Architecture for Cosmology, Particle Physics, Quantum Mechanics and Consciousness with Zero Free Parameters

Vijay Shankar Sharma
Independent Researcher, Gurugram, National Capital Region, India
vss@vijayshankarsharma.com | ORCID: 0009-0001-9622-6121
DOI: 10.5281/zenodo.19149785
The author declares no conflict of interest and no funding was received for this research.

Abstract

The Big Flare-Up Theory (BFUT) is a unified physical framework developed across twenty-nine companion papers, linking cosmology, matter formation, particle physics, quantum mechanics, gravitation, light, time, extreme gravity, and consciousness through one physical substrate. The matter substrate, which the Big Flare-Up Theory calls the Spaticle Field, is assigned a measurable equilibrium density, $\rho s = 7.3 \times 10^{-27}$ kg/m³, and the framework develops a connected mathematical chain from condensation geometry to particle properties, fundamental constants, gravitational response and large-scale structure. The condensation functional $E(R)=A/R^2+BR^2+CR+D/R$ derives its coefficients from localisation, bulk displacement, three-core boundary geometry, and internal topological circulation. Its dimensionless minimum gives $R_0 = 1.27348221$, which is independently reconstructed from particle-sector constants. The same condensation and substrate chain yields the electron-proton mass relation, the reduced Planck constant, the fine-structure relation, the substrate stiffness and the universal propagation relation $c = \sqrt{(K_s/\rho s)}$. The covariant carrier equation F1-cov connects the substrate description to gravitation, finite deformation domains and the dark matter effects equation (DME) for organised rotating systems. The framework extends this structure to the strong and weak interactions, quantum-mechanical relations, particle masses, antimatter formation, light propagation, relativistic time, and finite-density compact objects. The DME acceleration scale is applied to 175 SPARC galaxies and to KiDS-1000 weak-lensing data, while the broader programme contains mathematical and non-mathematical predictions across cosmology and particle physics. The synthesis also develops physical treatments of major ΛCDM and Standard Model tensions, including dark-matter effects, dark-energy-like acceleration, the cosmological constant, the Hubble relation, early structure formation, matter-antimatter asymmetry, the proton-electron hierarchy, and singularity formation. Layer 1 presents the common architecture and the principal equations and results of the companion papers, while the individual papers provide their full derivations, simulations and detailed observational analyses.

Keywords: Big Flare-Up Theory; matter substrate, which the Big Flare-Up Theory calls the Spaticle Field; infinite universe; eternal universe; cosmological constant; dark matter; dark energy; gravitational sorting; Hubble tension; cosmic microwave background; quantum gravity unification; unified theory of physics; alternative cosmology; particle physics; quantum mechanics; consciousness science; galaxy rotation curves; condensation functional; gravitational vortex; electroweak unification; Higgs boson; zero free parameters; falsifiable cosmology; temporal eternity; spatial infinitude

Table of Contents

1. Introduction

Figure 1. The observational scope of the Big Flare-Up Theory spanning approximately forty orders of magnitude, from quantum-scale physics to the largest cosmological structures.

This paper is the master synthesis of an independent research programme comprising twenty-nine companion papers spanning cosmology, particle physics, quantum mechanics, gravitational physics, and the physical basis of consciousness. Its purpose is to present the common physical architecture, the principal equations, the major derived quantities, the observational applications, and the principal conclusions of the programme in one coherent account.

The synthesis distinguishes the common mathematical architecture from the domain-specific results. The consolidated mathematical and non-mathematical predictions are presented in Appendix B, while the consolidated mathematical and non-mathematical resolutions of ΛCDM tensions are presented in Appendix C.

The framework begins from the proposition that the physical substrate of space possesses measurable physical properties. BFUT identifies this matter substrate, which the Big Flare-Up Theory calls the Spaticle Field, and develops a measurable equilibrium density and a carrier description from which matter, forces and large-scale gravitational response are connected.

The standard ΛCDM framework provides a powerful account of many observations, while several observations and inferred quantities raise questions concerning uniqueness of interpretation, including galaxy dynamics, weak lensing, cosmic acceleration, the Hubble relation, early structure formation, and the physical status of dark sectors. BFUT addresses these questions through a substrate-based physical architecture and derives explicit quantitative relations that can be tested against data.

The companion papers develop successive parts of one substrate-based programme. Particle formation establishes the microscopic condensation structure; the interaction papers develop the emergence of the four forces; the gravitational papers develop the carrier field and finite deformation domains; the quantum papers connect the same carrier structure to quantum phenomena; and the cosmological papers apply the resulting quantities to observations across many scales.

The central mathematical chain is presented first in Section 1.1. The subsequent sections examine the cosmological premises, the observational questions addressed by BFUT, the predictions and tension resolutions, and the detailed contributions of the individual companion papers.

The paper is organised as a synthesis. Section 1.1 establishes the physical and mathematical architecture. Section 2 examines the principal ΛCDM interpretive tensions. Section 3 states the foundational cosmological premises. Section 4 develops the major cosmological mechanisms. Section 5 connects the framework to observations. Sections 6 and 7 consolidate predictions and ΛCDM tension resolutions. The later sections present the contributions of Papers 15 through 29, followed by the master formula and symbol references and the named appendices.

BFUT does not dispute the existence of the observed CMB temperature, light-element abundances, galaxy distributions, acoustic features, BAO measurements, galaxy rotations or lensing signals. The synthesis examines the physical interpretation assigned to these observations and asks whether the same observations can arise from the substrate-based mechanisms developed in the companion papers.

The purpose of the synthesis is to make the complete BFUT architecture readable as one connected programme: the foundational assumptions, the condensation mathematics, the substrate quantities, the force hierarchy, the governing carrier equation, the quantum and relativistic limits, the observational applications, the predictions, and the tension resolutions.

1.1 Physical and Mathematical Architecture

The Big Flare-Up Theory calls the matter substrate the Spaticle Field. This section presents the common mathematical and physical chain that connects the microscopic condensation construction to particle properties, fundamental interactions, gravitation, quantum mechanics, light, time, compact objects and the cosmological applications developed in the companion papers.

1.1.1 Condensation functional and the derivation of R_0

Paper 16 starts from the dimensionless condensation functional:

$$E(R) = A/R^2 + B\cdot R^2 + C\cdot R + D/R$$

The four coefficients are derived from the physical terms represented by the condensation model. They are not introduced as independent fitting parameters.

A, the localisation/kinetic coefficient: $A = \hbar^2/(2m\_eff)$

$m\_eff = \hbar/(c\cdot \ell\_model)$

Therefore $A = (\hbar^2/2) / [\hbar/(c\cdot \ell\_model)] = (1/2)\hbar c\ell\_model$

In the model-unit normalisation used for the condensation functional, $\hbar c\ell\_model = 1$, so $A = 1/2$ exactly. This is the radial localisation cost and is the model's analogue of the Schrödinger kinetic term $p^2/(2m)$.

B, the bulk displacement coefficient: $B = [\pi(d+R)^2 - 3\pi + A\_void] / [3\pi + A\_void/6] = 0.56308$

This coefficient is obtained from the geometric bulk-displacement construction, including the displaced-area term and the void-area contribution. It fixes the energetic cost of expanding the condensation beyond its equilibrium configuration.

C, the boundary coefficient: $C = -1/3$

The negative boundary term follows from the three-core geometry: three identical quark-class units share the expelled central region equally. The expelled precursor contribution therefore gives one-third per core, with the boundary-energy sign negative because the expulsion releases energy. C is exact in the model normalisation.

D, the internal-circulation coefficient: D = 1

The D/R term represents internal circulation support from the topological phase winding. In SI normalisation D = ħc, and the model-unit definition gives D = 1. The relation D = 2A also follows directly from the adopted normalisation.

A = 1/2,   B = 0.56308,   C = −1/3,   D = 1

The equilibrium radius is obtained by differentiating the functional with respect to the dimensionless radius R and imposing the stationary condition:

$$dE/dR = -2A/R^3 + 2BR + C - D/R^2 = 0$$

Multiplying by R^3 gives the equivalent polynomial equation:

$$2BR^4 + CR^3 - DR - 2A = 0$$

Substitution of the four coefficients gives:

$$1.12616R^4 - (1/3)R^3 - R - 1 = 0$$

The positive stable minimum is:

$$R_0 = 1.27348220802151$$

The second-derivative condition confirms that this stationary point is a minimum:

$d^2E/dR^2 = 6A/R^4 + 2B + 2D/R^3 > 0$

Thus R_0 is a dimensionless geometric result of the condensation functional. The P16 framework uses the proton charge radius to establish the physical SI length scale associated with the dimensionless geometry. P14 records the same functional and the minimum $R_0 = 1.27348$.

1.1.2 Independent validation of R_0

R_0 is also independently reconstructed from the particle-sector constants through the reduced Planck relation and the electromagnetic definition of α. The BFUT relation for the reduced Planck constant is:

$$\hbar\_vss = mp\ c\ rp/(\pi R_0)$$

The standard fine-structure definition is:

$$\alpha = e^2/(4\pi\varepsilon_0\hbar c)$$

Substitution of the BFUT expression for ħ into the fine-structure relation gives:

$$\alpha\_vss = e^2R_0/(4\varepsilon_0 mpc^2rp)$$

Solving for R_0 gives the independent reconstruction:

$$R_0 = 4\varepsilon_0 mpc^2rp\alpha/e^2$$

P27 reports this cross-check as $R_0 = 1.27348$ with an agreement of 0.00048% in the stated calculation. P23 likewise uses R_0 in the independent reconstruction of c.

1.1.3 From condensation geometry to ρ_s and particle quantities

The density chain connects the particle-sector condensation scale to the equilibrium density of the matter substrate, which the Big Flare-Up Theory calls the Spaticle Field. The P16 geometry establishes the condensation scale and the particle relations. P16 gives the interstitial energy and electron relation:

$$E\_unit = mpc^2/\pi$$

$$m\_e\_vss\ c^2 = E\_unit/(6\pi^4)$$

$$m\_e\_vss/mp = 1/(6\pi^5)$$

The three-core packing geometry also gives:

$$r\_q = r_p/(1 + 2/\sqrt{3})$$

$$V_{gap}/V_q = 0.0770$$

The interstitial gap energy is:

$$E_{gap} = E\_unit(V_{gap}/V_q) = 22.999\ \text{MeV}$$

The resulting BFUT-derived electron mass is:

$$m\_e\_vss = 0.511009\ \text{MeV}/c^2$$

The particle-sector gravitational-energy calculation then supplies the physical density scale. P78 gives the gravitational energy density as $u\_g = 6.56355667 \times 10^{-10}$ J/m³ and obtains the substrate density by dividing by c^2:

$$\rho_s = u\_g/c^2$$

$$\rho_s = 7.3 \times 10^{-27}\ \text{kg/m}^3$$

The publication value is the rounded equilibrium density:

$$\rho_s = 7.3 \times 10^{-27}\ \text{kg/m}^3$$

The extracted P78 text preserves the density derivation and its conversion from energy density to mass density. The publication value used in this synthesis is $\rho_s = 7.3 \times 10^{-27}$ kg/m³.

1.1.4 The connected derivation chain

The important feature is that R_0 does not stand alone. The condensation geometry feeds a chain of particle and field quantities. The principal relations are:

$$m\_e\_vss/mp = 1/(6\pi^5)$$
$$\hbar\_vss = mp\ c\ rp/(\pi R_0)$$
$$\alpha = e^2/(4\pi\varepsilon_0\hbar c)$$
$$c^2 = e^2R_0/(4\varepsilon_0 mprp\alpha)$$

$K_s = \rho_s c^2$
$a_s = c\sqrt{(G\rho_s/3)}$
$\mu_s^2 = 3G\rho_s/c^2$
$L_s = 1/\mu_s$

The same chain therefore reaches the electron mass, reduced Planck constant, fine-structure constant, speed of light consistency relation, substrate stiffness, galactic acceleration scale and carrier length. P27 explicitly records the ħ, α and R_0 cross-check chain.

1.1.5 Derivation and independent reconstruction of c

The mechanical propagation relation is:

$$c = \sqrt{(K_s/\rho_s)}$$

Equivalently:
$K_s = \rho_s c^2$

The independent numerical reconstruction uses quantities fixed or measured elsewhere in the programme:

$$c^2 = e^2R_0/(4\varepsilon_0 mprp\alpha)$$
$$c\_vss = 2.99791740 \times 10^8 \text{ m/s}$$
$$c = 2.99792458 \times 10^8 \text{ m/s}$$

The reported difference is 0.000239%. P23 explicitly describes this as a consistency reconstruction in which c is not used on the right-hand side.

1.1.6 Matter formation, antimatter and the stability filter

Antimatter is an essential part of the mathematical matter-formation chain. Paper 16 treats the formation process as a stability filter acting on excitations of the matter substrate.

The n = 4 partition analysis gives three relevant configurations. The 3+e configuration is the preferred stable configuration. The parameter-space analysis gives the following stability fractions:

3+e preference: 97.56% in 1D
3+e preference: 95.95% in 2D
3+e preference: 90.43% in 3D

The n = 4 configuration table gives the 3+e configuration a 97.56% share, compared with 2.16% for 2+2 and 0.28% for 4+0.

The formation interpretation is that the stable 3+e topology produces ordinary matter. The complementary unstable excitations collapse, and the rebound is identified in P16 as the antiparticle. Antimatter is therefore described as the cancellation wave associated with a failed excitation, not as a separately generated stable population. Matter and antimatter are circulation-topology inverses of the same underlying 3+e architecture, and complete annihilation corresponds to cancellation of the opposing topology.

The stability percentages are stated by dimensionality: 90.43% to 97.56% across the reported scans, with 97.56% for the n = 4 3+e configuration.

1.1.7 Emergence of the fundamental interactions

The strong interaction follows from compact three-core organisation. The confinement construction gives:

$$C\_s = F\_conf = 0.574 \text{ GeV/fm}$$

The electromagnetic coupling is:

$$\alpha = e^2/(4\pi\varepsilon_0\hbar c)$$

With the BFUT Planck relation substituted:

$$\alpha\_vss = e^2R_0/(4\varepsilon_0 mpc^2rp)$$

The reported BFUT value is α ≈ 1/137.037 compared with approximately 1/137.036.

The weak-sector relation is:

The P19 mixing quantity is an output of the independent W and Z resonance masses: $\sin^2\theta\_W\_vss = 1 - 256^2/(9\pi^8) = 0.23257$.

The synthesis associates this value with the bifurcation chirality geometry of the 3+e formation and the fixed handedness of the reconfiguration.

1.1.8 The governing covariant carrier equation and gravity

The common covariant carrier equation is:

$$g^{\mu\nu} \nabla_\mu\nabla_\nu(\delta\Psi) - 3\rho_s c^2\delta\Psi = (1/c^2)g^{\mu\nu} \nabla_\mu\nabla_\nu \Psi_{matter}$$

The finite deformation-domain equation is:

$$R_d = [3M/(8\pi\rho s)]^{(1/3)}$$

$$R_{eff} = R_d(1 + v_{rot}^2/c^2)^{(1/3)}$$

The DME relation is:

$$v^2(R) = v_b^2(R)[1 + a_s R/v_b^2(R)]^{(1/2)}$$

These equations connect the particle-sector density to the gravitational and galactic regimes. The P78 derivation gives the explicit carrier chain:

$$\rho_s \rightarrow \mu_s^2 = 3G\rho_s/c^2 \rightarrow \mu_s \rightarrow a_s = c\sqrt{(G\rho_s/3)}$$

No galaxy quantity enters the derivation of a_s.

1.1.9 Carrier relaxation and equilibrium scales

The relaxation representation is:

$$\tau_c\, \partial\Psi/\partial t + \Psi - L_{rlx}^2\nabla^2\Psi = K\cdot J[T_{mn}]$$

At the equilibrium density $\rho_s = 7.3 \times 10^{-27}$ kg/m³, the natural equilibrium carrier scales are:

$$L_{nat} = 45.17 \text{ AU}$$

$$\tau_{nat} = L_{nat}/c = 6.26 \text{ h}$$

1.1.10 Quantum mechanics, time, light and causality

The carrier equation is carried into the quantum regime. The programme connects it with the Schrödinger equation, the Born rule, spin-statistics, Pauli exclusion, wave-function collapse, superposition and entanglement. Angular momentum quantisation is expressed as:

$$L = n\hbar$$

The time relation is:

$$c^2 = v_{spatial}^2 + v_{internal}^2 + v_{grav}^2$$

$\eta = d\tau/dt = c_s/c_0$

The speed-limit relation is:

$$c = \sqrt{(K_s/\rho_s)}$$

Light and gravitational waves are treated as propagating disturbances of the same matter substrate, which the Big Flare-Up Theory calls the Spaticle Field, and therefore share the same limiting propagation speed.

1.1.11 Particle masses and configuration resonance predictions

The particle-sector chain gives:

$$m_p/m_e = 6\pi^5 = 1836.118$$

The H-class resonance follows from the P19 radial condensation invariant: $\lambda_{H\_vss} = 2\, A\, R_0 / \pi^2$, $v_{vss} = 6E_{unit}/\alpha_{vss}$, and $m_{H\_vss} = v_{vss}\sqrt{(2\lambda_{H\_vss})} = 124.75$ GeV/c².

The four-unit condensation gives two higher configuration-resonance predictions developed in P16A:

$m_{Shankar}\, c^2 = 2.60E_{unit} = 776.5$ MeV; $m_{BFUT}\, c^2 = 4.70E_{unit} = 1403.7$ MeV.

They are the 2+2 and 4+0 excitations above the persistent 3+1 condensation; P16A contains the full derivation and experimental correspondence.

1.1.12 Compact objects and finite density

The causal limit gives:

$$R_{max} = GM/c^2$$

$$\bar{\rho}_{max} = 3c^6/(4\pi G^3M^2)$$

The P16 condensation functional supplies the microscopic finite-condensation mechanism, while the causal calculation supplies the finite mean-density bound. P26 explicitly distinguishes this mean-density result from a claim about a uniform internal density profile.

1.1.13 Galaxy dynamics, weak lensing and cosmological tests

The same substrate-derived quantities are applied to galaxy rotation, weak lensing and cosmological observables. The Layer 1 synthesis reports 175 SPARC galaxies and the KiDS-1000 weak-lensing result using the common substrate framework. The P13 S8 programme gives a proof-of-concept rotational suppression from 0.832 to 0.7805, a 6.2% reduction.

1.1.14 The integrated mathematical chain

The mathematical foundation can therefore be represented compactly as:

condensation functional

↓

$$R_0 = 1.27348220802151$$

↓

3+e condensation geometry and particle relations

↓
m_e, $\hbar$, α, r_p and particle-sector energy relations
↓

$$\rho_s = 7.3 \times 10^{-27}\ \text{kg/m}^3$$

↓
K_s, c, μ_s, L_s, a_s
↓
F1-cov → gravitation → DDR/DME → galaxy and lensing predictions
↓
quantum, light, time and compact-object regimes

2. Critical Review of ΛCDM: Unresolved Contradictions

This section does not propose to provide an exhaustive critique of the Big Bang Theory. It identifies the specific contradictions most directly relevant to the motivations for BFUT.

2.1 The Singularity and Its Location

Foundational Ontology: ΛCDM vs. BFUT

	ΛCDM	BFUT
Universe Origin	Finite; singular Big Bang 13.8 Gyr ago.	**Eternal; Big Flare-Up as a local ignition in an infinite, structured substrate.**
Vacuum State	Empty geometric spacetime with vacuum energy crisis (10^121 discrepancy).	**A physical medium (Spaticle field) at equilibrium density.**
Spatial Extent	Finite or undefined; inflationary smoothing required.	**Logically and physically infinite; no boundary.**
Cosmological Constant (Λ)	Assumed dark energy accelerating expansion.	**The derived geometric signature of the Spaticle field's density.**
Dark Matter	Undiscovered particulate halos.	**The non-particulate Spaticle field itself.**

Figure 2. Comparison of the conceptual foundations and explanatory frameworks of ΛCDM and the Big Flare-Up Theory.

The ΛCDM model does not require the spatial universe itself to be finite. The singularity issue concerns the past boundary of the cosmological solution, not a point located in today's spatial manifolD's criticism is therefore directed at the interpretation of a literal point-like origin and at claims that all of present space must have emerged from such a point. The standard response that the Big Bang occurred everywhere is a statement about the geometry of the early solution, not a proof that the present universe has a finite spatial boundary. BFUT instead argues independently that the physical universe is spatially infinite and has no terminal boundary.

2.2 The Hubble Constant: Variability Inconsistent with a True Constant

A physical constant is expected to be stable across independent measurement methods and epochs. The Hubble constant (H_0) has varied from Hubble's original estimate of approximately 500 km/s/Mpc [23] through revisions to approximately 180, 75, and 50-55 km/s/Mpc over subsequent decades, to the current range of 67-74 km/s/Mpc depending on measurement methodology (Riess et al., 2019; Planck Collaboration, 2020). The variation is important because H_0 is an expansion-rate parameter, not a fundamental constant in the same sense as c. The reciprocal $1/H_0$ is the Hubble time, a characteristic timescale, not in general the age of the universe. At Hubble's original value of 500 km/s/Mpc, the Hubble time is approximately 2.0 billion years, illustrating why the early estimate was incompatible with the independently established age of Earth. At approximately 50 km/s/Mpc, the Hubble time is approximately 19.6 billion years. The variation from the highest to lowest historical values therefore changes the characteristic Hubble timescale by nearly a factor of ten. The current Hubble Tension - a 4-6 σ discrepancy between Planck CMB-derived values and local distance-ladder measurements - has been described as potentially requiring new physics beyond the standard model. BFUT proposes that the variation reflects the fact that H_0 is an emergent statistical property of a gravitationally sorted galaxy population and not a universal expansion constant.

instability reflects not measurement error but the possibility that a single universal expansion parameter is being inferred from a population whose kinematics depend on environment, scale, and dynamical history. Note added in proof (March 2026): Two peer-reviewed papers published in Astronomy & Astrophysics (Wagner, Benisty & Karachentsev, 2026; Benisty et al., 2026) report an additional independent measurement of the Hubble relationship using galaxy-group infall dynamics applied to the M81/M82 and Centaurus A/M83 groups, obtaining $H_0 = 63 \pm 6$ km/s/Mpc. These results add to the methodological spread among local, distance-ladder, and CMB-derived determinations and are consistent with BFUT's Prediction 5, which holds that the observed Hubble relationship is an emergent statistical property of gravitationally sorted galaxy populations. The two studies also report group dynamics consistent with the visible baryonic mass of the principal member galaxies without requiring a dark-matter halo in the systems analysed, consistent with BFUT's Prediction 4.

2.3 The Local Exception Defence: An Unfalsifiable Mechanism

The ΛCDM model's principal response to observations of galactic approach (notably Andromeda at approximately 110 km/s) and galaxy-galaxy collisions is to classify them as 'local exceptions' - regions where gravitational interactions override the universal expansion. This defense has never been accompanied by a definition of the spatial scale at which 'local' ends and 'universal' begins. A scientific theory must be falsifiable [34]. A defense mechanism capable of absorbing any contradictory observation without a defined application boundary is unfalsifiable. The observation of hundreds of galaxy collisions across the observable universe - documented extensively by the Hubble Space Telescope and JWST - makes the 'local exception' classification increasingly untenable without a defined boundary.

2.4 Recession Velocity Exceeding the Speed of Light

The Hubble radius is not, by itself, a causal horizon. In standard cosmology, regions beyond the Hubble radius can in principle remain causally connected depending on the expansion history, while the relevant causal boundaries are defined by particle and event horizons. BFUT therefore does not treat the Hubble radius as a boundary of physical existence. The empirical question is instead whether the observed recession relation requires metric expansion at all.

2.5 Dark Energy: Observational Basis Under Challenge

The evidence for cosmic acceleration, and therefore for dark energy, originates primarily from Type Ia supernova observations by Perlmutter et al. (1999) and Riess et al. (1998). A 2019 peer-reviewed paper by Colin, Mohayaee, Rameez, and Sarkar, published in Astronomy & Astrophysics, reanalyzed the Joint Light-curve Analysis (JLA) catalogue of 740 Type Ia supernovae and found that the deceleration parameter exhibits a significant dipole component

(3.9σ statistical significance) aligned with the CMB dipole direction. The paper's conclusion is direct: 'the cosmic acceleration deduced from supernovae may be an artefact of our being non-Copernican observers, instead of evidence for a dominant component of dark energy in the Universe' (Colin et al., 2019, p. L13). This finding has not been refuted in the subsequent peer-reviewed literature. The observational foundation of dark energy - and therefore of the Nobel Prize awarded for its discovery - rests on data that peer-reviewed analysis suggests may reflect local bulk flow.

2.6 The Non-Detection of Dark Energy and Dark Matter

Dark energy and dark matter together comprise approximately 95% of the proposed content of the universe (Planck Collaboration, 2020). Neither has been directly detected. Dark matter searches including the Large Underground Xenon (LUX) experiment, the XENON programme, and the Cryogenic Dark Matter Search (CDMS) have produced null results. Dark energy has no confirmed direct detection of any kind. A theoretical framework in which 95% of the proposed content remains undetected after decades of dedicated experimental effort warrants serious scrutiny.

2.7 The James Webb Space Telescope and Early Galaxy Formation

JWST observations have identified massive, morphologically mature galaxies at redshifts $z > 10$, corresponding to less than 500 million years after the putative Big Bang (Labbé et al., 2023; Curtis-Lake et al., 2023). These galaxies exhibit stellar masses, star formation histories, and structural complexity inconsistent with the timescales available for structure formation in the ΛCDM model. Multiple authors have noted that these observations challenge the standard model of hierarchical structure formation (Steinhardt et al., 2016; Boylan-Kolchin, 2023). In BFUT, mature galaxies at any distance are predicted, not surprising, because the universe has had infinite time for structure formation at all locations.

2.8 The Balloon and Raisin Bread Analogies

The Big Bang framework invokes two analogies to explain why every galaxy recedes from every other without a centre: a balloon being inflated, and a loaf of raisin bread being baked. These are presented not merely as illustrations but as evidence. Both fail on their own physical terms.

Both analogies require a centre. A balloon expands because air pressure pushes outward from a central cavity. Every point on the surface scales outward from the same single centre. The universe, by the Big Bang's own claim, has no centre. The analogy requires the very thing the theory denies. Every observer on such a surface could identify where the centre is by the direction of the expansion force acting on them. No such directionality is observed.

A real balloon has a deflated initial state - collapsed, folded, crumpled. The analogy always begins already inflated to a convenient smooth state, hiding the chaotic initial condition that corresponds to the post-Big Bang epoch.

Galaxy orientations are fixed in space. A spot on a balloon rotates with the rubber surface as it inflates. Real galaxies do not. If orientations are fixed, the apparent angles between galaxies must change as the balloon carries their positions to new locations on the curved surface. No such systematic angle change is observed, and no defender of the analogy has addressed this.

Neither analogy can expand indefinitely. Every balloon bursts. The analogy collapses at the moment it needs to be most convincing.

An observer on the balloon surface with sensitive instruments would find a centre. The expansion force acts outward from a single interior point. Every observer on the surface performing the same measurement would point to the same location. The centre is physically detectable. There would be a direction in which, looking far enough, you would find nothing. In the real universe, galaxies are observed in every direction at every distance to the limits of every instrument ever built. No direction terminates in emptiness. No detectable centre exists. No observer has ever identified a direction of expansion force pointing to a common source.

The nested balloon escape route fails on three independent counts. First, all layers still share the same centre - the centre problem is merely surrounded by more balloons. Second, layers expanding at the same speed produce no inter-layer recession; layers at different speeds produce an asymmetric recession pattern depending on which direction you look. Isotropic recession is observed. Third, discrete layers require boundaries that would appear as voids in the galaxy distribution. No such gaps are observed.

The balloon surface analogy is a pedagogical construction, not a literal embedding of cosmological space in a higher-dimensional Euclidean space. A closed curved space can be finite and boundaryless without being a wormhole or providing a traversable shortcut through an interior. The analogy therefore cannot by itself establish either a physical centre or a physical boundary; its value is limited to illustrating how distances can change without a preferred point on the surface.

The "finite but unbounded" claim is exposed by the hamster analogy. If an intelligent hamster inside a box asks what lies beyond the wall, and one places the hamster on a wheel and says it can keep walking forever, the original question has not been answered. Endless motion on a loop does not prove the enclosing space is boundaryless.

Finally, every deep field image shows galaxies oriented in every possible direction with no systematic pattern. A single central pressure source cannot produce matter oriented in every direction randomly. This constitutes independent observational falsification of the balloon analogy on its own physical terms. See also Section 2.9.

2.9 Galaxy Orientations: A Visible Proof Against a Single Origin

Every deep field image produced by the Hubble Space Telescope and the James Webb Space Telescope - images showing hundreds or thousands of galaxies in a patch of sky smaller than a grain of sand held at arm's length - displays the same observable fact: galaxies are oriented in every possible direction in three-dimensional space. Some are face-on, presenting their full spiral disc. Some are edge-on, appearing as thin lines. Most are tilted at every conceivable angle between these extremes. No two orientations are the same. No preferred plane is detectable. No systematic bias exists in any direction. This observation has been in plain sight in every deep field image ever taken. It has never been framed as the direct logical argument it constitutes against a single-point origin. A single-point origin imposes a geometry. Any geometry imposes a preferred orientation. If the universe expanded from a single point outward in all directions - as the Big Bang proposes - that expansion carries a directionality. Matter ejected from a common origin and expanding outward together should show some statistical pattern in how it orients over time. The expansion surface, the direction of flow, the common origin - any of these would leave a detectable imprint on the large-scale orientation statistics of galaxies. None is observed. Galaxy orientations are isotropic to the limits of every instrument ever used to measure them. Furthermore, no rule has ever been found - and none can in principle be found - that predicts under what conditions a given galaxy will be oriented in a given direction. Orientation is determined entirely by local gravitational history: the specific directions from which matter happened to arrive at that location over the lifetime of that galaxy. Each galaxy's orientation is the unique product of its own local accumulation history. This is precisely what an infinite eternal universe with no origin point predicts - and precisely what a universe expanding from a single point does not. The second implication of isotropic galaxy orientations is equally significant. If any net force or gravitational pull were operating at universal scale - pulling or pushing from any preferred direction - it would leave a detectable signature in galaxy orientations. Galaxies everywhere would be statistically nudged toward some common alignment over cosmic time. No such alignment is observed. Isotropic orientations are therefore independent observational confirmation that no universal-scale force operates which removes one of the theoretical motivations for dark energy entirely. In BFUT, isotropic galaxy orientations are the expected outcome. In an infinite universe with no origin point, matter accumulates from all directions at every location, producing rotational axes that point in every direction with equal probability. The orientation of any galaxy is the frozen record of its unique local gravitational history. There is no pattern because there is no common origin to impose one. The balloon analogy fails on three additional physical observations that can be stated together. First, in a real balloon the spots themselves expand as the rubber stretches. A spot that is one centimetre wide becomes two centimetres wide as the balloon doubles in size, because the spot is painted on the rubber and the rubber carries it. If galaxies are the spots and space is the rubber, galaxies should grow as space expands. They do not. Observed galaxy sizes do not simply scale with a balloon surface in the manner required by the literal analogy. This is a qualitative objection to treating the balloon as a physical model of space. Second, galaxies maintain their orientations, as already established above. Third, distances between objects in the local region are not measurably increasing, which the standard model addresses by invoking local gravity as an exception to universal expansion. However no boundary has ever been defined for where local gravity ends and universal expansion begins. BFUT treats the absence of a specified transition boundary as an unresolved modelling question that should be stated explicitly. All three

observations, fixed galaxy sizes, isotropic orientations, and the undefined local exception, point to the same conclusion: the balloon is not a physical analogy for the universe. It is a convenience that fails every time it is tested on its own terms.

The observed diversity of galaxy orientations argues against more than just one simplistic expansion picture. If galaxies were expanding outward from a single pressure center, or being coherently pulled toward some universal external attractor, or being pushed in a common direction by some large-scale external agency, then sufficiently large samples should show statistically recognizable alignment signatures in their orientations, angular momenta, or structural axes. No such universal alignment is observed.

The absence of a common directional imprint therefore argues against all three simplified pictures at once: no single internal pressure point of origin, no universal pull from some cosmic edge or corner, and no universal push from outside. This is stronger than merely saying that there is no obvious center of expansion. It means that the visible large-scale distribution also lacks the kind of systematic orientational memory that such common forcing would be expected to leave behind. The observational diversity of orientations is therefore more naturally consistent with long-timescale local formation, recurrent flare-up histories, and structurally independent development across an infinite universe than with any single universal one-time forcing geometry.

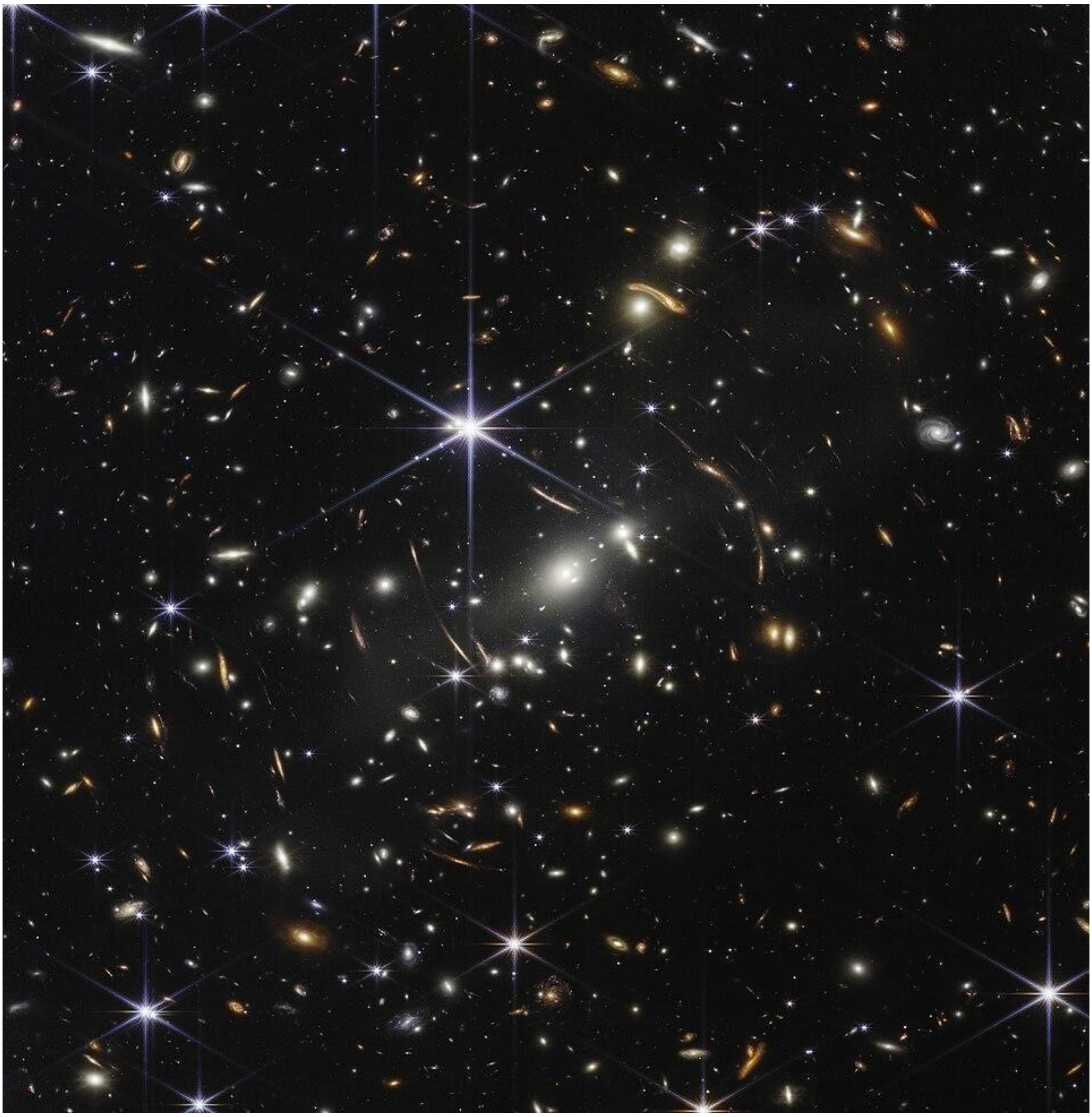

Figure 3: JWST First Deep Field - Galaxy Cluster SMACS J0723.3-7327 (NASA/ESA/CSA/STScI, 2022). Thousands of galaxies are visible in this image covering a patch of sky the size of a grain of sand held at arm’s length. Observe that the galaxies are oriented in every possible direction - face-on, edge-on, and every angle between. No preferred orientation exists. No rule predicts why any galaxy faces the direction it does. This constitutes independent falsification of the balloon analogy (Section 2.8) - a single central pressure source cannot produce matter oriented in every direction randomly. It is also the expected outcome of an infinite eternal universe with no common origin point (Section 2.9).

2.10 The Universal Spiral: Why Everything in the Universe Spins

BFUT proposes that rotation is ubiquitous across the observed structures discussed in this section. Stars, planets, galaxies, galaxy clusters, the filaments of the cosmic web - all rotate. This is not a coincidence requiring special explanation.

It is a necessary physical consequence of two facts operating together: that matter accumulates gravitationally from multiple directions simultaneously, and that the universe is infinite. When hydrogen atoms first began to coalesce under gravity, they attracted neighbouring atoms from multiple directions. Those approach trajectories are never perfectly collinear - matter arrives from slightly different angles, imparting net angular momentum to the accumulating mass. This is the same mechanism responsible for the rotation of every protoplanetary disc, every star, every galaxy. The initial rotation begins almost immediately after the first gravitational accumulation. Within the BFUT infinite-universe model, once rotation is established, the absence of a cosmological boundary and the conservation of angular momentum provide the proposed reason for its persistence. There is no boundary to absorb angular momentum. There is no friction at cosmological scale sufficient to dissipate it. Angular momentum is conserved. Rotation, once initiated, is permanent. The infinite universe is the reason everything spirals. In a finite universe, it is at least theoretically possible to travel in a straight line until encountering a boundary. In an infinite universe, straight-line travel is impossible in practice over sufficient timescales - the traveller will always, eventually, encounter another gravitational body. That encounter deflects the trajectory. Deflection accumulated across infinite time and infinite space means every path curves. BFUT proposes that repeated gravitational deflections make long-term straight-line trajectories dynamically uncommon. The spiral is not a special condition of matter in the universe. It is the only stable long-term state available to matter in an infinite universe. This argument also explains the absence of any preferred spin direction in the universe. Just as gravitational sorting produces a local Hubble recession pattern without it constituting a universal law - an observer in a different region would see a different local pattern - any apparent local preferred spin axis is a local statistical outcome of the particular gravitational history of this observable region. An observer in a sufficiently distant region would find a different local preferred axis, or none at all. Zoom out to a sufficiently large-scale and spin directions are isotropic. This is what an infinite eternal universe predicts. It is what BFUT predicts. A single-point origin with a preferred expansion direction cannot account for it. There is a further and stronger argument for why everything in the universe rotates, one that goes beyond the mechanics of angular momentum imparted at formation. Over infinite time, straight-line motion is the least stable configuration available to any body in infinite space. A body moving in a straight line will inevitably encounter another body. If it survives the collision it is deflected. Repeated deflections curve the trajectory. A body that does not find a stable orbital or rotational configuration will continue colliding until it is absorbed into a larger body that has. Bodies on stable orbital and rotational paths persist. Bodies on straight trajectories do not. BFUT therefore interprets rotational and orbital configurations as dynamically persistent configurations over cosmological timescales. Over cosmological timescales, straight-line motion is selected against and rotational motion is selected for, not by any force or intention, but by the simple mathematics of survival in infinite space. Everything in the universe spins because spinning and orbiting bodies endure and straight-moving bodies do not. This argument also connects directly to the gravitational sorting mechanism of Section 4.3: the same selection process that eliminates galaxies on collision courses and leaves predominantly divergent survivors also eliminates straight-moving matter and leaves predominantly rotating survivors. Gravitational sorting and universal rotation are two expressions of the same underlying principle operating at different scales across infinite time.

2.11 Dark Matter as a Claimed Necessity for Cosmic-Web Formation

The synthesis is accompanied by the standard 106-entry Spaticle Field Applications Appendix, which records the independently meaningful derived results and applications of the framework.

3. Foundational Premises of the Big Flare-Up Theory

A Universal Principle Underlying BFUT

Before presenting the four foundational premises of BFUT, it is necessary to name the universal principle of which this theory is the first formal cosmological demonstration. The Big Flare-Up Theory is not an isolated proposal about the origin of the universe. It is the cosmological expression of a law that operates at every scale of existence - from the behaviour of subatomic matter to the structure of the universe, from the mechanism of biological evolution to the origin and expression of human emotion. That law is stated here for the first time:

The author proposes the following as the universal principle underlying BFUT and the broader framework: wherever stable or predictably unstable conditions exist, matter - which is conscious at every scale - will manifest in a more complex form, driven by its fundamental drive to propagate and perpetuate itself. It fires at every scale, at every moment, wherever the conditions are met.

Its corollary follows directly from the same principle.

Every star igniting in the modern universe is the same law that produced the Big Flare-Up, firing again at a new location and time. Every fusion event, every gravitational vortex, every accumulation of matter from the Spaticle field is the same threshold being crossed, the same law expressing itself. The Big Flare-Up was singular not because its physics was unique - those physics operate continuously across the infinite universe to this day - but because the condition that produced it, a universe that had never before experienced fusion energy, can never exist again. The law is eternal. Its first firing was unrepeatable.

3.1 Premise 1: The Universe Is Spatially Infinite

The spatial infinitude of the universe is not assumed in BFUT but derived from two independent logical arguments.

The BFUT boundary argument is not a general mathematical theorem that every finite space must have a boundary, because closed boundaryless manifolds exist. It is instead a physical argument against a finite universe having a genuine terminal boundary of physical extension. Consider any finite region of ordinary physical space - a room, a building, a city. Its apparent boundaries are surfaces within a larger space, and space continues beyond them. BFUT therefore argues that a literal physical terminus of the entire universe would require a physically meaningful distinction between space and non-space at that terminus. The conclusion is a physical claim about the universe represented by BFUT, not a theorem about all possible finite manifolds.

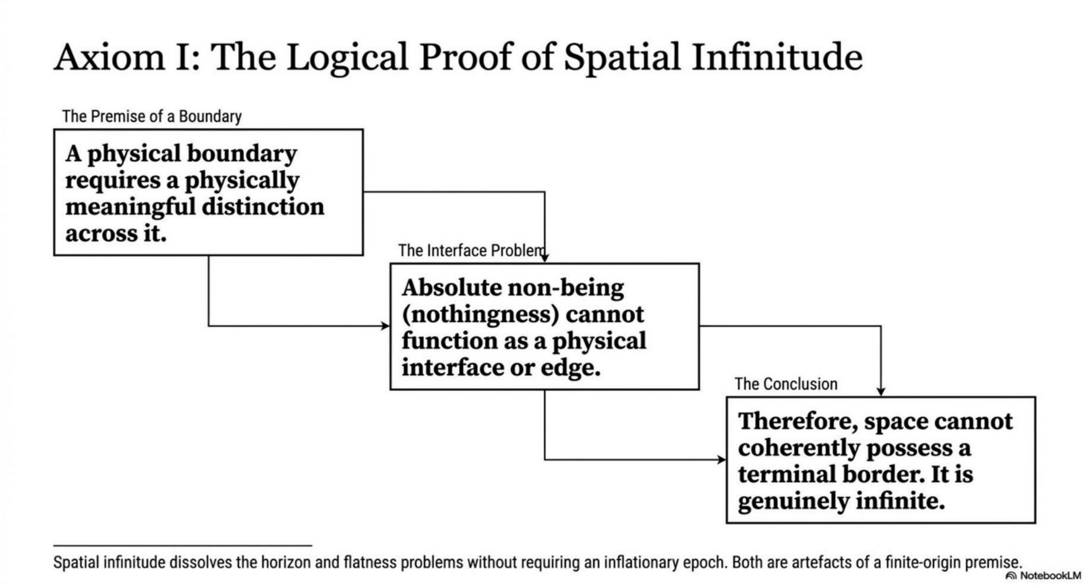

Figure 4. Logical arguments supporting spatial infinitude and the absence of a universal boundary.

- every planet, moon, star, galaxy - is itself inside space, with space continuing on every side of it. At every scale, in every direction, the same observation applies: whatever appears to bound a region of space is itself inside space. Space continues beyond it. BFUT's physical boundary argument therefore concerns a boundary that would constitute a genuine terminus of physical extension. This argument should not be stated as a general mathematical theorem that every finite space has a boundary: closed, boundaryless manifolds exist. Nor does positive spatial curvature require an embedding in a higher-dimensional physical space. BFUT's claim is instead that a physical terminus of space would require a physically meaningful boundary condition, and that no such boundary has been identified or derived within the BFUT framework.

3.1.1 The Vacuum Stability Argument: A Physical Illustration

The logical argument above establishes BFUT's boundary objection. The following calculation is only a physical illustration of what a material boundary would have to withstand; it is not an independent proof. If a finite vacuum region were enclosed by a physical boundary, the boundary would have to provide the required stress balance against the interior state. The calculation therefore illustrates the physical burden imposed by a finite-boundary model and does not assume that every finite manifold must have an external medium or pressure.

The illustrative calculation shows that assigning a physical boundary creates an additional stress-balance problem and does not remove it. Lower assumed stresses change the numerical requirement but do not supply a derived physical boundary condition. The conclusion that the universe is spatially infinite in BFUT rests on the independent boundary argument and the observational programme developed in Paper 5. The darkness of the night sky is addressed separately in Section 5.6.

3.2 Premise 2: The Universe Is Temporally Eternal

Spatial infinitude does not mathematically imply temporal eternity. BFUT treats temporal eternity as a separate foundational claim, supported by continuity arguments concerning the absence of a privileged initial epoch and by the ongoing matter-formation process described below. A universe that has always existed has no initial boundary in time within the BFUT framework, so the origin question is replaced by the question of how matter and structure evolve within the underlying substrate. Gas clouds of varying densities have been observed across the universe at stages ranging from diffuse clouds to active collapse and stellar ignition. Taken together, these observations are consistent with an ongoing accumulation and ignition sequence. The temporal-eternity argument and the spatial-infinitude argument should therefore be regarded as complementary but logically distinct claims.

specific prediction about interstellar matter density, developed in full in Section 7 as Prediction

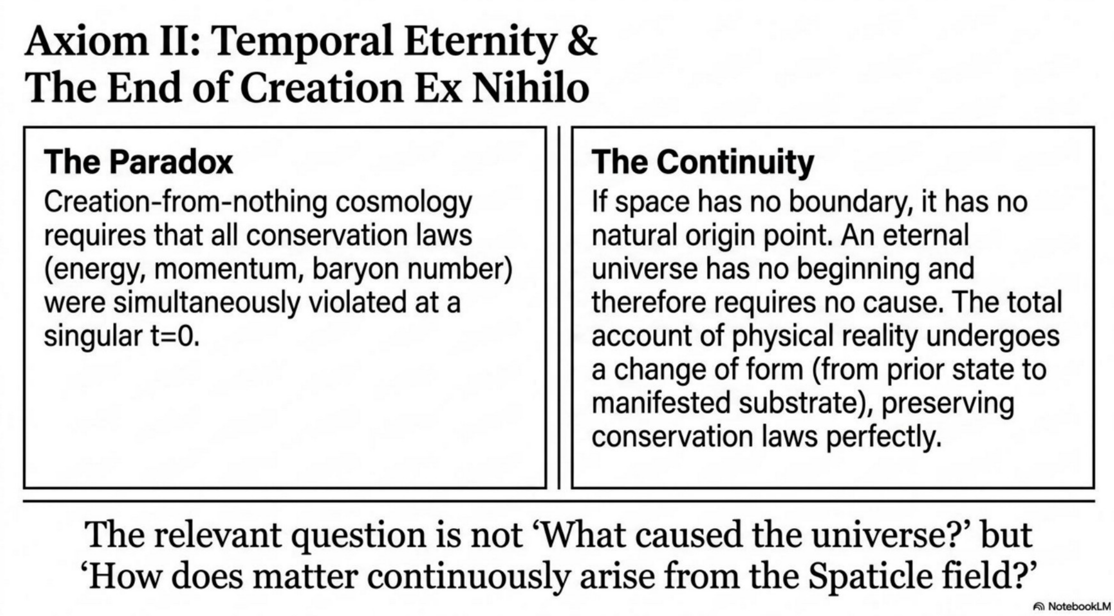

Figure 5. The eternally existing universe prior to the Big Flare-Up event.

6. This does not imply that the universe is static_vss proposes a universe that is infinite and eternal but continuously evolving - dynamically active at all times and all locations, with no privileged epoch.

3.3 Premise 3: Matter Arises Through Quantum Fluctuations in the Spaticle Field

Einstein's general relativity - the most precisely confirmed theory in modern physics - shows that space warps, stretches, and transmits gravitational waves. A geometric abstraction cannot do any of these things. Space must therefore be composed of something physical. BFUT designates that physical substrate the Spaticle field. The full argument is developed in Section 4.6.

Quantum fluctuations - temporary deviations in energy levels associated with quantum uncertainty - occur throughout quantum fields. BFUT proposes that a subset of fluctuations can enter stable condensation states and persist. If the stable-condensation rate remains non-zero over arbitrarily long times and the process continues to sample independent opportunities, the expected number of successful events grows without bound. This supports eventual occurrence in the BFUT framework, but the mathematical statement should not be phrased as an unconditional theorem that any non-zero probability automatically implies certainty without specifying the stochastic process and its persistence over time. The subsequent condensation mechanism is developed in Paper 16 [P16].

A direct question must be acknowledged: quantum field theory describes virtual particle-antiparticle pairs that annihilate almost immediately after formation. The physical mechanism by which occasional fluctuations in the Spaticle field produce stable, persistent matter is not fully specified in this paper. It is proposed as the mechanism most consistent with the observed population of gas clouds at every stage of accumulation, and with the Voyager plasma density finding described in Section

The argument that non-zero probability over infinite time becomes certainty applies to any quantum fluctuation process operating in any physical substrate, and it does not depend on the specific nature of the Spaticle field. The Spaticle field therefore plays two distinct roles in BFUT, and these roles should be distinguished clearly. The first role is the role established by confirmed physics: space has physical properties: it warps, transmits waves, and interacts with matter. This requires a physical substrate. BFUT names that substrate the Spaticle field. This role does not depend on any unconfirmed mechanism. The second role is as the medium in which quantum fluctuations

produce stable persistent matter through the condensation mechanism established in Paper 16 [P16]. The first role stands independently of the second. The Spaticle field is the necessary physical substrate of space and time established by confirmed general relativity regardless of which mechanism explains persistence, and the condensation functional of Paper 16 provides that mechanism directly. The two roles are connected: matter arising from quantum fluctuations in the physical substrate of space is the natural and parsimonious proposal, and the foundational claim about the Spaticle field's existence does not depend on any further confirmation beyond the derivation already given.

3.4 Premise 4: Nuclear Fusion Drives Continuous Stellar Formation

Matter accumulating in gravitationally dense regions eventually reaches the temperature and pressure conditions for nuclear fusion - the process by which hydrogen nuclei fuse to form helium and heavier elements, releasing energy. Gravitational collapse is the immediate mechanism that forms stellar structures; fusion begins after sufficient compression and heating. In BFUT, the first fusion ignition in a universe that had never before experienced fusion energy initiated the Big Flare-Up cascade, while subsequent fusion events continue to provide energy and can trigger secondary ignition in neighbouring matter. The distinction is important: fusion does not replace gravitational collapse as the local formation mechanism, but it is the sustaining and cascade-driving process in the BFUT picture.

Subsequent individual stellar ignitions continue to the present day and are directly observable as active stellar nurseries, but these are ordinary local events, not repetitions of the Big Flare-Up.

4. Core Mechanisms of the Big Flare-Up Theory

4.1 The Big Flare-Up: First Ignition Across Infinite Space

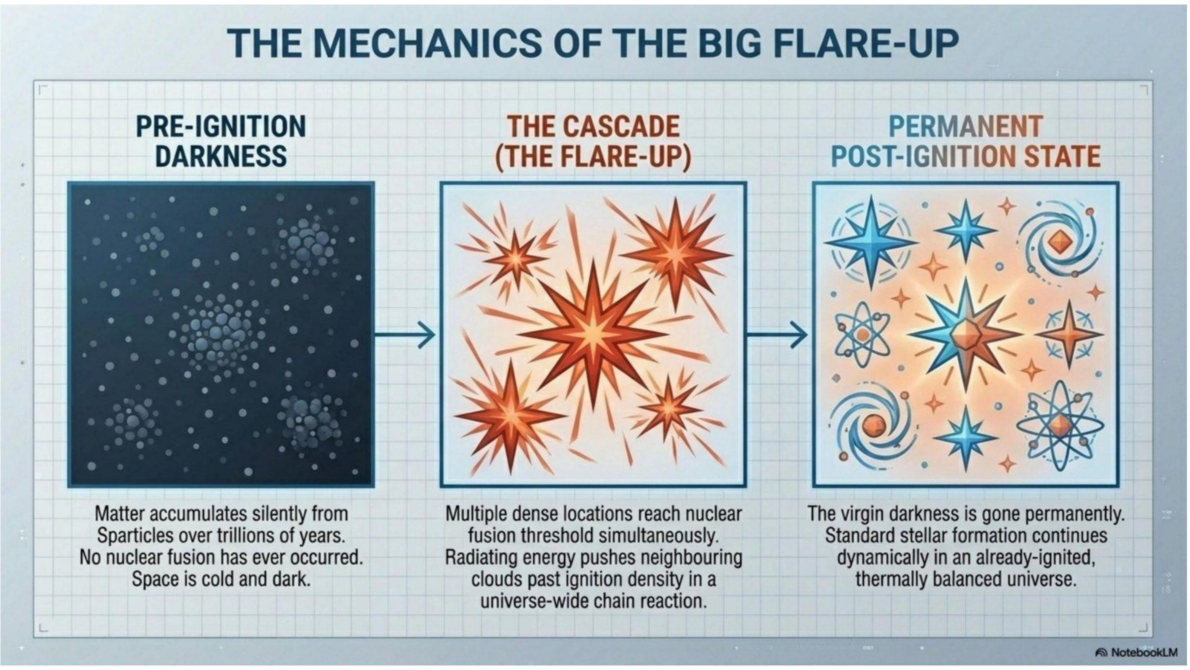

Figure 6: The three phases of the Big Flare-Up. Pre-Ignition Darkness: matter accumulates silently. The Cascade: multi-point ignition fires when density thresholds are crossed. Post-Ignition Equilibrium: the permanent current state of the universe.

In BFUT, the question of cosmic origin is reframed from 'what caused the Big Bang?' to 'when did matter first ignite in nuclear fusion, and what happened when it did?' The answer to that question is the Big Flare-Up - a singular event whose nature and mechanism are fundamentally different from any stellar ignition occurring today. Before the Big Flare-Up, the universe contained only the Spaticle field and the matter that had gradually accumulated from quantum fluctuations over a span of time far exceeding any timescale in current cosmology - potentially trillions or quadrillions of years, far exceeding any timescale in the current standard model. This was a universe in complete darkness. No fusion had ever occurred anywhere. No fusion energy existed anywhere. Matter sat in accumulating clouds across infinite space, growing denser, but none of it had yet crossed the ignition threshold. Then, at multiple locations distributed across the infinite universe, wherever matter had first reached ignition density, conditions crossed the threshold for nuclear fusion. Fusion ignited. Energy was released - the first fusion energy that had ever existed in the universe. That energy radiated outward into neighbouring clouds. Here is what made the Big Flare-Up singular: those neighbouring clouds, some of which had not yet reached ignition threshold on their own, were pushed across threshold by the incoming fusion energy, causing secondary ignitions that propagated the flare-up outward in a cascading chain reaction. The precise timing of the Big Flare-Up is not known and cannot be determined from within the current universe using existing observations. This is not a weakness of the theory - it is an expected consequence of the scale involved. The Big Bang framework similarly cannot explain what preceded its own proposed origin or what caused it. The timing of the Big Flare-Up is, however, derivable in principle. If sustained observational programmes measuring matter density at fixed coordinates in multiple molecular clouds establish an average accumulation rate, that rate can be extrapolated backward through

The timing is a derived target that can be constrained by the Jeans-instability and ignition conditions once the relevant physical inputs are specified. Prediction 6 in Section 6 concerns the persistence of the 2.725 K CMB temperature at greater observational depth, not the timing of the first ignition. The first-ignition epoch is therefore treated separately from Prediction 6.

A clarification of scope is essential here. BFUT does not treat luminous flare-up phases as unique once-only events confined to the distant past. Such flare-ups are recurrent processes in an infinite and eternal universe. They may occur at many different locations, at many different times, on many different scales, and under many different local conditions. Some occurred long before the epoch the standard model contemplates. Some are occurring now. Every stellar ignition in every nursery across the observable universe is a local flare-up in this sense: the same threshold physics and the same release of energy into neighbouring clouds. The Big Flare-Up was singular not because its local physics was unique, but because it marked the first universe-wide transition from a state with no prior fusion history to one in which fusion had become an ongoing physical process. The local ignition times are not globally simultaneous and propagate through finite-speed physical interactions.

4.2 Matter Accumulation and Rotational Structure Formation

In BFUT, matter accumulation in an infinite universe is necessarily accompanied by rotational structuring. Given sufficient time, repeated interactions among gas clouds, stars, compact objects, and larger gravitational aggregates do not preserve perfect radial symmetry. Instead, angular momentum is generated, exchanged, concentrated, and retained. This makes rotation a generic long-term outcome of matter aggregation.

This rotational hierarchy is not a decorative by-product of structure formation but one of its primary organizing principles. As matter accumulates over long durations within a persistent gravitational environment, even slight asymmetries in infall and interaction are amplified into orbital motion, angular momentum segregation, and nested rotational structures. Clouds do not merely collapse; they sort, spin, flatten, fragment, and reorganize. This naturally produces disks, vortices, filaments, rotating substructures, and bound systems at multiple scales without requiring a single explosive origin.

4.3 Gravitational Sorting: The Mechanism of Apparent Galactic Recession

The observation that most galaxies exhibit redshifted spectra consistent with recession velocity proportional to distance [23] is the primary empirical basis for universal expansion. BFUT proposes an alternative mechanism: gravitational sorting, operating across cosmic timescales, producing a universe in which surviving galaxies are predominantly in non-intersecting trajectories - and therefore predominantly moving apart.

4.3.1 The Solar System Analogy

The solar system provides a directly observable demonstration of gravitational sorting. Early in solar system formation, planetesimals and proto-planets occupied a wide range of orbital planes and inclinations. Objects on intersecting orbits collided, merged, were deflected, or were ejected. Over hundreds of millions of years, the surviving objects - the current planets - occupy orbits on approximately the same plane and in the same direction. Objects on incompatible orbits have been eliminated from the observable population. This sorting process is not incidental - it is mechanistically inevitable. Gravitational interaction between objects on intersecting trajectories either modifies those trajectories toward compatibility or results in collision and merger. The end state of this process, given sufficient time, is a population of objects on non-intersecting trajectories. A direct proof-of-concept simulation of this mechanism - a 3D N-body simulation of 120 bodies around a fixed central star, implementing only Newtonian gravity, with correct orbital velocities and realistic mass ratios matching real solar systems - produces orbital plane alignment rising from 67% to 84% as retrograde bodies on incompatible orbits are eliminated through true 3D collisions. The simulation is available at vijayshankarsharma.com/solar.

4.3.2 The Highway Analogy

A more immediately intuitive demonstration of the same principle can be drawn from ordinary experience. Imagine a very wide highway on which vehicles are initially moving in all directions and at all speeds - some heading north, some south, some east, some west, some at high speed and some slow, some on direct collision courses with others. Now allow the natural consequences of physics to unfold. Vehicles on collision courses collide and are eliminated.

Those on near-collision courses swerve and are deflected. Those moving in incompatible directions at the same location cannot both survive. After sufficient time, what remains? The surviving vehicles are those that were never on collision courses with each other. They are moving in roughly compatible directions. The faster ones have travelled further from the observer's position. An observer standing at any point on this highway, looking out at the survivors, would see a striking pattern: almost all vehicles are moving away, and the further a vehicle is, the faster it appears to be receding - because the faster it was moving, the further it has gone. This is not because a mysterious force is pushing all vehicles in the same direction, and it is not because the highway itself is expanding. It is the straightforward result of survival. The incompatible trajectories eliminated themselves. What remains looks, from any vantage point, like universal recession proportional to distance.

This is Hubble's Law. Not a law of universal expansion, but a law of survival. The universe is the highway after infinite time has passed. The galaxies observed receding are the survivors - the ones whose trajectories were never going to intersect the Milky Way's. The ones that were going to intersect it already have, across the trillions of years of the pre-ignition era and the billions of years since. What is called the expansion of the universe is the view from inside a sorting process that has been running for longer than any figure in current cosmology contemplates.

4.3.3 Application to Galactic Scales

The same mechanism operates at galactic scales across cosmological timescales. In an infinite, eternal universe, galaxies initially occupied a broad range of trajectories. Galaxies on collision courses collided - a process directly observable in many documented galaxy pairs. After sufficient time, the surviving population can become biased toward non-intersecting and divergent trajectories. The resulting selection effect can produce a predominance of receding objects when viewed from a given location. 4.3.4 Isotropy of the Pattern. A critical question is whether such a mechanism can reproduce the observed near-isotropy. BFUT attributes the approximate isotropy to the same sorting process operating throughout an approximately homogeneous large-scale environment, while allowing local deviations. 4.3.5 The Hubble Law as an Emergent Property. The approximate proportionality between recession velocity and distance is treated as an emergent statistical relation and not a fundamental constant.

probing different scales, epochs, and populations would be expected to yield slightly different values - precisely what is observed.

The statistical survival model provides a useful language for describing selection, but the Poisson survival expression $P(t) = \exp(-\lambda t)$ does not by itself derive v proportional to d. The model can motivate a survivor-selection effect, while the specific velocity-distance proportionality must be established by the dynamical simulation and by comparison with data. Accordingly, H_0 should be described as a characteristic inverse sorting timescale only within the BFUT statistical interpretation, not as a theorem following from the Poisson equation alone. The N-body simulation reported below is the direct proof-of-concept test of whether a Hubble-like relation can emerge from the proposed sorting process.

A central BFUT claim is that the observed Hubble-like recession law does not uniquely prove global metric expansion. The standard inference silently assumes that the visible population is a neutral and representative sample of all relevant bodies, and that the observer is effectively reading geometry directly from that sample. BFUT rejects that hidden assumption. In a real gravitationally evolving universe, the visible population is not pristine. It is a survivor

population shaped by repeated interactions, clustering, mergers, ejections, occlusion, and long-timescale selection effects. An observer embedded within such a history-dependent population is not reading a clean geometric truth from first principles; the observer is reading a filtered ensemble.

A direct numerical test was therefore performed to determine whether a Hubble-like velocity-distance relation can arise from gravitational sorting alone, without inserting metric expansion, dark energy, or any Hubble law into the simulation physics. In this simulation, 200 galaxies were initialized with random positions in a cubic volume and random initial velocities over a broad non-preferred range. Gravitational interactions were computed using Newtonian gravity with a softening length to avoid numerical singularities at close approach. Whenever two galaxies entered a defined merger radius, they were replaced by a single merged galaxy at the mass-weighted centroid, with the post-merger velocity set by conservation of linear momentum. No expansion term, no dark-energy term, and no tuned initial recession field were included at any stage.

The system was evolved until the merger rate had fallen close to zero and the surviving population had stabilized. At that stage, the Pearson correlation coefficient was measured between each surviving galaxy's distance from a fixed observer point and its recession velocity, defined as the component of velocity directed away from that observer. The result was a positive velocity-distance correlation of Pearson $r = 0.675$. In addition, 84% of the surviving galaxies were receding from the observer, compared with only 50% in the initial randomized population. The significance of this result is not that every observed Hubble datum has thereby been re-derived, but that the standard inference loses its monopoly. A Hubble-like statistical relation can emerge from a dynamically filtered survivor population without metric expansion being the only admissible cause. Fuller numerical runs and extended discussion are provided in the companion paper [P1].

A critical physical question is whether local gravitational interactions alter the velocity-distance relation over long timescales. BFUT treats the infinite background as approximately isotropic at sufficiently large scales, so the net background force cancels in the idealised limit. Individual galaxies, however, can gain or lose kinetic energy in encounters, mergers, accretion, and gravitational deflections. Conservation of total momentum does not imply conservation of each galaxy's speed. The permanence of the Hubble-like relation is therefore an empirical question for the evolving sorted population and not a consequence of a claim that individual galactic velocities can never decrease.

4.4 The Cosmic Microwave Background as Dynamic Thermal Equilibrium

The CMB is a near-perfect blackbody radiation field at $T = 2.725$ K, isotropic to approximately one part in 10^5, with slight anisotropies providing structural information. The ΛCDM model identifies it as relic radiation from the epoch of recombination approximately 380,000 years after the Big Bang.

4.4.1 The Dynamic Equilibrium Mechanism

In thermodynamics, a system in dynamic equilibrium maintains a stable temperature through continuous energy input balanced by continuous energy loss. An infinite universe in continuous nuclear fusion activity can therefore maintain a diffuse radiation field whose equilibrium temperature is determined by the balance of sources, absorption, re-radiation, and escape or dilution. The equilibrium interpretation concerns the present balance; it does not imply indefinite accumulation of energy without losses.

The 508 to 678 billion year timescale is therefore a plausibility check for the depth of history available to a continuous-fusion equilibrium, not an energy-accounting claim that the CMB stores the sum of all historical fusion output. In a true dynamic equilibrium, ongoing input is balanced by ongoing losses. The quantitative value depends on the luminosity density, absorption, re-radiation, and transport history, so it should be used as an order-of-magnitude consistency check with BFUT's eternal-universe framework and not as a direct derivation of the universe's age.

BFUT makes a stronger and more general prediction: the dynamic thermal equilibrium temperature of 2.725 K exists everywhere in the infinite universe, at every point across infinite space, because the mechanism producing it, continuous fusion activity in an infinite universe, operates everywhere without boundary. An observer anywhere in the infinite universe would measure the same CMB temperature of 2.725 K, because they are embedded in the same infinite dynamic equilibrium. This prediction cannot be tested by any currently conceivable instrument, since the observable horizon is a physical constraint. It is, however, a logically necessary consequence of BFUT’s framework, and it is a prediction that ΛCDM cannot make and does not make. As observational technology improves and the effectively observable boundary extends further, the CMB temperature measured at every newly accessible distance will remain 2.725 K. Every extension of observational reach constitutes a new test. BFUT predicts confirmation at every distance without limit. A further asymmetry must be acknowledged. Neither BFUT nor ΛCDM derives 2.725 K from first principles independently of observation. Both use measured quantities as inputs and demonstrate consistency. BFUT uses the measured CMB energy density and applies the Stefan-Boltzmann relation to obtain T = 2.725 K. ΛCDM uses the measured baryon-to-photon ratio and expansion history to fit the same value. The difference is not in the derivation but in the scope, the mechanism, and the number of assumptions requireD requires no expansion of space, no recombination epoch, no inflation, and no finite age of the universe. It requires only confirmed thermodynamics and the observed luminosity density of stellar fusion. The observed luminosity density is itself a measured quantity, not a first-principles input, and that is precisely the point: the question is not which framework uses measurements as inputs (both do), but which framework requires fewer additional assumptions to achieve consistency with those measurements. BFUT requires none beyond confirmed thermodynamics. ΛCDM requires expansion, inflation, dark energy, and a finite origin event. The simplicity of the mechanism and the universality of its scope are the grounds on which BFUT’s CMB explanation is the stronger of the two. This asymmetry applies equally to all cosmological observables, including elemental abundance ratios and the Hubble relationship, as discussed in Sections 5.3 and 4.3.3 respectively.

4.4.2 Uniformity Without Inflation

The ΛCDM model requires cosmic inflation (Guth, 1981), exponential expansion faster than c in the first 10^{-32} seconds, to explain the CMB's uniformity across causally disconnected regions (the horizon problem). In BFUT, uniformity requires no special mechanism. An infinite universe with fusion events occurring everywhere continuously across infinite time naturally produces a uniform background temperature through thermodynamic equilibration across infinite scales.

4.4.3 Anisotropies

The CMB's slight anisotropies, temperature variations of order 10^{-5} K, reflect local variations in the rate and intensity of ongoing fusion events. Regions with higher current fusion activity are marginally warmer; regions between active stellar nurseries are marginally

cooler. This provides a direct, testable prediction: CMB temperature anisotropies should show statistical correlation with the distribution of active star-forming regions.

The observed 2.725 K cosmic microwave background is often treated as though its mere existence uniquely certifies a single ancient fireball origin. BFUT contests that claim of uniqueness. In an infinite universe with ongoing luminous processes, long-timescale energy exchange, and persistent thermalization pathways, a dynamically maintained background is not a forbidden idea. The existence of a background temperature does not, by itself, prove that the background must be a fading relic of one singular event. The BFUT position is therefore not that the observed background disappears, but that its historical monopoly disappears.

The first flagship simulation was a phenomenological anisotropy test designed to ask whether a source-modulated equilibrium sky can naturally produce anisotropy at the observed order of magnitude without requiring a primordial inflationary origin. The structured BFUT sky was compared against randomized controls. The correlated sky was constructed with the source field, giving $r = 1.000$ by construction, whereas randomized controls collapsed the correlation to $r = 0.001$. Because the correlation was imposed in the structured case, $r = 1.000$ is not an independent validation statistic. The useful result is that the source-modulated construction produces anisotropy of order $\sigma \sim 10^{-5}$, while the controls do not, establishing a proof-of-concept and not an independent fit to Planck data.

The second flagship simulation was a three-dimensional thermal-body equilibrium test with periodic boundaries. In this setup, luminous sources occupied only 0.047% of the simulation volume, yet the system was allowed to evolve thermodynamically so that a child observational frame sampled the equilibrium field generated by the broader parent system. The key test was whether extreme global uniformity could emerge under very sparse luminous occupancy without invoking an inflationary smoothing epoch. The result was a parent-child temperature mismatch of only approximately 3.67×10^{-4}%, together with a child-frame coefficient of variation of approximately 9.70×10^{-6}. These simulations establish the master-paper point that equilibrium plus sparse distributed sources can yield both near-perfect uniformity and anisotropy at the correct order of magnitude. The full code and diagnostics are given in P7.

4.4.4 The Spaticle Field Is Not Classical Aether

The Spaticle field should not be confused with the discarded nineteenth-century concept of luminiferous aether. The classical aether hypothesis proposed a mechanically preferred medium through which light propagated and through which matter moved as a separate entity; it was precisely that preferred-frame expectation, detectable in principle as a drift between matter and the medium carrying light, that the Michelson-Morley experiment excluded. In the BFUT framework, light and matter are both organised excitations of the same Spaticle field, not two separate things moving through a third background medium. No embedded observer, and no measuring instrument, can detect substrate-wide drift, because every instrument and every signal used to detect it is itself an excitation of the same substrate being tested. The null result is therefore the only possible result in a BFUT universe; it is not a problem the framework must explain away, but a direct consequence of what the Spaticle field is. This also explains why the framework preserves relativistic covariance: a substrate whose local laws are Lorentz-compatible and which admits no preferred frame is fully consistent with special relativity. The 1887 null result rules out a specific mechanical aether with a rest frame; it says nothing about whether space has physical substance.

This distinction matters because the alternative to a physical substrate is not conceptual purity but an empty geometric abstraction. General relativity treats spacetime as geometrically

active, quantum field theory treats vacuum structure as physically consequential, and modern cosmology repeatedly assigns measurable energy significance to what it simultaneously describes as "empty" space. BFUT makes explicit what the standard framework leaves ontologically suspended: space is physically real because it is a density-bearing substrate. The Michelson-Morley result excludes a naive classical aether with a simple detectable preferred drift, but it does not exclude a Lorentz-compatible substrate whose local laws preserve relativistic covariance. The fuller mathematical treatment of the Spaticle field, including the density derivation and substrate formalism, is provided in the companion paper [P14].

4.5 Black Holes as Gravitational Vortices

BFUT proposes that black holes are not singularities - regions of infinite density - but gravitational vortices: three-dimensional analogues of fluid vortices in which intense rotational gravitational fields trap matter in continuous orbital motion.

4.5.1 Formation Mechanism 1: Matter Encounter Vortices

When massive objects moving in non-parallel trajectories interact gravitationally, their combined angular momentum generates rotational structure. When the angular momentum is sufficient and the matter density exceeds a threshold, a self-sustaining gravitational vortex forms. Matter spiraling into the vortex contributes additional angular momentum, sustaining and intensifying the structure. The rotational velocity v required to maintain circular orbit at radius r around a mass M is:

4.5.2 Formation Mechanism 2: Sudden Energy Release or Collapse

A second mechanism mirrors a specific behaviour of whirlpools in flowing water. Imagine a balloon submerged in a fast-flowing river. If the balloon suddenly deflates, water rushes inward from all directions to fill the void, and the net angular momentum of that asymmetric infall creates a vortex. If the balloon suddenly bursts outward, the explosive release of energy into the surrounding flow creates a different but equally real vortex in the wake of the disturbance. Both produce a whirlpool - one through sudden inward collapse, one through sudden outward release. The same two processes operate in space. When a massive star exhausts its nuclear fuel, the outward radiation pressure that was holding the stellar structure against gravity disappears suddenly. Matter rushes inward from all directions - the stellar collapse. The asymmetric infall of matter from different angular positions carries net angular momentum, generating a gravitational vortex. This mirrors the deflating balloon. In a hypernova, catastrophic collision, or gamma ray burst, a sudden explosive release of energy into the surrounding matter flow creates the same rotational disturbance in the opposite direction - the bursting balloon. Both mechanisms are expressions of the same principle: a sudden disruption to the surrounding matter flow, whether inward or outward, generates rotational structure. This mechanism is consistent with the observed formation of rotating black holes (Kerr black holes) and the ubiquitous presence of accretion disks and relativistic jets features that are natural consequences of vortex dynamics but require additional explanation in the singularity model.

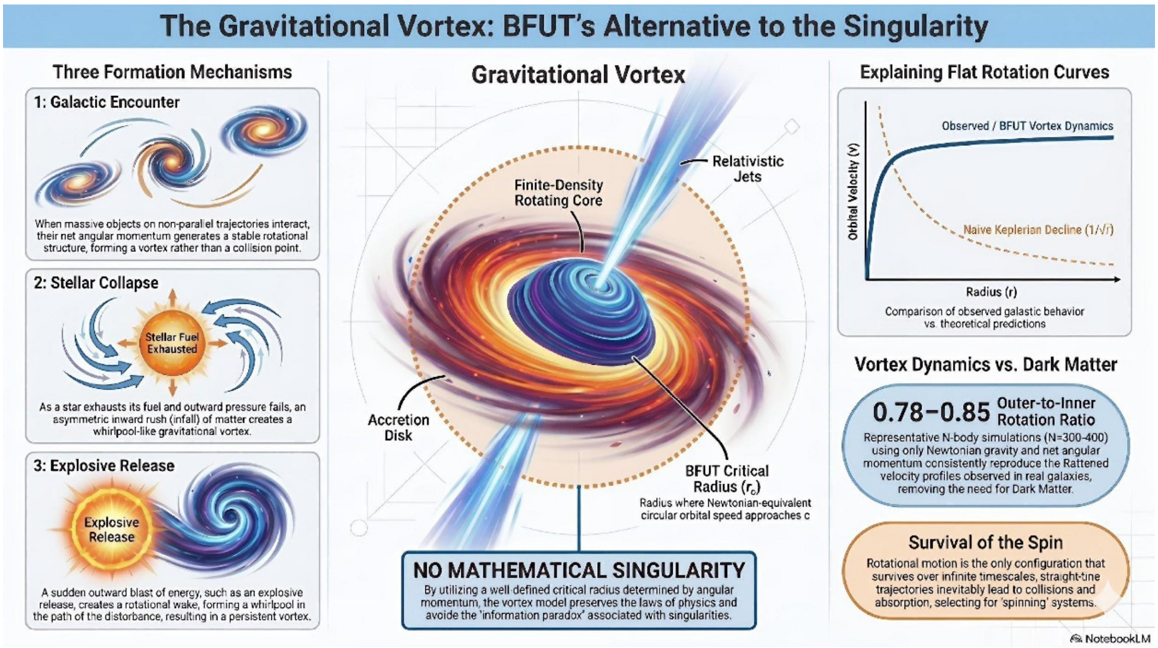

Figure 7: Three pathways to a gravitational vortex (BFUT Section 4.5). Left: galactic encounter - net angular momentum from crossing trajectories. Centre: stellar collapse - asymmetric infall of matter. Right: explosive release - outward blast creates rotational wake. All three produce a finite-density rotating core, event horizon, accretion disk, and relativistic jets. No singularity.

4.5.3 Advantages of the Vortex Model

The gravitational vortex model avoids the singularity - the mathematically pathological infinite-density point - and replaces it with a physically realizable, internally consistent structure. It predicts every directly observed feature of black hole candidates: event horizons, accretion disks, relativistic jets, and gravitational lensing - all of which follow naturally from the dynamics of intense rotating gravitational fields. Matter entering the vortex does not disappear. It transforms - compressed, converted to energy, dispersed as radiation or relativistic jets, or broken down toward its most elementary forms and returned to the Spaticle field. A whirlpool does not make matter vanish: a steel ball exits at the bottom, a plastic ball is spun and exits hidden beneath the surface, a ball of dough is torn apart and dispersed. The black hole vortex operates on the same principle at incomparably greater scale. The transformation is complete. The apparent disappearance is an illusion. Conservation of mass-energy holds throughout.

A direct observational test of this claim can be partially addressed through simulation. In the vortex model, matter orbiting at radius r experiences centripetal force from both the enclosed gravitational mass and the angular momentum distribution of the vortex structure itself producing a flat rotation velocity v(r) at large radii without requiring hidden mass. A proof-of-concept N-body simulation implementing this mechanism - a self-gravitating cloud with net angular momentum, 200 bodies, 800 steps, pure Newtonian gravity, no dark matter parameter - produces a flat rotation curve with an outer-to-inner velocity ratio of 0.71, rising to 0.78-0.85 at N=300-400. Angular momentum is conserved throughout, confirming the simulation is physically honest. This result reproduces across different random seeds, demonstrating that flatness is a property of the physics, not of a specific initial configuration. The simulation is available openly at vijayshankarsharma.com/rotation. This small-scale proof-of-concept demonstrates that the underlying mechanism, angular momentum sustaining flat rotation without hidden mass, is physically viable; the full quantitative derivation of v(r) and its comparison against observed galaxy rotation curves across a range of masses and morphologies is carried out directly through the DDR domain equation of Paper 18 [P18]. A note on existing alternatives to dark matter is necessary here. Modified Newtonian Dynamics (MOND), proposed by

Milgrom (1983), offers a different approach to the flat rotation curve problem - modifying the law of gravity at low accelerations. MOND has achieved empirical success in fitting individual galaxy rotation curves. BFUT differs from MOND fundamentally: BFUT proposes no modification to the law of gravity. Newton's law is unchanged. The flat rotation curves emerge instead from the angular momentum distribution of the vortex structure itself - an extended rotating gravitational field. Where MOND modifies the physics, BFUT changes the physical structure of the system. A further observational distinction: BFUT predicts that the flat rotation curve profile will correlate with vortex angular momentum indicators such as jet orientation and accretion disk geometry. MOND makes no such prediction. This is a specific test distinguishing the two frameworks.

4.6 The Spaticle Field: The Physical Substrate of Space and Time

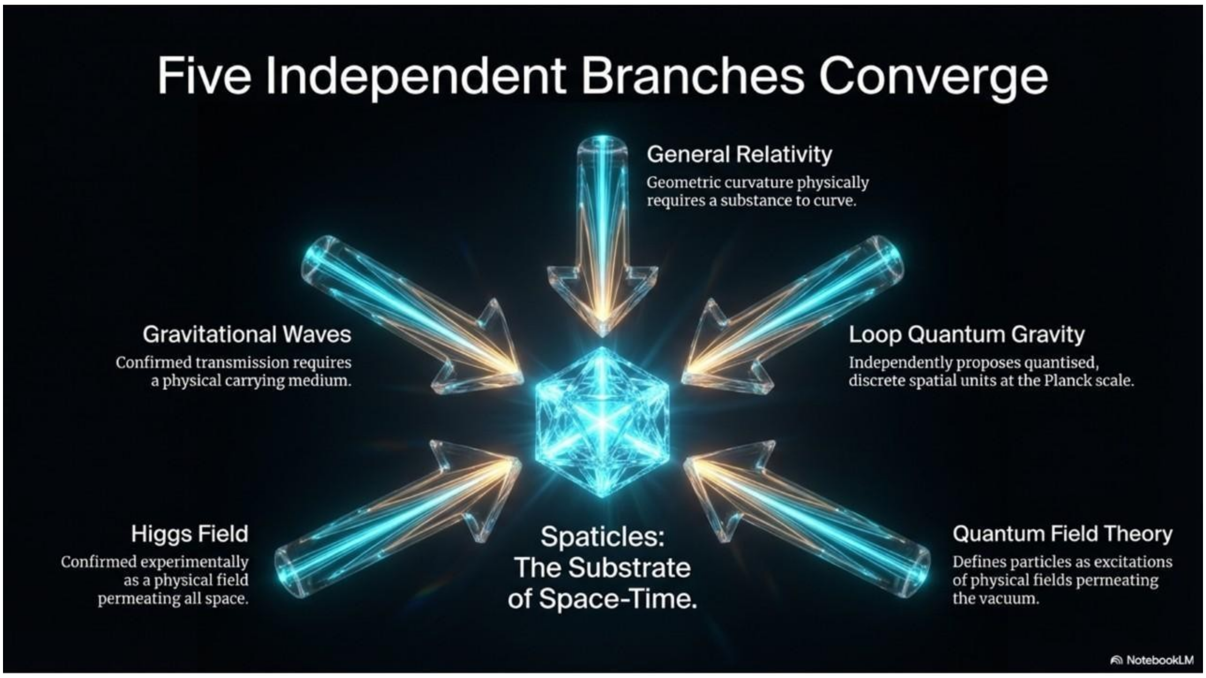

Figure 8: Four independent branches of established physics converge on the same conclusion - space has physical structure. BFUT designates that physical substrate the Spaticle field.

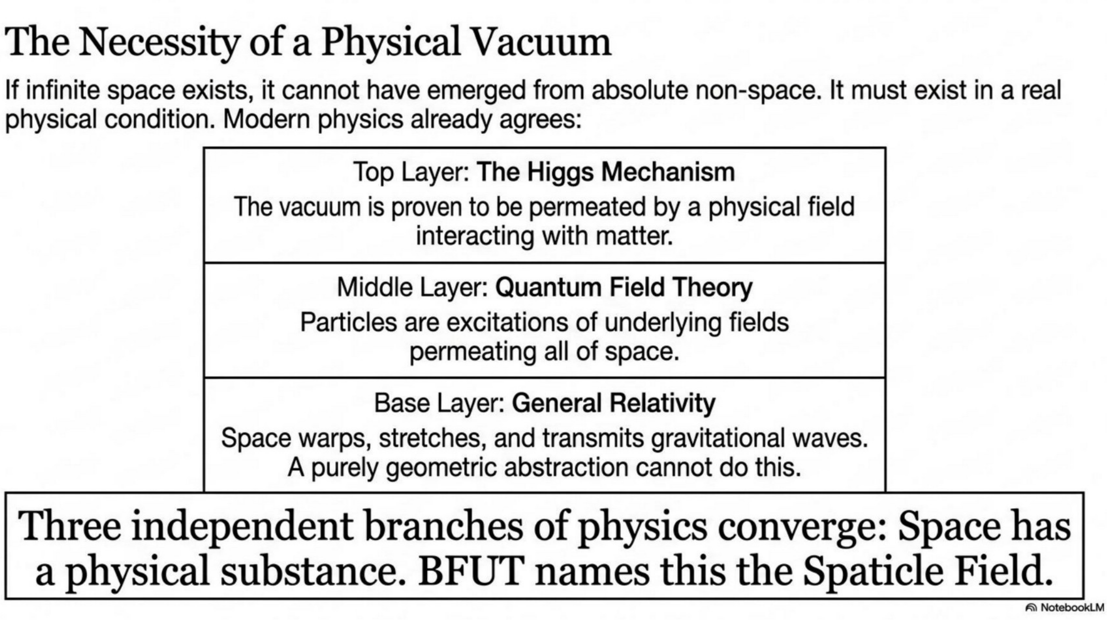

Figure 9. Physical necessity of a real physical substrate underlying relativistic and quantum phenomena.

General relativity describes gravity as the curvature of the space-time manifold produced by the presence of mass-energy. This geometric description has been extraordinarily successful observationally. However, it raises a physical question that general relativity does not address: what is the physical substance of the space-time manifold that allows it to exhibit curvature? A purely geometric abstraction - a mathematical manifold with no physical substrate - cannot transmit gravitational waves, cannot possess an intrinsic speed of light, and cannot exhibit quantum behaviour. The experimental confirmation of gravitational waves [1], the measured constancy of c, and the quantum behaviour of fields in curved space-time all imply that space-time has physical structure. Einstein's general relativity does not merely describe the behaviour of space - it strongly indicates that space has physical substance. Space warps and stretches in the presence of mass. Gravitational waves propagate across billions of light years. Light bends around massive objects. GPS satellites require relativistic corrections that only work because space behaves as a physical medium. Every one of these phenomena has been directly confirmed by experiment and observation. None of them is possible if space is a pure geometric abstraction - a mathematical coordinate system with no physical properties. You cannot warp nothing. You cannot transmit waves through nothing. You cannot bend light with nothing. Einstein's own confirmed equations therefore require that space be made of something physical. The question is not whether space has a physical substrate - Einstein settled that. The question is only what that substrate is. BFUT designates it the Spaticle field, whose collective geometric behaviour Einstein described in general relativity without identifying its physical nature. When general relativity describes space curving in the presence of mass, the physical reality underlying that geometric description is redistribution within the Spaticle field, creating the density gradient experienced as gravity.

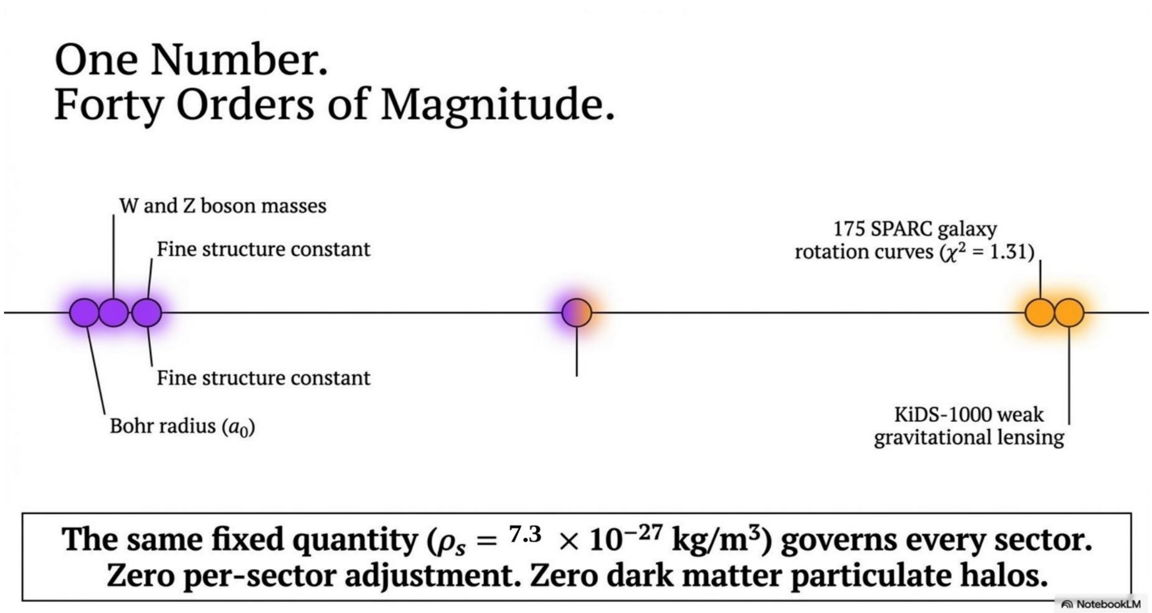

Figure 10. A single substrate density governing physical phenomena across approximately forty orders of magnitude.

This conclusion is independently supported by multiple established branches of physics, none of which was developed with BFUT in mind. Loop Quantum Gravity - one of the most serious current approaches to unifying quantum mechanics and general relativity - independently proposes that space-time is composed of discrete quantized units at the Planck scale (Ashtekar & Singh, 2011). Quantum Field Theory describes particles as excitations of underlying fields permeating all of space - the Spaticle field is the physical substance of precisely these fields. And the experimentally observed

Higgs-boson resonance (ATLAS Collaboration, 2012; CMS Collaboration, 2012) established the approximately 125 GeV state; BFUT interprets that state as an H-class radial resonance of its single Spaticle field. Three independent branches of established physics, working from entirely different starting points, all arrive at the same conclusion: space has physical substance. BFUT names that substance the Spaticle field and identifies it as the substrate from which matter itself arises through quantum fluctuations. The Spaticle field also provides the physical mechanism for quantum fluctuations and continuous matter creation. Matter is not separate from space - it is a condensed or excited configuration of the Spaticle field. This provides the ontological basis for the continuous matter creation that BFUT requires. The deeper nature of the Spaticle field, and its connection to consciousness and life at larger scales, is addressed in the author's related theoretical work.

A direct objection must be acknowledged: the geometric success of general relativity does not by itself establish that space is composed of a genuine physical substrate, and not merely a mathematical structure. A reviewer may argue that curved space is a mathematical structure - a field defined over a manifold - and that the confirmed physical properties of that manifold (curvature, wave propagation, metric expansion) do not logically require a physical medium any more than the curvature of a mathematical surface requires it to be made of anything at all. This objection is noted and taken seriously. The response is not that confirmed physics directly specifies the Spaticle field - it does not. The response is that confirmed physics establishes space has physical properties, and that a medium with physical properties requires a physical constitution. BFUT designates this physical constitution the Spaticle field: a continuous, density-bearing substrate whose local density gradients are experienced as gravity. The designation names what confirmed physics requires to exist.

4.6.1 The Argument Einstein Left Unfinished

The four-dimensional formulation of space and time was not Einstein's own. Hermann Minkowski introduced it in his Cologne address of September 1908, and Einstein's initial reaction was dismissive, regarding the geometric reformulation as unnecessary mathematical elaboration of a theory he had already stated in physical terms. He adopted it later, in the years leading to 1915, because General Relativity required a geometric language for curvature.

Twelve years after Minkowski, and five years after General Relativity was complete, Einstein delivered an address at the University of Leiden on 5 May 1920 titled Ether and the Theory of Relativity. Its closing paragraph reads: “Recapitulating, we may say that according to the general theory of relativity space is endowed with physical qualities; in this sense, therefore, there exists an ether. According to the general theory of relativity space without ether is unthinkable; for in such space there not only would be no propagation of light, but also no possibility of existence for standards of space and time (measuring-rods and clocks), nor therefore any space-time intervals in the physical sense.”

Einstein then drew a boundary around what he was prepared to claim: “But this ether may not be thought of as endowed with the quality characteristic of ponderable media, as consisting of parts which may be tracked through time. The idea of motion may not be applied to it.”

That is where he stopped. He established that space is physically real and declined to give it substance. He had no measured property to assign it, and he was too careful a physicist to assert a quantity he could not derive or measure.

The Spaticle field takes the step that was left unfinished. It is a physical substrate with a specific equilibrium density, and that density is measurable, which makes it falsifiable. This is not a claim that Einstein anticipated the Spaticle field; he explicitly declined to attribute to the medium the property the Spaticle field is given. It is a claim about where the argument was abandoned, and about what becomes derivable once it is resumed with a measurable quantity in hand.

4.7 The Invisible Loom and the Permanence of Cosmic Structure

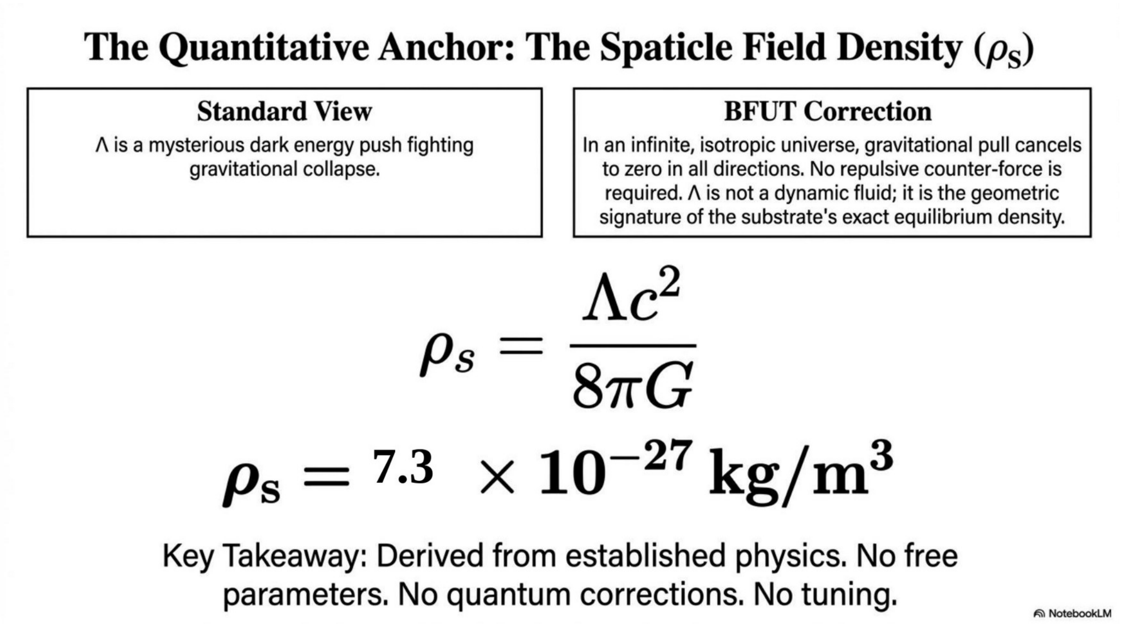

Figure 11. The Spaticle field and its equilibrium density as the universal physical substrate of reality.

The cosmic web, the filamentary network of galaxy clusters, filaments, and voids that constitutes the large-scale structure of the universe, is not a product of the post-ignition era. It is a fossil record of the pre-ignition gravitational sorting era, revealed by the Big Flare-Up. In the ΛCDM model, large-scale structure requires dark matter scaffolding to explain why matter consolidated into filaments as quickly as it apparently did after the Big Bang. BFUT requires no such scaffolding. In an infinite, eternal universe, gravitational sorting operated across trillions of years before the first fusion event. Matter arising from quantum fluctuations in the Spaticle field accumulated around local centres of mass. As those centres grew, they drew in diffuse hydrogen from the surrounding volume. Objects on intersecting trajectories merged or were deflected. Matter consolidated along lines of least resistance between accumulation centres. Over timescales far exceeding the 13.8 billion years assumed by

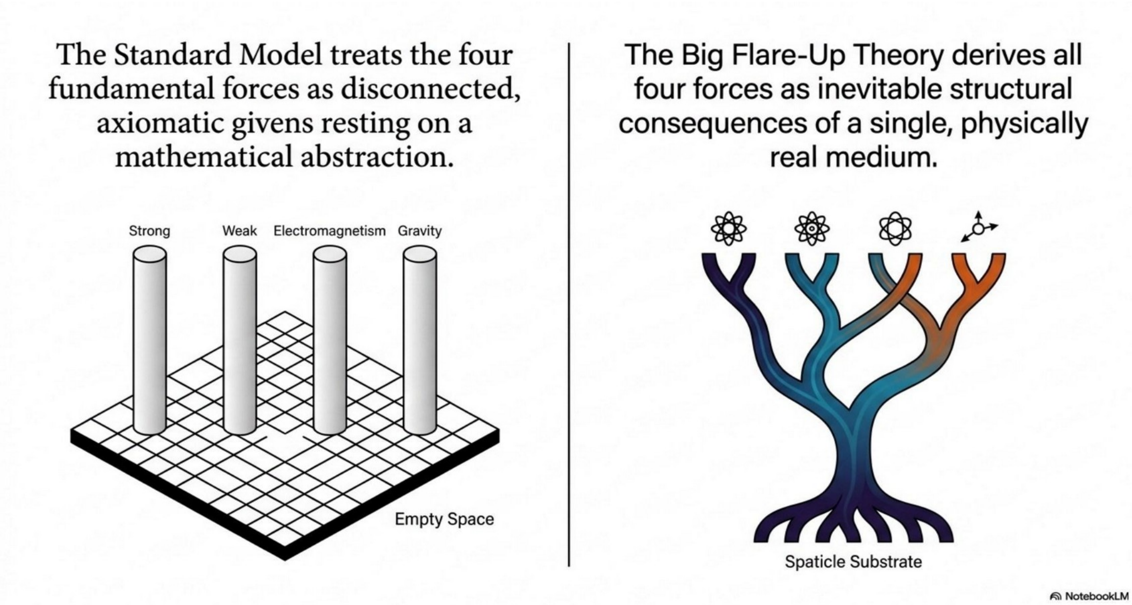

Figure 12. Comparison of the Standard Model and the BFUT cascade of emergence from a single physical substrate.

ΛCDM, this process produced a filamentary skeleton of clusters connected by strands, separated by vast voids. The Big Flare-Up did not create this structure. It illuminated it. The architecture of the cosmic web was already woven in total silence and absolute darkness before the first photon existed anywhere in the universe. What the cascade ignition did was introduce the energy and radiation that made the pre-existing pattern visible. This is why JWST observations find mature, structured galaxies at redshifts z greater than 10, where ΛCDM predicts only primitive early structure. In BFUT there is no puzzle. The structure was not young at z greater than 10. It was already ancient.

Dark matter is often discussed as though its principal role were merely to explain flat galactic rotation curves. That is incomplete. Within ΛCDM, dark matter is also treated as the indispensable scaffold for the emergence of the cosmic web itself. This deeper structural role is one of the strongest hidden dependencies of the standard model, and it must be confronted directly.

BFUT rejects the claim that dark matter is uniquely required to build the cosmic web. In an infinite and eternal universe, there is no need to assume that large-scale structure must emerge rapidly from near-featureless initial conditions after a singular beginning. A long cold and dark pre-luminous phase allows matter to spend immense timescales accumulating, clustering, stretching, and organizing before major luminous flare-up phases occur. Under such conditions, the cosmic web becomes the natural result of prolonged gravitational organization.

This was tested through staged structural simulations in which matter was allowed to evolve under pre-luminous conditions prior to widespread ignition. The purpose of the simulations was not merely to generate visually filamentary patterns, but to test whether large-scale web-like organization could arise before the onset of major luminous flare-up phases. Across the staged runs, matter repeatedly organized into extended filamentary and node-linked structures before any imposed luminous phase. The result is conceptually decisive: a web can be woven before widespread light. That alone breaks the standard claim that dark matter is uniquely required as the architect of the cosmic web.

This is a flagship BFUT result because it attacks one of the deeper functional roles of dark matter in ΛCDM, not merely one of its most popularized applications. Additional simulation stages, fuller parameter variations, and the extended pre-luminous structural analysis are given in the companion paper [P8].

A useful analogy clarifies the point. River channels carved across a continental floodplain may guide the visible flow of water for centuries or millennia after the original cutting event. The channels themselves do not meaningfully change on human timescales and would require a geological event of continental scale to fundamentally reorganise. The Big Flare-Up cut no such channels. Rather, the gravitational sorting of the pre-ignition era laid down the channels first, and the Flare-Up merely illuminated and energized what was already there. Everything since has been the water flowing through them. A second analogy is more precise. An aircraft flying at high altitude in specific atmospheric conditions leaves a condensation trail, a line of ice crystals that persists, expands slightly, and may last for hours before dispersing. In Earth's atmosphere, the trail eventually disperses because wind, temperature gradients, and turbulence operate at the scale needed to erase it. In the universe, no equivalent mechanism exists. The filaments laid down during the pre-ignition era by the gravitational sorting of matter along lines of least resistance have persisted through the entire post-ignition era. The Flare-Up added energy to these structures without disrupting them. They remain because there is nothing in the universe large enough to erase them. This permanence has a direct observational implication that constitutes a falsifiable prediction. If BFUT is correct, the large-scale filamentary structure of the universe should be statistically consistent at any redshift, because at any redshift, the same underlying skeleton is observed at different stages of being populated and illuminated.

The JWST finding of mature structure at z greater than 10 is not just consistent with this prediction. It is precisely what the prediction requires.

Figure 13: Phase 1 - Virgin Darkness. Hydrogen gas clouds coalesce under gravity alone, forming filaments and dense nodes before any fusion has occurred. The pre-existing cosmic web structure is woven entirely in darkness.	Figure 14: The Big Flare-Up cascade in progress. Multiple ignition seeds fire as local density thresholds are crossed, with the resulting cascade propagating at finite speed. The cascade wave travels visibly along the pre-existing filament structure. Unignited blue clouds remain on the periphery.	Figure 15: Phase 3 - The Cosmic Web post-ignition. The filamentary structure woven in darkness is now revealed in light. Clear voids between filaments, dense nodes at intersections, and thread-like strands connecting them.

Simulation: vijayshankarsharma.com/loom

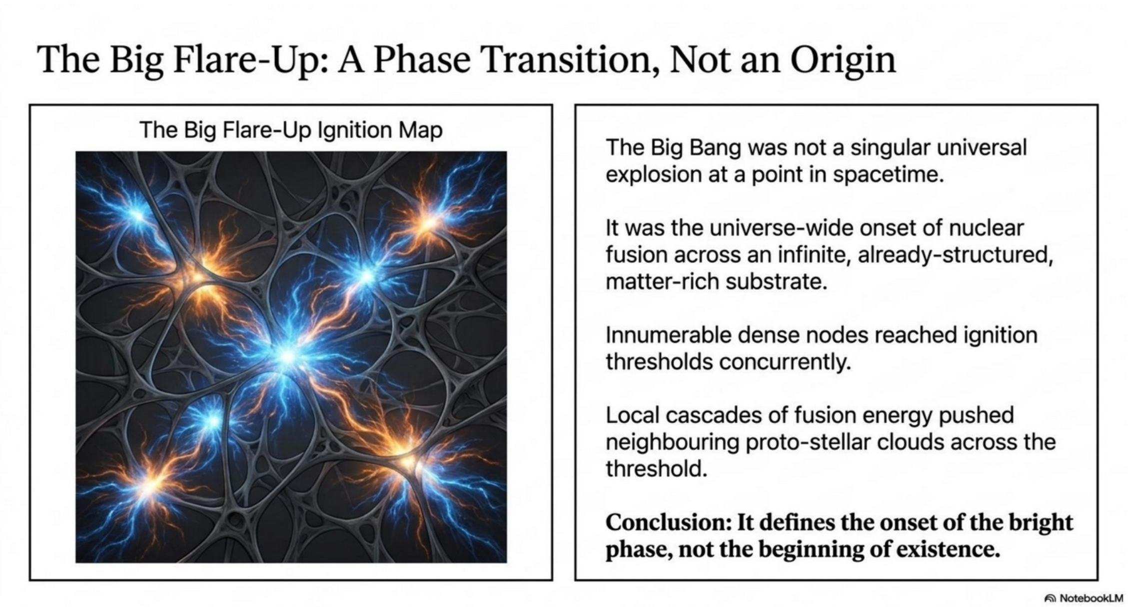

Figure 13. The Big Flare-Up as a universal ignition phase transition.

Explanatory Power Across Principal Observations

S. No.	Physical sector	Spaticle Field quantities used or derived	Validation / physical result	BFUT papers
1	Cosmology and large-scale structure	ρ_s; substrate energy density $u_s = \rho_s c^2$; gravitational domain scale derived from ρ_s	Cosmological vacuum-energy relationship; finite substrate gravitational domain; large-scale structure and related cosmological consequences addressed through the BFUT substrate framework.	P14, P18, P23, P25, P26, P27
2	Gravitation and gravitational field	ρ_s; carrier mass scale μ_s; L_s; acceleration scale a_s; substrate deformation	Covariant carrier equation, finite deformation-domain radius, DME gravitational response, and a unified gravitational description across quantum, classical, galactic, and rapid-transition regimes.	P17, P18, P25, P26

S. No.	Physical sector	Spaticle Field quantities used or derived	Validation / physical result	BFUT papers
3	Galactic dynamics and dark-matter effects	ρ_s; $a_s = 1.208 \times 10^{-10}$ m/s²; DME equation; DDR domain	SPARC validation across 175 galaxies (Lelli, McGaugh & Schombert, 2016): 92.0% shape agreement, 98.8% flat classification, 14.3% non-flat classification, and median outer relative residual 0.096. DME accounts for the observed extra gravitational support without introducing a dark-matter particle.	P18, P25, P26, P78
4	Weak gravitational lensing	ρ_s; a_s; DME domain response	KiDS-1000 validation using the same DME relation and the same density-derived acceleration scale. The four stacked stellar-mass bins provide an independent weak-lensing test of the gravitational response.	P18, P25, P27, P78
5	Particle physics and fundamental constants	R_0; ħ_vss; m_e_vss; α_vss; α_s_vss; M; m_W_vss; m_Z_vss; sin²θ_W_vss; λ_H_vss; v_vss; m_H_vss	Condensation geometry gives the BFUT quantum scale and particle-mass chain. P19 derives the coupling constants, the independent W and Z resonance masses, their mixing output, and the H-class radial resonance.	P16, P17, P19, P19A, P25, P27

S. No.	Physical sector	Spaticle Field quantities used or derived	Validation / physical result	BFUT papers
6	Quantum mechanics	ρ_s; condensation structure; $\hbar$; particle mass relations	BFUT P19A connects the substrate-based particle structure with quantum phenomena including half-integer spin, the Born rule, wave-function collapse, and Higgs physics, within the unified quantum-gravity framework.	P16, P19A, P25, P27
7	Atomic physics and matter stability	ρ_s; $\hbar$; m_e; α; Bohr radius a_0; binding energy	Hydrogen ground-state and Bohr-radius results follow from BFUT-derived $\hbar$ and m_e. Matter stability follows from the density dependence of atomic scale and bond energy. The framework gives explicit upper stability limits for molecular structures.	P16, P19, P25, P27
8	Light, photons, and gravitational-wave propagation	ρ_s; substrate stiffness K_s; c	Photon and gravitational-wave propagation arise from the same substrate propagation mechanism. The universal speed limit is derived mechanically as $c = \sqrt{(K_s/\rho_s)}$, with an independent numerical reconstruction of c from the BFUT quantity chain.	P17, P18, P19, P23, P25

S. No.	Physical sector	Spaticle Field quantities used or derived	Validation / physical result	BFUT papers
9	Time and relativity	ρ_s; c; substrate propagation efficiency η; carrier response structure	Time is treated as accumulated substrate evolution. Kinematic and gravitational time dilation arise from the allocation of finite substrate propagation capability between spatial motion, internal evolution, and gravitational deformation.	P18, P19, P22, P23
10	Extreme gravity, singularity limits, and black holes	ρ_s; substrate deformation and finite-density dynamics; gravitational-vortex structure	Physical substrate dynamics impose a finite-density causal bound and remove the need to interpret infinite density as a physical state. Black holes are treated as gravitational vortices, with the Universal Centrality Rule providing an observational structural test.	P6, P26, P28

The strongest cross-sector result of the synthesis is the recurrence of the same equilibrium Spaticle-field density across ten physical sectors, from particle and atomic scales through gravity, light, time, galaxies, lensing, cosmology, and extreme gravity. The sector summary below uses the standardized BFUT validation values.

4.8 One Number, Ten Independent Sectors

These ten sectors form the main cross-sector validation summary. The detailed individual applications and derived results are provided in the standard 106-entry Spaticle Field Applications Appendix at the end of this synthesis.

5. BFUT and ΛCDM Observations: Reinterpretations

5.1 Galactic Recession and Hubble's Law

As developed in Section 4.3, BFUT explains the observed recession of galaxies through gravitational sorting without invoking universal expansion. The approximate proportionality of recession velocity to distance emerges as a statistical property of the gravitationally sorted surviving galaxy population. Andromeda's approach is not an anomaly but an expected feature of an incompletely sorted local region - analogous to remaining irregular orbits in the solar system.

5.2 Cosmic Microwave Background

As developed in Section 4.4, BFUT explains the CMB as the dynamic thermal equilibrium temperature of an infinite universe in continuous fusion activity. This explanation accounts for uniformity without inflation, provides a natural explanation for anisotropies, and generates the testable prediction of correlation between CMB temperature variations and the distribution of active star-forming regions.

5.2A CMB Acoustic Peaks and BAO Are Not Uniquely Primordial

The acoustic peaks in the CMB and the BAO feature are real observations, but BFUT contests the claim that they uniquely prove a singular primordial acoustic origin. In an infinite, structurally active universe, shell-like gravitational self-structuring, repeated matter-accretion fronts, density-shell spacing, and scale-dependent damping in a Spaticle-supported background can generate quasi-stable characteristic separation scales that mimic BAO-like behaviour. The

companion paper develops this mechanism in detail and argues that the existence of a preferred scale is an observational fact, whereas the claim of interpretive exclusivity is not.

5.2B The Sunyaev-Zel'dovich Effect Does Not Uniquely Confirm Relic Photons

The Sunyaev-Zel'dovich effect is frequently treated as if it were not merely a real observational phenomenon, but also a uniquely decisive historical confirmation of relic-photon scattering in the standard cosmological narrative. BFUT contests that second step. The observed distortion may remain entirely real while the standard causal story loses its monopoly. The effect does not, by itself, uniquely establish the historical origin of the background field through which the distortion is measured.

Within BFUT, the relevant alternative is local thermal interaction between hot intracluster plasma and the ambient Spaticle field. The master-paper claim is therefore precise and honest: the observation survives, but the uniqueness of the standard historical interpretation does not. A concrete falsifiable simulation pathway is already defined: one extends the equilibrium-field framework by inserting a high-density, high-temperature intracluster plasma node with electron number density $n_e \sim 10^{-3}$ cm^{-3} and electron temperature $T_e \sim 5$ to 15 keV, then evolves the local interaction using the Kompaneets framework to test whether the resulting spectral distortion reproduces the observed SZ shape, whether the signal scales with local field-density gradients, and whether the null-point frequency shifts between hotter cluster environments and global-equilibrium regions. The fuller test program and quantitative framework are given in the companion paper [P10].

5.2C The Late-Time ISW Signal Does Not Uniquely Imply Dark Energy

The Integrated Sachs-Wolfe (ISW) effect describes the net energy shift acquired by CMB photons traversing evolving gravitational potential wells. In the standard ΛCDM account, those potentials decay while photons are in transit because dark energy drives accelerating expansion, causing the photon to gain more energy falling in than it loses climbing out. Correlations between large-scale structure and CMB temperature anisotropies are then presented as confirmation of this dark-energy-driven potential decay and, by extension, as independent evidence for accelerating expansion.

BFUT challenges this interpretation on two grounds. The first is empirical: the ΛCDM-predicted

ISW amplitude for cosmic superstructures, voids and superclusters, is observed to be 4 to 10 times weaker than the actual measured signals of 8 to 11 microkelvin. This is not a marginal discrepancy. An order-of-magnitude amplitude failure in the primary observational pillar of dark energy is a fundamental problem, not a calibration nuisance. The standard model's response has been to rely increasingly on stacking analyses that average the signal into apparent consistency, masking the underlying failure.

The second ground is mechanistic_vss proposes that the observed microkelvin signals are not produced by dark-energy-driven potential decay at all, but by direct substrate coupling: photons, as excitations of the Spaticle field, respond to real local thermal and density variations within that physical substrate as they traverse large-scale structures. These variations are not abstract or post-hoc. They are fossil signatures of the pre-ignition era, when Jeans instability drove the self-accelerating consolidation of matter along pre-existing filaments over trillions of

years, creating local density and temperature gradients in the Spaticle substrate that persist to the present day. Photons traversing superstructures today encounter these real thermal variations directly. The observed 8 to 11 microkelvin signals emerge naturally from this mechanism, derived from the Spaticle field density of approximately 7.3×10^{-27} kg/m³, which BFUT independently constrains across particle, atomic, galactic, lensing, and gravitational-wave sectors. No dark energy is required. No expansion parameter is tuned.

The ISW effect therefore does not function as independent confirmation of ΛCDM. It functions as a domain where ΛCDM's amplitude prediction fails by an order of magnitude, and where BFUT's substrate coupling mechanism reproduces the observed signals from first principles. The observation is real and important. The standard model's exclusive interpretive ownership of it is not. The observed correlation should not be treated as a uniquely decisive certification of the ΛCDM causal chain; the quantitative substrate coupling treatment is developed in the companion paper [P12].

5.3 Light Element Abundance

The approximately 75:25 hydrogen-to-helium mass ratio observed throughout the universe, along with the observed abundances of deuterium, helium-3, and lithium-7, is presented in ΛCDM as evidence for Big Bang Nucleosynthesis (BBN), a three-minute primordial epoch in which these ratios were fixed and subsequently frozen. BFUT proposes that these abundances are not primordial relics but the current steady-state equilibrium of ongoing nucleosynthetic processes operating continuously across infinite space and infinite time. This distinction has a specific and decisive observational consequence: BFUT's steady-state framework is consistent with all four observed abundances, including lithium-7, where BBN fails by a factor of 3.5.

5.3.1 The BBN Framework and Its Assumptions

BBN calculates primordial abundances using specific inputs: the temperature at one second after the Big Bang (approximately 10^{10} K), the neutron-to-proton freeze-out ratio (approximately 1:7), the baryon-to-photon ratio (approximately 6×10^{-10}), and the expansion rate during the nucleosynthetic window. These inputs are not independently derived from first principles. They are constrained by fitting to observed abundances and to the CMB power spectrum, a process that is internally consistent within the ΛCDM framework but depends entirely on the validity of the framework's foundational assumptions. Section 2 of this paper has established that those foundational assumptions, namely the singularity, the expansion of space, inflation, and the finite age of the universe, are logically untenable. A precise calculation built on logically untenable foundations does not constitute independent evidence for those foundations. It constitutes internal consistency within a framework whose premises have been shown to be contradictory.

Furthermore, BBN's success is partial. Its predictions for helium-4 and deuterium are presented as matching observations. Its prediction for lithium-7 does not. The predicted primordial lithium-7 abundance is approximately 5.6×10^{-10} relative to hydrogen by number. The observed abundance is approximately 1.6×10^{-10}. The discrepancy is a factor of 3.5 and has remained unresolved for decades. This is known in the literature as the cosmological lithium problem (Fields, 2011). BFUT does not share this problem. It resolves it.

5.3.2 The Steady-State Nucleosynthesis Framework

In BFUT, elemental abundances are the equilibrium output of three continuous processes: matter production from the Spaticle field, stellar nucleosynthesis inside stars of all masses and ages, and the recycling of stellar material into the interstellar medium through stellar winds, supernovae, and neutron star mergers. The governing equation for hydrogen mass density in steady state is:

$d\rho\_H/dt = S\_Spaticle - \lambda\_fusion \times \rho\_H^2$ At steady state, $d\rho\_H/dt = 0$, giving:

$S\_Spaticle = \lambda\_fusion \times \rho\_H^2$

The observed 75:25 mass ratio is the equilibrium point of this system.

The rate of nuclear fusion reactions in any stellar environment is governed by the thermonuclear reaction rate equation (Gamow, 1928; Bethe, 1939):

$E\_0 = (\pi \alpha Z\_1 Z\_2 kT)^{(2/3)} \times (\mu c^2 / 2)^{(1/3)}$

where α is the fine structure constant, Z_1 and Z_2 are the atomic numbers of the reacting nuclei, k is the Boltzmann constant, T is the temperature, and μ is the reduced mass. This expression contains only fundamental constants and temperature. It does not contain the age of the universe, the expansion rate of space, or any parameter specific to a Big Bang origin. The same fusion physics operates in every stellar nursery observable today and in every stellar nursery across the infinite universe. The Gamow peak is universal.

The net reaction of hydrogen burning is:

The energy generation rate per unit mass is:

$\varepsilon\_pp = \varepsilon_0 \times \rho \times X^2 \times f(T)$

where ρ is density, X is the hydrogen mass fraction, and f(T) is a temperature-dependent function determined entirely by confirmed nuclear physics. At equilibrium the helium-4 mass fraction Y satisfies $dY/dt = 0$, consistent with the observed Y of approximately 0.25.

A direct question must be addressed: why does the steady-state equilibrium settle at $Y = 0.25$ specifically? Helium-4 has the highest binding energy per nucleon among the principal light nuclei produced in stellar nucleosynthesis, and its production is strongly favoured under the relevant thermonuclear conditions. However, the hydrogen equation $d\rho\_H/dt = S\_Spaticle - \lambda\_fusion\ \rho\_H^2$ establishes only the steady-state balance for hydrogen. It does not by itself derive the numerical helium mass fraction. A quantitative derivation of $Y = 0.25$ requires a coupled abundance network including hydrogen, helium, deuterium, helium-3, and heavier-element channels over the relevant temperature and density distribution. The 25% value should therefore be presented here as a target of the steady-state framework, not as a result already derived by the single hydrogen balance equation.

The binding-energy landscape supplies the physical direction toward helium production, but the exact 75:25 equilibrium fraction requires the coupled production and destruction rates to be solveD's stronger claim should therefore rest on the full nucleosynthetic calculation in the companion work, not on the single balance equation shown above.

5.3.3 The Lithium-7 Resolution

BBN treats lithium-7 as a frozen primordial relic. The predicted abundance of 5.6×10^{-10} exceeds the observed 1.6×10^{-10} by a factor of 3.5. In the BBN framework this discrepancy has no resolution. In BFUT, lithium-7 participates in ongoing reactions throughout the lifetime

of every star in which it is present. The dominant destruction reaction is confirmed and directly observed:

This reaction proceeds at temperatures above approximately 2.5×10^6 K, conditions present throughout stellar interiors across their full lifetimes. The rate equation for lithium-7 in steady state is:

$d[Li\text{-}7]/dt = R\_production - k\_dest \times [Li\text{-}7] \times [p] = 0$

giving the steady-state equilibrium abundance:

[Li-7]_eq = R_production / (k_dest × [p])

This steady-state value naturally produces lower lithium-7 than BBN's frozen snapshot, consistent with the observed abundance. The cosmological lithium problem is not a problem for BFUT. It is a prediction.

5.3.4 Deuterium as a Dynamic Abundance Instead of a Primordial Relic

The BBN argument for primordial deuterium rests on the observation that stars destroy deuterium at temperatures above approximately 5×10^5 K, a confirmed early phase of stellar evolution. The argument proceeds: stars destroy deuterium; therefore the deuterium observed today must have been produced before stars existed; therefore it is primordial. This argument commits a logical error that becomes visible the moment it is stated in a different domain.

Stars destroy deuterium. Living organisms consume oxygen. The atmosphere nonetheless maintains a steady-state oxygen concentration of 21%, not because oxygen is primordial, but because photosynthesis continuously replenishes what respiration and combustion consume. To argue that deuterium must be primordial because stars destroy it is precisely equivalent to arguing that atmospheric oxygen must be primordial because organisms consume it. The argument identifies a consumption mechanism and concludes a primordial source is required, without asking whether a continuous production mechanism exists.

A continuous production mechanism for deuterium exists and is confirmed. Cosmic ray spallation, specifically high-energy cosmic ray protons striking carbon, nitrogen, and oxygen nuclei in the interstellar medium, continuously produces deuterium. This process is directly observed and measurable. Additionally, specific stellar environments including the outer layers of certain stars and supernova shockwaves produce deuterium that is ejected into the interstellar medium before being destroyed.

In BFUT, the observed deuterium abundance is the steady-state equilibrium between continuous production and continuous destruction. The observed gradient, higher deuterium in pristine unprocessed gas clouds and lower in regions of high stellar activity, is direct evidence that deuterium abundance is dynamic and ongoing, not primordial and frozen. This gradient is precisely what BFUT predicts.

5.3.5 The Universal Prediction and Epistemological Asymmetry

The thermonuclear reaction rate equation contains only fundamental constants: the fine structure constant, the reduced Planck constant, the speed of light, the proton mass, and the Boltzmann constant. These constants are identical everywhere in the observable universe, confirmed by spectroscopic observations of atoms in galaxies billions of light years away showing identical spectral lines to atoms measured in terrestrial laboratories. Because the nuclear physics governing elemental abundance ratios depends only on these universal constants and on temperature and density conditions determined by gravitational physics, which is equally universal, the same abundance ratios will emerge in every stellar nursery in the infinite universe.

This is a specific, falsifiable prediction: measure elemental abundances in stellar nurseries and gas clouds across the observable universe at every accessible redshift. BFUT predicts the same equilibrium ratios everywhere. Variations will reflect differences in stellar processing history, not differences in the underlying physics. Every spectroscopic observation of a distant galaxy

confirming identical atomic spectra is a confirmation of the universality of the nuclear physics that BFUT's steady-state framework requires.

A further asymmetry must be acknowledged. Neither BFUT nor ΛCDM derives elemental abundance ratios from first principles independently of observation. The universe produced what it produced; that production is observed, and the question becomes whether a given framework is consistent with the observation, whether it contradicts it, and whether it explains it through mechanisms that are themselves independently confirmed. On this standarD and ΛCDM are not equal. ΛCDM presents parameter-fitted calculations as first-principles derivations and still fails on lithium-7. BFUT presents its consistency with observations honestly, explains the mechanisms through confirmed ongoing physics, covers infinite scope, and resolves the lithium problem that ΛCDM cannot.

The ΛCDM model's BBN predictions apply only to the observable universe and depend on a framework whose foundational premises Section 2 has shown to be logically untenable. BFUT's steady-state nucleosynthesis prediction applies to the entire infinite universe. It is the more general framework, derived from more general physics, and it is more consistent with the full body of observations including the one that BBN gets wrong.

5.4 Large-Scale Structure

The filamentary large-scale structure of the universe, the cosmic web of galaxy filaments, sheets, and voids, is explained in BFUT through the gravitational dynamics of matter accumulation and sorting across effectively unlimited time. Gravitational attraction draws matter into filamentary structures along lines of least resistance between accumulation centres. The resulting web structure is the natural end state of gravitational dynamics in a long-lived matter distribution and does not require a special invisible scaffolding component to appear suddenly after a singular origin. In BFUT, the cosmic web is the revealed architecture of a pre-luminous universe, not a hurried post-origin construction.

5.4.1 The Cosmic Web as Pre-Luminous Gravitational Architecture

In ΛCDM, large-scale structure is commonly treated as requiring dark matter scaffolding to explain why matter consolidated into filaments as quickly as it apparently did after the Big Bang. BFUT rejects the claim that dark matter is uniquely required for this role. In an infinite and effectively eternal universe, there is no need to assume that large-scale structure must emerge rapidly from near-featureless initial conditions after a singular beginning. A long cold and dark pre-luminous phase allows matter to spend immense timescales accumulating, clustering, stretching, and organizing before major luminous flare-up phases occur.

Under such conditions, matter arising from quantum fluctuations in the Spaticle field accumulates around local centres of mass. As those centres grow, they draw in diffuse hydrogen from the surrounding volume. Objects on intersecting trajectories merge or are deflected. Matter consolidates along lines of least resistance between accumulation centres. Over timescales far exceeding the 13.8 billion years assumed by ΛCDM, this process naturally produces a filamentary skeleton of clusters connected by strands and separated by vast voids. The Big Flare-Up did not create this structure. It illuminated it. The architecture of the cosmic web was already woven in darkness before the first widespread luminous phase in the local region. This is why JWST observations find mature, structured galaxies at redshifts $z > 10$, where ΛCDM predicts only primitive early structure. In BFUT there is no puzzle. The structure was not young at $z > 10$. It was already ancient.

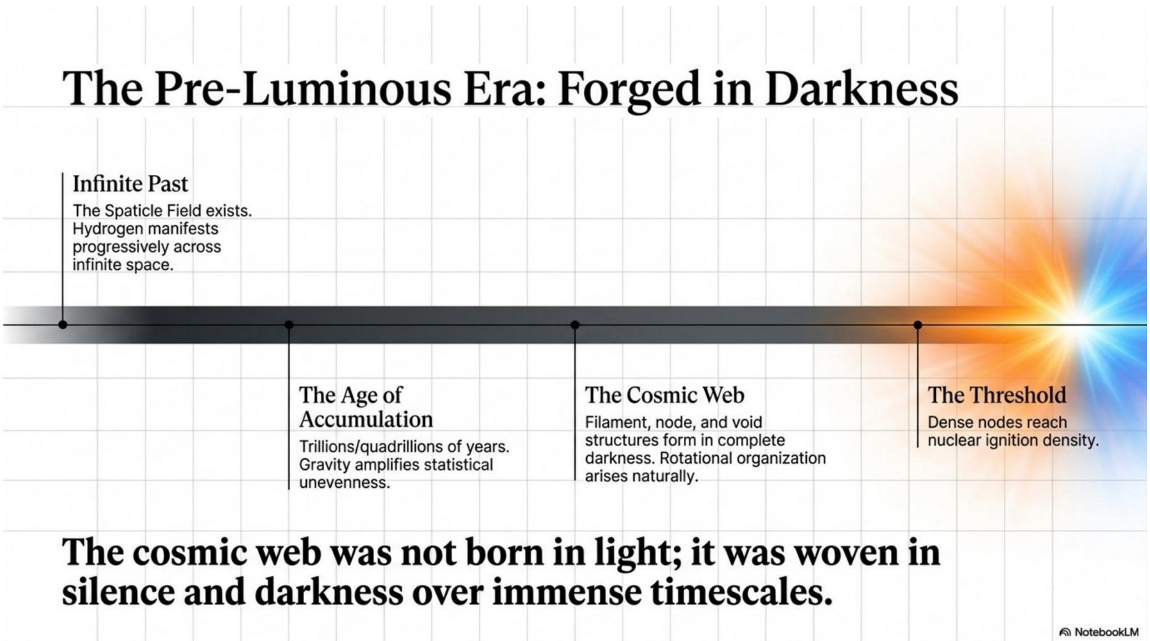

Figure 14. Evolution of the universe during the pre-luminous epoch preceding the Big Flare-Up.

5.4.2 Simulation Evidence for Pre-Luminous Web Formation

This claim was tested through staged structural simulations in which matter was allowed to evolve under pre-luminous conditions prior to widespread ignition. The purpose of the simulations was not merely to generate visually filamentary patterns, but to test whether large-

scale web-like organization could arise before the onset of major luminous flare-up phases. Across the staged runs, matter repeatedly organized into extended filamentary and node-linked structures before any imposed luminous phase.

The master-paper point is decisive: a web can be woven before widespread light. That alone breaks the standard claim that dark matter is uniquely required as the architect of the cosmic web. This is a flagship BFUT result because it attacks one of the deeper functional roles of dark matter in ΛCDM, not merely one of its most popularized applications. Additional simulation stages, fuller parameter variations, and the extended pre-luminous structural analysis are given in the companion paper [P8].

5.4.3 The S8 Tension as a Signature of Suppressed Structure Growth

The S8 tension is often treated within ΛCDM as a nuisance discrepancy to be domesticated by parameter adjustment. BFUT treats it differently: as a potentially diagnostic feature. If structure growth is being suppressed relative to standard expectations by rotational support, long-timescale persistence, or non-standard growth pathways, then the observed weak-lensing discrepancy is not merely an embarrassment but a clue that the standard growth history is being over-imposed on the data.

The master-paper point should be stated sharply. In several standard analyses, when an observable would naturally weaken the preferred inference, an ad hoc corrective relation is often introduced that restores the favoured conclusion by construction. This is one of the ways in which ΛCDM frequently appears more resilient than it truly is: the model survives because the interpretation is repeatedly repaired to keep it alive. BFUT therefore reads the S8 tension not as a bookkeeping inconvenience, but as one member of a broader pattern in which model-preserving adjustments are treated as explanatory success.

Within BFUT, the natural bridge is straightforward: if a living cosmic web, persistent rotational support, and long-timescale structural inheritance suppress clustering amplitude relative to standard expectations, then S8 becomes signal. The fuller weak-lensing discussion, concrete examples of model-preserving corrective practice, and the extended quantitative analysis are given in the companion paper [P13].

5.4.4 The Gunn-Peterson Trough as an Absorption Percolation Threshold

The sharp rise in Gunn-Peterson opacity is often treated as though it directly reveals a one-time global reionization frontier. BFUT contests that inference. A sudden observational transition does not, by itself, prove a single universal epochal wall. In a structured absorber field, line-of-sight visibility can collapse sharply once enough absorbers accumulate, even though no unique ontological boundary has been reached.

A direct flagship simulation was therefore constructed to test whether a present-universe threshold in absorber overlap can generate a Gunn-Peterson-like opacity rise without invoking metric expansion, a cosmological phase transition, or an imposed reionization redshift. A proof-of-concept synthetic sightline was built using a nominal redshift-like coordinate from $z =$
4.5 to $z = 7.0$ purely as an ordering proxy along the line of sight. Along this coordinate, the absorber encounter rate, characteristic optical depth, and characteristic width were all allowed to increase smoothly as power-law functions of position. No discontinuity was inserted anywhere in the model.

The simulation placed 200 absorber components with centres biased toward the high-z end of the sightline using a power-law distribution. Each absorber was assigned a Gaussian optical-depth profile whose peak depth and width scaled smoothly with position. The optical-depth field was convolved with a mild smoothing kernel representing instrumental response, and transmitted flux was computed as $F = \exp(-\tau)$.

The proof-of-concept simulation result is numerical and seed-specific. For seed 1201, the low-z bin mean flux at $z \sim 4.55$ was 1.000, while the high-z bin mean flux at $z \sim 6.95$ fell to 0.042. Both the $F < 0.20$ and $F < 0.10$ thresholds were crossed within the same transition bin centred near $z \sim 6.35$. The maximum steepening in effective optical depth, $d(\tau_{eff})/dz$, reached 15.3 per unit redshift at $z \sim 6.65$.

An analytic covering-factor proxy $C = \lambda \times w_{eff}$ rose to approximately 11.8 near the maximum steepening bin. The central point is decisive: a smooth absorber gradient, with no imposed epoch boundary, produced a sharply localized collapse in transmitted flux in the same broad redshift neighbourhood usually cited as the canonical Gunn-Peterson transition.

Two additional supporting simulations strengthen the conclusion. First, modest absorber-density changes of only 0.78×, 1.00×, and 1.25× baseline shifted the apparent onset redshift across a span of approximately 0.9 in z, which is exactly the signature of an environment-sensitive threshold. Second, a non-expanding velocity-structured sightline using a velocity axis from 0 to 50,000 km/s, populated by 60 weak absorbers and 12 stronger absorbers with a proximity-effect clearing near the source end, produced 42 resolved absorption minima, mean transmitted flux 0.965, and effective optical depth 0.036, showing that a Lyman-α-like forest can arise without metric expansion. A further trough non-uniqueness demonstration showed that diffuse (180 absorbers), clustered (89 absorbers), and patchy (100 absorbers) absorber architectures all produced nearly identical strong-suppression classes, with mean transmitted flux around 0.100 and effective optical depth around 2.305, within 0.3% of one another.

A useful analogy makes the logic immediately clear. In a vast sparse jungle, one initially sees through the gaps and knows the forest continues. But beyond some distance, the accumulated trunks and foliage close the visible gaps, and one can no longer see farther, even though the forest has not ended. The same logic applies here: loss of line-of-sight visibility beyond a threshold distance does not prove that the universe itself changes ontological state at that exact location. The fuller simulation set, additional figures, and the extended opacity mathematics are given in the companion paper [P11].

5.5 Apparent Accelerating Expansion

As noted in Section 5.5, the peer-reviewed analysis by Colin et al. (2019) identifies significant directional anisotropy in the supernova data underlying the dark energy hypothesis, with the apparent acceleration consistent with a bulk flow artifact. BFUT's gravitational sorting mechanism provides a natural explanation for the bulk flow: the local region of the universe is a gravitationally coherent structure moving in a specific direction relative to the large-scale background, producing an apparent asymmetry in recession measurements that has been misidentified as universal acceleration.

Figure 15: Dark Energy Illusion simulation with bulk flow set to 550 km/s - matching the known CMB dipole velocity of the Local Group. Left panel: simulation controls and parameters. Right panel: the Hubble diagram and dipole plot showing the apparent dark energy signal and directional asymmetry consistent with Colin et al. (2019). The signal is produced entirely by observer motion with no dark energy in the physics. Simulation: vijayshankarsharma.com/acceleration

Late-time luminosity relations should not be treated as raw direct measurements of cosmic ontology. Once bulk-flow effects, line-of-sight environment, and model-dependent calibration chains are acknowledged, the apparent acceleration signal ceases to function as a uniquely decisive proof of a dark-energy-driven expanding metric_vss therefore treats the acceleration claim as a major interpretive question, not a closed case.

The inference of late-time cosmic acceleration is often presented as though it were almost interpretation-free. BFUT contests that claim directly. An embedded observer in a structured universe need not infer the same large-scale kinematics as an idealized observer in a perfectly homogeneous and isotropic model. If the observer is situated inside a coherent bulk-flow environment, the inferred recession pattern can be materially distorted in a way that mimics or amplifies an apparent acceleration signal.

To test this, a dedicated bulk-flow simulation was constructed to ask a specific but crucial question: can observer bulk flow alone generate a strong apparent directional dipole signal in a synthetic Hubble-flow sample, even when no dark-energy term is present in the simulation physics? The simulation began with a synthetic isotropic Hubble-flow population. An observer was then embedded in a region moving at 550 km/s relative to the background, aligned with the CMB dipole direction. The resulting line-of-sight velocity perturbations were computed, and the induced directional asymmetry was measured using hemisphere-split Hubble slopes and a residual dipole statistic. The setup was intentionally conservative as a mechanism demonstration and not a full cosmological likelihood pipeline: it did not include supernova intrinsic scatter, observational covariance, or a full q0 fit. The only imposed asymmetry was the observer bulk flow itself.

The result was decisive. With the 550 km/s observer bulk-flow term included, the simulation produced a strong directional dipole signal. When the bulk-flow term was set to zero while leaving the rest of the simulation unchanged, the directional signal collapsed. That control is the key strength of the exercise: the same synthetic Hubble-flow population, under the same statistical logic, ceases to show the anisotropic signal once the observer-motion term is removed. In other words, observer bulk flow alone is sufficient to generate the kind of directional asymmetry often treated as evidence that the standard acceleration inference is reading the universe cleanly. This does not deny the observed supernova pattern. It demonstrates that the apparent acceleration signal is not robustly observer-neutral and can be materially shaped by the kinematic state of the observer relative to the surrounding flow field. Extended numerical treatment and the fuller Pantheon+ directional analysis are given in the companion paper [P4].

5.6 Olbers' Paradox

Olbers' Paradox asks why the night sky is dark if the universe is infinite and filled with stars. The paradox is not resolved by the inverse-square law alone: in a homogeneous infinite static universe, the number of sources in a spherical shell grows as r^2 while the flux from each source falls as $1/r^2$, so the two factors cancel. BFUT instead invokes the physical structure of its universe - finite luminous source occupation, finite luminous lifetimes, absorption and re-radiation, and a continuously evolving substrate. The dark sky therefore depends on the transport and source-history properties of the model, not on inverse-square dilution by itself.

The relevant BFUT mechanisms must therefore be distinguished from unsupported universal statements about individual systems. Many galaxies contain central compact objects, and many stellar systems contain planets, dust, or other absorbing material, but none of these is universal. A quantitative BFUT treatment of Olbers' Paradox must evaluate the source luminosity density, covering and absorption probability, photon propagation, and re-radiation over the relevant path lengths. No paradox follows once those physical processes are included, but the inverse-square law alone is not sufficient to establish convergence.

5.7 Cosmic Rotations Across Scales

Rotation should not be treated as an occasional nuisance detail confined to local systems. Across scales, recurrent angular momentum and rotational order point toward a broader structural principle. If rotational persistence repeatedly appears in the organization of matter, then it becomes increasingly difficult to dismiss it as incidental while preserving a model that heavily depends on short timescales and tightly constrained formation windows.

A dedicated proof-of-principle simulation sequence was therefore developed to test whether gravity alone, starting from random initial positions and velocities in three dimensions, can spontaneously generate persistent orbit-like capture without any imposed circular motion, no expansion term, and no artificial stabilizing force. The simulations were intentionally framed as proof-of-principle demonstrations. Their purpose was not to reconstruct the entire universe, but to test whether rotational and orbit-like ordering can emerge naturally from unsorted gravitational motion.

The simulation proceeded in two methodological phases. First, a whole-system search across multiple random seeds was performed to identify the strongest naturally emerged candidate pair by tracking separation through time, counting periapsis passages, and monitoring the sign of relative angular momentum. The strongest candidate was found for seed 104, pair (9, 38), with 4 periapsis passages, 0 angular-momentum sign flips, 153 qualifying frames, and strong persistence. Second, a focused local rerun retained that naturally emerged pair together with only its nearest few perturbers and evolved the local system for longer. This produced the cleanest near-isolated case: local body count 6, local IDs [9, 32, 36, 38, 41, 57], again 4 periapsis passages, 0 angular-momentum sign flips, 33 qualifying frames under the strict filter, mean perturbers 0.0186, and final separation 1.226 in simulation units.

The correct conclusion is not that every astrophysical system must reduce to a two-body binary. The simulation establishes the more fundamental point relevant to BFUT: from random unsorted motion, gravity alone can produce sustained orbit-like behaviour and local

hierarchical ordering without any imposed orbital geometry. That is the proof-of-principle needed for the broader rotational argument. The more often such order persists across scales, the less natural it becomes to treat the 13.8-billion-year age ceiling as a robust inevitability. The extended simulation sequence and stricter quantitative diagnostics are given in the companion paper [P9].

5.8 The Physical Origin of the Cosmological Constant

The history of the cosmological constant illustrates how one theoretical interpretation can be replaced by another. The BFUT analysis of the dark energy interpretation, set out in companion paper P4 and Section 5.5 below, argues that the apparent acceleration can arise from observer bulk motion and not a universal accelerating metric. The physical interpretation of Λ is treated separately in the covariant substrate analysis below.

5.8.1 The Isotropic Cancellation of Gravitational Force

The same discrepancy can be stated in energy-density terms directly. The standard QFT estimate is of order 10^{111} joules per cubic metre in the convention used by P2, while the observed effective vacuum energy density is approximately 10^{-10} joules per cubic metre. This is the approximately 10^{121} discrepancy discussed in P2. BFUT attributes the discrepancy to the multiplicity and empty-mode attribution in the standard calculation and instead identifies the physical vacuum with the equilibrium substrate density $\rho_s c^2$.

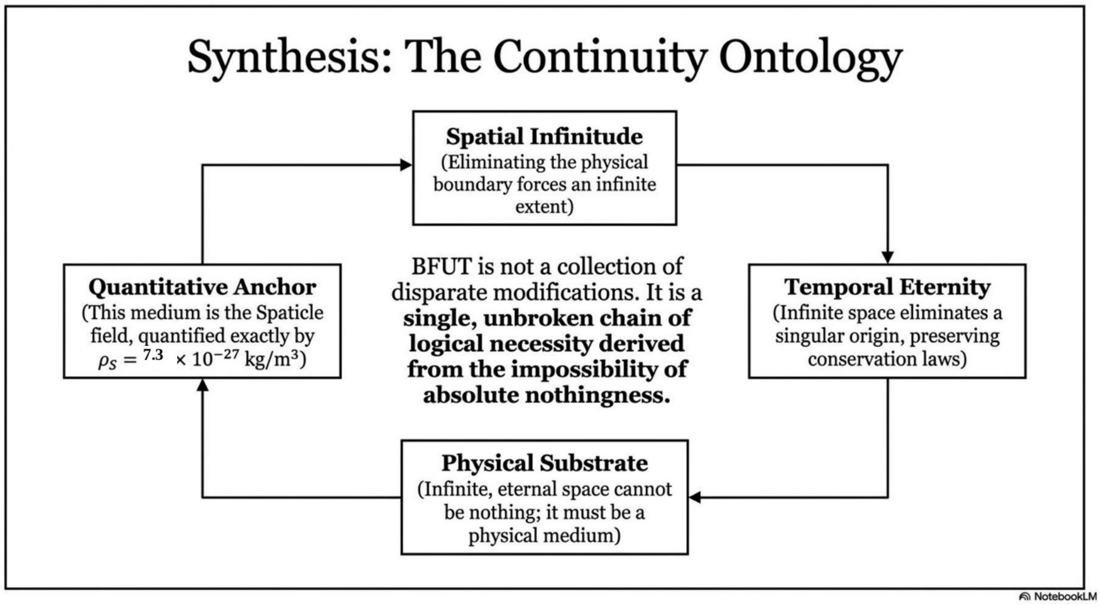

Figure 16. Continuity ontology forming the conceptual foundation of the Big Flare-Up Theory.

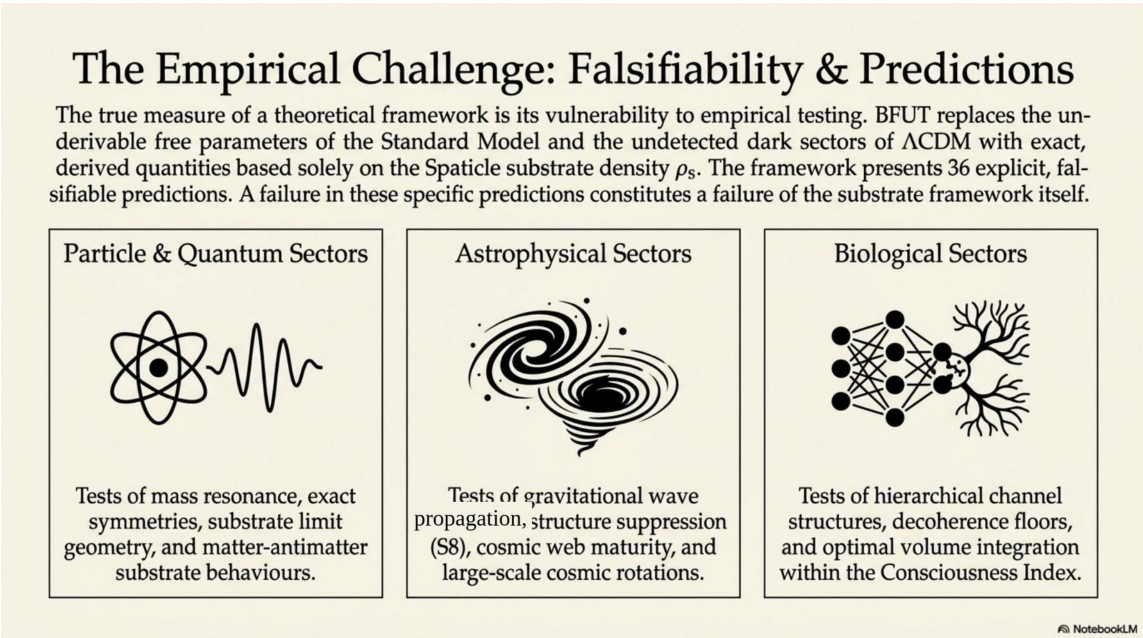

Figure 17. Principal observational tests and falsifiable predictions of the Big Flare-Up Theory.

6. Predictions (see Appendix B. Mathematical and Non-Mathematical Predictions)

The mathematical predictions include the condensation minimum R_0, particle-mass and coupling relations, independent R_0 and c reconstructions, the equilibrium matter-substrate density ρs, substrate stiffness, acceleration scale a_s, finite deformation domains, DME and its asymptotic consequences, carrier attenuation and relaxation, photon persistence thresholds, compact-object bounds, cross-scale identities and the quantitative S8 result. The non-mathematical predictions include centrality, rotational entrainment and sustenance, environmental effects, antimatter behaviour, CMB equilibrium, cosmic redshift, Lyman-α and ISW interpretations, S8 redshift dependence, merger morphology, low-dark-matter systems and finite-core compact objects.

The prediction programme is presented in Appendix B, “Mathematical and Non-Mathematical Predictions.”

The appendix is part of this synthesis and contains the complete numbered set of mathematical and non-mathematical predictions arising from the companion papers.

7. ΛCDM Tension Resolutions (see Appendix C. Mathematical and Non-Mathematical Resolutions of ΛCDM Tensions)

The mathematical resolutions include the vacuum-energy relation, finite gravitational domains, DME and its deep-regime limit, weak-lensing response, particle-mass and coupling relations, the origin of c, common photon and gravitational-wave propagation, relativistic time dilation, finite compact-object density, S8 suppression and the finite-range carrier correction. The non-mathematical resolutions include dark-matter effects, dark-energy-like acceleration, the Hubble relation, horizon and flatness, early structure formation, the CMB, lithium, Lyman-α, ISW, compact objects, information retention, merger morphology, cosmic redshift and low-redshift inference.

The ΛCDM tension-resolution programme is presented in Appendix C, "Mathematical and Non-Mathematical Resolutions of ΛCDM Tensions." The appendix is part of this synthesis and contains the complete numbered treatment.

8. A Recurring Methodological Concern: Non-Unique Inference

A recurring methodological error in modern cosmology is the transformation of successful model-fitting into claims of unique historical causation. Many of the most famous ΛCDM "proofs" are not direct proofs of the model's causal story; they are demonstrations that the model can fit a class of observations under a particular interpretive framework. That is a much weaker statement. A fit is not a monopoly.

The upgraded BFUT program repeatedly targets this exact weakness. The question is not whether ΛCDM can be made to reproduce a phenomenon. The question is whether the phenomenon, by itself, uniquely forces the standard causal narrative. In paper after paper, that stronger claim fails. Hubble-like recession can arise from gravitational sorting; apparent acceleration can be distorted by observer bulk flow; a nearly uniform and weakly anisotropic background can arise in dynamic equilibrium; preferred scales can emerge from shell injection and damping; a Gunn-Peterson-like threshold can arise from absorber percolation without a unique global epoch boundary; and the cosmic web can form before widespread luminous ignition without dark matter being uniquely required as its scaffold.

This is why the correct methodological posture is not that every standard result has been disproved in a simplistic sense. The stronger and more accurate statement is that a large fraction of the standard framework's most rhetorically powerful inferences are non-unique. Once that is understood, ΛCDM is no longer protected by the aura of inevitability that textbook presentation often gives it. The full technical inventory of such non-unique inferences, including further examples and deeper quantitative treatment, is developed across the companion papers.

9. The BFUT Simulation: A Falsifiable Prediction and an Invitation

BFUT is not presented here merely as a verbal reinterpretation of cosmological data. It makes explicit simulation-level claims. If large-scale organization, apparent recession structure, rotational hierarchy, and related observational signatures can be reproduced qualitatively under BFUT-style assumptions without invoking the standard dark-sector package, then the framework becomes empirically vulnerable in a stronger and more useful way than a purely rhetorical alternative model.

Four proof-of-concept simulations have been developed and are available as open-source interactive demonstrations. All are implemented in standard JavaScript with no external dependencies. Source code is published openly for inspection, modification, and extension by any researcher. Python reference implementations are available for researchers who prefer a scriptable environment. (1) The full Big Flare-Up universe simulation is available at vijayshankarsharma.com/bfut. It demonstrates pre-ignition gravitational sorting, the Big Flare-Up cascade, post-ignition thermal equilibrium, vortex formation, and CMB temperature tracking. (2) A vortex formation simulation is available at vijayshankarsharma.com/vortex, demonstrating that gravitational vortices form naturally from confirmed physics alone across all three proposed formation mechanisms. (3) A galaxy gravitational sorting simulation demonstrating the emergent Hubble Law is available at vijayshankarsharma.com/gs. This simulation has been independently verified: N=200 galaxies with random initial conditions produce Pearson r = 0.675 between distance and recession velocity after sorting, with 84% of surviving galaxies receding. Verified on Google Colab. (4) A flat rotation curve simulation demonstrating vortex dynamics without dark matter is available at vijayshankarsharma.com/rotation. N=200 bodies produce a flat rotation curve with outer-to-inner velocity ratio of 0.71, rising to 0.78-0.85 at larger N. Angular momentum conserved throughout. (5) The Invisible Loom simulation - pre-ignition gravitational sorting producing the cosmic web filament structure before the Big Flare-Up - is available at vijayshankarsharma.com/loom. Hydrogen emerges continuously from the Spaticle field. Gravity forms filaments and dense nodes. The Flare-Up fires automatically when fusion density is reached, cascading along the pre-existing structure and revealing it. Post-ignition, a local Flare-Up demonstrates ongoing star formation. (6) The Highway Analogy simulation - demonstrating gravitational sorting as the mechanism behind galactic recession - is available at vijayshankarsharma.com/highway. Vehicles on incompatible trajectories collide and are eliminated. What remains are sorted parallel streams. The simulation demonstrates visually why Hubble recession does not require expanding space. The complete simulation source code is freely available for download at vijayshankarsharma.com/download-simulations and is permanently archived with a citable DOI at Zenodo: https://doi.org/10.5281/zenodo.19124509 [CD1]. The author invites collaboration from computational astrophysicists with access to supercomputing facilities to design and run the full-scale simulation. The required computing scale - while large - is within reach of existing national and institutional supercomputing resources. The simulation code would need to be built from established

gravitational and hydrodynamic simulation frameworks, modified to remove Big Bang assumptions and implement the periodic boundary representation described above. This is a tractable engineering problem, and the question a full-scale run would settle, whether large-scale structure emerges from these initial conditions without an imposed expansion history, is decisive and falsifiable on its own terms.

The simulation operates under the following conditions: N-body gravitational dynamics as the sole organising force; hydrogen-only initial matter with no seeded structure; periodic boundary conditions in which matter exits one edge and equivalent hydrogen enters from the opposite edge, representing the continuous matter production of the infinite Spaticle field; and a fusion threshold based on local matter density, directly analogous to the Jeans instability criterion. From these inputs, without programming any of the following outcomes, the simulation produces: self-organised clustering and void formation consistent with large-scale structure; a three-phase ignition sequence in which a pre-ignition field of drifting matter self-organises until local density thresholds trigger a cascade ignition event - the Big Flare-Up - after which the field enters a permanently altered post-ignition state; dynamic CMB tracking that holds at 2.725 K in the pre-ignition phase and stabilises near 2.82 K post-ignition; and gravitational vortex formation events in which collapsing high-mass remnants produce void openings and jet ejections, with no singularity. These results are offered as a proof-of-concept demonstration, not as a final validated simulation. The simulation is two-dimensional; timescales are dimensionless and compressed; particle counts are far below the scale required for cosmological fidelity. The simulation is published openly with the specific intention of inviting researchers with access to greater computational resources to extend, challenge, and test these results at scales that would constitute formal validation. The source code is documented and structured to support this extension. Independent replication and scaling of this simulation, using only confirmed physics and hydrogen as the starting condition, constitutes a falsifiable test of BFUT's core claims about emergent structure formation. On Independent Research in Fundamental Science The author notes that the history of science includes numerous instances of fundamental contributions from researchers outside the established academic structures of their time. The value of a theoretical proposal is determined by its logical consistency, explanatory power, and testable predictions not by the institutional affiliation of its author. The present paper is offered in that spirit, and the author's arguments are presented for evaluation on their scientific merits.

10. Discussion

10.1 Relationship to Existing Alternative Cosmologies

BFUT was developed independently from first principles and does not derive from any prior cosmological framework. It is not a variant, modification, or extension of any existing theory. Several earlier cosmological proposals are noted here not because BFUT draws from them but because a reviewer familiar with those proposals may perceive surface similarities that require clarification.

Hoyle, Bondi, and Gold (1948) proposed a steady-state cosmology that also rejected a singular origin and invoked continuous matter creation. That proposal was rejected primarily because of the observed evolution of quasar populations with redshift: distant quasars are more numerous than nearby ones, establishing that the universe looked different in the past. A genuinely static steady-state universe cannot accommodate this. BFUT is not a steady-state theory and does not share this vulnerability. BFUT proposes a genuine historical event, the Big Flare-Up, that permanently and irreversibly altered the universe. The universe before the Big Flare-Up was fundamentally different from the universe after it, and BFUT therefore predicts that the universe looked different at greater distances and earlier times, exactly as observed. The evolution of quasar populations with redshift is fully consistent with_vss. The matter creation mechanism in BFUT is also entirely different: quantum fluctuations in the Spaticle field, not the continuous creation field of the steady-state model. The galactic recession mechanism is also different: gravitational sorting of surviving populations, not recession as a built-in feature of the model. The two frameworks share no mechanisms.

Proposals in loop quantum cosmology such as those of Bojowald (2001) and Ashtekar and Singh (2011) replace the Big Bang singularity with a quantum bounce or pre-Big Bang epoch

. BFUT rejects the Big Bang framework entirely and proposes an infinite eternal universe requiring no quantum gravity regime distinct from the physics of the current universe. These are fundamentally different positions, not variations on a common theme.

Paper 14 [P14]: The Matter Substrate, Which the Big Flare-Up Theory Calls the Spaticle Field, as the Unified Substrate of Physical Reality
P14 provides the cross-programme synthesis connecting the equilibrium matter-substrate density to ten physical sectors spanning particle physics, atomic physics, quantum mechanics, gravitation, galaxies, lensing, light, time and extreme gravity.
Paper 13 [P13]: Weak Gravitational Lensing and the S8 Tension
P13 examines rotational suppression and the dependence of recovered S8 on redshift, scale cuts, tomography, covariance, intrinsic-alignment modelling and sector coverage. Its rotational-collapse demonstration gives

S8=0.7805 versus 0.832 for the radial reference, a 6.2% suppression.

Paper 12 [P12]: The Integrated Sachs-Wolfe Effect

P12 models the ISW signal through local matter-substrate temperature variations coupled to density structure, using $T\_local=T_0(1+\alpha\delta)$. Reported simulations produce approximately 9.86 μK for a supercluster and −8.63 μK for a supervoid, with environment-dependent amplitudes.

Paper 11 [P11]: The Lyman-Alpha Forest and Absorption Percolation

P11 interprets the Gunn-Peterson opacity rise as an absorber percolation threshold. Simulations produce transmitted flux declining from about 1 to 0.042 and cross $F<0.20$ and $F<0.10$ near $z\approx6.35$. Changes in absorber density shift the apparent onset redshift.

Paper 10 [P10]: The Sunyaev-Zel'dovich Effect as Local Substrate Interaction

P10 retains $y=(\sigma\_T/(m\_ec^2))\int P\_e\ dl$ and $\Delta T/T=-2y$ in the Rayleigh-Jeans limit, while interpreting the background as the ambient matter substrate. Hot intracluster plasma interacts locally with that field.

Paper 9 [P9]: Cosmic Rotation Across Scales

P9 develops rotational ordering as a recurring result of gravity. Proof-of-principle simulations begin with random positions and velocities, with no imposed circular motion, and produce persistent orbit-like ordering.

Paper 8 [P8]: Cold, Dark, and Inevitable reconstructs

a long pre-Flare-Up phase in which matter accumulated and gravitationally organised before widespread luminous ignition. The Big Flare-Up is a transition in an existing universe. The paper connects pre-ignition sorting with filament-node-void structure and later ignition.

Paper 7A [P7A]: CMB Acoustic Peaks and BAO

P7A treats the acoustic peaks and BAO preferred scale as real observations whose physical origin is not uniquely fixed by the data. Shell-like gravitational structuring, repeated accretion fronts, density-shell spacing and damping are proposed as mechanisms for preferred scales.

Paper 7 [P7]: Dynamic Thermal Equilibrium as an Alternative Origin for the CMB Temperature

P7 identifies the CMB temperature as dynamically maintained thermal equilibrium. $T=(u\_CMB\ c/(4\sigma))^\wedge(1/4)$ gives 2.725 K from the measured CMB energy density. Simulations test near-uniform equilibrium with anisotropy of order 10^{-5}.

Paper 6 [P6]: Black Holes as Central Gravitational Vortices

P6 identifies compact central objects as gravitational vortices within the matter substrate. The Universal Centrality Rule places the primary vortex at the dynamical centre of a settled host system and combines this with finite-core compression and the absence of a physical infinite-density singularity.

Paper 5 [P5]: The Universe Has No Boundary

P5 develops spatial infinitude as a foundational premise. The observable limit is a visibility or causal constraint, not a physical boundary. The same premise addresses the horizon and flatness problems without requiring a finite-origin causal patch.

Paper 4 [P4]: Observer Bulk Flow as an Alternative Explanation for Apparent Cosmic Acceleration

P4 models apparent acceleration as an observer-kinematic effect produced by bulk flow through a structured gravitational environment. A 550 km/s observer velocity aligned with the CMB dipole is used in a controlled simulation; removing the bulk-flow term removes the directional signal.

Paper 3 [P3]: A Steady-State Nucleosynthesis Resolution of the Cosmological Lithium Problem

P3 treats elemental abundances as equilibrium outputs of continuous matter production, stellar nucleosynthesis and recycling. The hydrogen balance is $d\rho\_H/dt=S\_Spaticle-\lambda\_fusion\rho\_H^2$, with $S\_Spaticle=\lambda\_fusion\rho\_H^2$ at equilibrium.

Paper 2 [P2]: Dissolving the Cosmological Constant Problem

P2 identifies the physical vacuum with the equilibrium energy density of the matter substrate, which the Big Flare-Up Theory calls the Spaticle Field. The central relation is $u\_vac=\rho_s c^2$. Empty, unexcited modes do not contribute condensation energy.

Paper 1 [P1]: Gravitational Sorting as an Alternative Mechanism for the Hubble Relationship

P1 proposes that the observed velocity-distance relation can emerge from gravitational sorting in a spatially infinite system. Its survival model uses $P(t)=\exp(-\lambda t)$, while the direct velocity-distance test is supplied by N-body dynamics. The reported proof-of-concept gives Pearson $r=0.675$ and 84% of survivors receding from the observer.

10.2 Companion Papers P1-P14: Cosmology, Structure and Observational Reinterpretation

11. Paper 15 [P15]: What Existed Before Matter and the Spaticle

Field

Paper 15 extends the infinite-universe premise of Paper 5 one step further, asking what existed prior to the Spaticle field itself. Five independent arguments converge on the same conclusion: universal conservation laws prohibit the field's emergence from literal nothing; a spatial metric cannot bootstrap its own underlying extension from non-extension; causality requires a prior condition, since an uncaused first cause violates the same causal structure the standard model otherwise relies on; the thermodynamic arrow of time and the extraordinarily improbable low-entropy initial condition of the standard picture become rationally explicable only under continuity of a prior state; and the laws of physics are themselves a form of information that cannot arise from zero information. The Spaticle field is the manifestation of a prior real energy state of infinite space, not a creation from nothing. The paper closes with a dedicated section formally stating Vijay's Law and the perpetuation principle: everything in the universe is alive and conscious; whenever conditions are stable or predictably unstable at any scale, more evolved matter manifests; all matter possesses a perpetuation drive; and that drive is fulfilled when the combined form is able to perpetuate itself. The same principle is shown to operate at every later stage of emergence summarised in the remainder of this section [1].

P15 establishes ontological continuity through conservation, causal precedence, the inability of a metric to generate its own underlying extension, the thermodynamic arrow of time and the informational content of physical law. It concludes that the matter substrate is a manifestation of a prior real physical state. P15 also formally states Vijay’s Law and the perpetuation principle.

12. Paper 16 [P16]: The Origin of Matter, Antimatter, and Fundamental Forces

Paper 16 derives the proton, the electron, and ordinary hydrogen from the Spaticle field through a four-term condensation functional, using the measured proton charge radius as the SI length anchor and the independently constrained substrate density ρ_s. No fitted model parameter is introduced.

$$E(R) = A/R^2 + B \times R^2 + C \times R + D/R$$

Minimising this functional fixes the dimensionless condensation radius at $R_0 = 1.27348221$. A threshold logic selects a three-core-plus-electron (3+e) topology over symmetric alternatives, the structural origin of charge separation; the resulting proton and electron combine to form hydrogen. A robustness scan of the full free-energy landscape at the n=4 stability threshold identifies exactly three competing configurations: 3+e is preferred across 97.56% of the parameter space scanned, 2+2 across 2.16%, and 4+0 across 0.28%, with no other configuration found stable, establishing the 3+e topology as the dominant outcome.

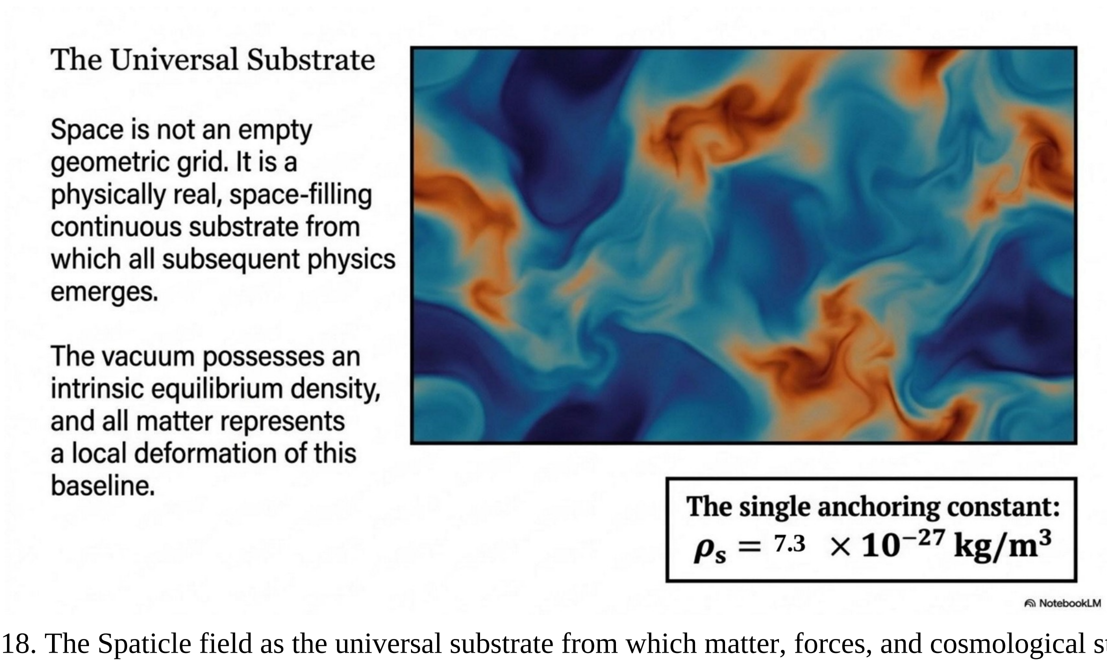

Figure 18. The Spaticle field as the universal substrate from which matter, forces, and cosmological structure emerge.

The same condensation geometry fixes the reduced Planck constant directly:

$$\hbar = m_p \cdot c \cdot r_p / (\pi \times R_0)$$

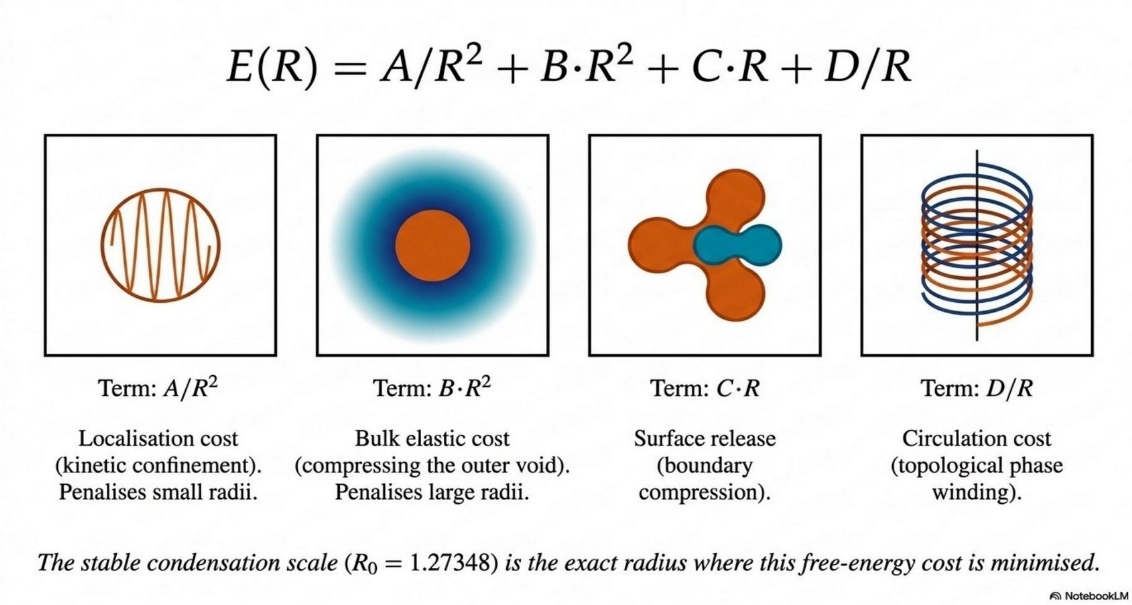

Figure 19. Energy landscape of the BFUT condensation functional illustrating the emergence of stable condensations.

The three-fold rotational topology supplies the geometric structure of the charged-lepton sector. The exact symmetry constraints and the remaining dynamical problem for the full three-generation hierarchy are treated in restricted P29.

The Bernoulli co-rotation mechanism that binds the three-core also derives quark confinement directly: the derived confinement force is F_conf = 0.574 GeV/fm against a measured QCD string tension of 0.9 GeV/fm, an agreement of 64% with no free parameters. The same stability-selection mechanism gives a different physical account of the matter-antimatter asymmetry: the asymmetry arises during the quark stability-selection stage itself, when only a stable excitation fraction persists macroscopically, removing the need for a separate large-scale asymmetry-generation mechanism beyond the stability filter already established for proton formation. This account is developed into specific, falsifiable predictions for the CERN antihydrogen programme in Paper 16A [P16A], including the prediction that antihydrogen falls under gravity identically to ordinary hydrogen and that macroscopic stable antimatter domains will not be produced under ordinary conditions.

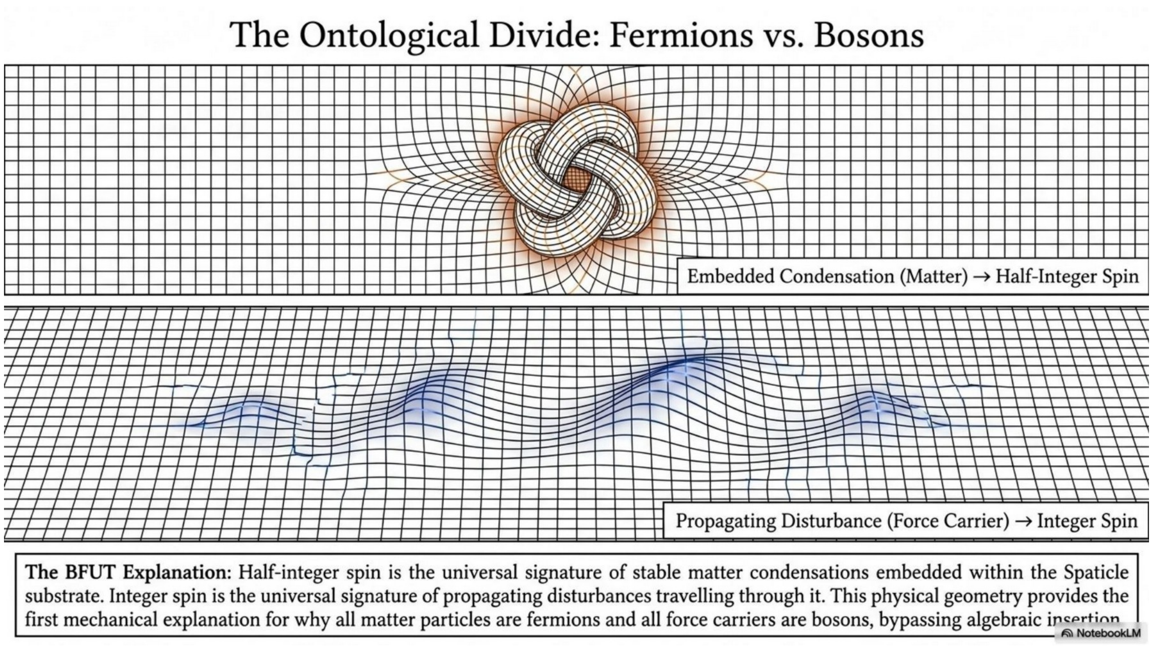

Figure 20. BFUT reinterpretation of fermions and bosons as distinct condensation states of the Spaticle field.

The condensation functional further establishes a general Hierarchy Theorem: once a stable organisational unit forms, further energy reduction proceeds through structural modularity, repeated formation of the same stable unit. This modularity principle is shown to extend across scales, connecting to the filament-node-void cosmic structure established in Paper 8, and gives a physical account of why every electron in the universe has identical mass, charge, and spin: each is an independent instance of the same finite, energetically preferred condensation, not a distinguishable individual object [P16]. A full numerical code deposit accompanies the paper, implementing the condensation functional, the minimisation, and the robustness scan [P16].
The full technical derivations underlying these results are given in the cited companion papers, including P16, P18, P19, P19A, P22, P23, P25, P26, P27, and P28.

The 3+e stability scan gives 97.56% for 3+e, 2.16% for 2+2 and 0.28% for 4+0. The condensation geometry supplies $m\_e/mp=1/(6\pi^5)$ and $\hbar=mpc\ rp/(\pi R_0)$, and the density chain reaches $\rho s=7.3\times10^{-27}$ kg/m³. The stability-filter mechanism supplies the physical basis for the antimatter treatment in P16A.
The condensation functional is $E(R)=A/R^2+BR^2+CR+D/R$. Its coefficients have stated physical and geometric origins: A=1/2 from the localisation term in the adopted model normalisation; B=0.56308 from the bulk-displacement geometry including the void contribution; C=−1/3 from the three-core sharing of the expelled central region; and D=1 from the internal topological circulation normalisation. Differentiation gives $dE/dR=-2A/R^3+2BR+C-D/R^2=0$, or $1.12616R^4-(1/3)R^3-R-1=0$. The stable positive minimum is $R_0=1.27348221$.
The condensation chain therefore connects R_0 to particle masses, the quantum of action and the equilibrium density of the matter substrate, which the Big Flare-Up Theory calls the Spaticle Field. The electron relation is $m\_e/mp=1/(6\pi^5)$, the reduced Planck constant is $\hbar=mpc\ rp/(\pi R_0)$, and the electromagnetic relation is $\alpha=e^2/(4\pi\varepsilon_0\hbar c)$.
With these coefficients, $dE/dR=-2A/R^3+2BR+C-D/R^2=0$ gives $2BR^4+CR^3-DR-2A=0$. Substitution gives $1.12616R^4-(1/3)R^3-R-1=0$ and $R_0=1.27348221$. The particle-sector density is $\rho s=G(m\_e/\alpha)^2/(8\pi r\_e^4c^2)$, with the publication value $\rho s=7.3\times10^{-27}$ kg/m³. The same particle-sector derivation can also be written as $\rho s=[Gc^2/(8\pi\hbar^4)](m\_e/\alpha)^6$.
A, B, C and D are dimensionless coefficients with distinct physical origins. The localisation coefficient is $A=\hbar^2/(2m\_eff)$, which becomes A=1/2 in the model-unit normalisation. The bulk coefficient is obtained from the three-sphere displacement and void geometry: $B=[\pi(d+R)^2-3\pi+A\_void]/[3\pi+A\_void/6]=0.56308$. The boundary coefficient is C=−1/3 because the expelled central region is shared equally by the three identical core components. The circulation coefficient is D=1 in model units, corresponding to $D=\hbar c$ in SI and to the internal topological phase winding.

13. Paper 17 [P17]: The Emergence of Forces and Fundamental Senses

Paper 17 derives all four fundamental forces directly from the structure of the 3+e condensation established in Paper 16, in a fixed emergence order. Gravity emerges first, requiring only mass-energy deformation of the substrate, with no separate mediating particle. The strong force emerges second, when compact three-core condensations are brought close enough that their internal substrate organisation couples directly, giving confinement and short range as direct mechanical consequences. Electromagnetism emerges third, requiring condensations with persistent internal rotational asymmetry; a stationary charge produces a static directional substrate pattern, while a charge in motion or under acceleration produces a time-varying polarised substrate wave, which is electromagnetic propagation itself, fixing the speed of light as the substrate's own maximum propagation speed. The weak force emerges last and is structurally the most demanding of the four: the W and Z bosons are temporary, massive, highly localised substrate excitations that carry internal-reconfiguration information between condensation types, transforming one quark or lepton type into another through a three-stage internal topology reconfiguration; parity violation follows as an asymmetry in the preferred direction of that reconfiguration.
The paper further proposes that all four forces are best understood as a hierarchy of fundamental sensing channels: every physical interaction requires a system to produce a real, physical state transition that either propagates outward as a signal or remains confined, and the four forces in their fixed emergence order constitute the channels through which physical systems can detect and respond to their environment, the foundation extended into the consciousness framework of Papers 20 and 21 [P17].
P17 also identifies the four forces as a hierarchy of sensing channels: gravity provides presence sensing, the strong interaction provides binding, electromagnetism provides identity and distance sensing, and the weak interaction provides transformation-threshold detection.

P17 develops the four interaction regimes in the order gravity, strong interaction, electromagnetism and weak interaction. Gravity is the response to substrate deformation by mass-energy; the strong interaction arises from direct coupling of compact three-core condensations; electromagnetism arises from persistent rotational asymmetry and its propagating polarisation; and the weak interaction involves internal reconfiguration of condensations, with W and Z excitations carrying transformation information and the preferred reconfiguration producing parity asymmetry.

14. Paper 18 [P18]: Beyond General Relativity

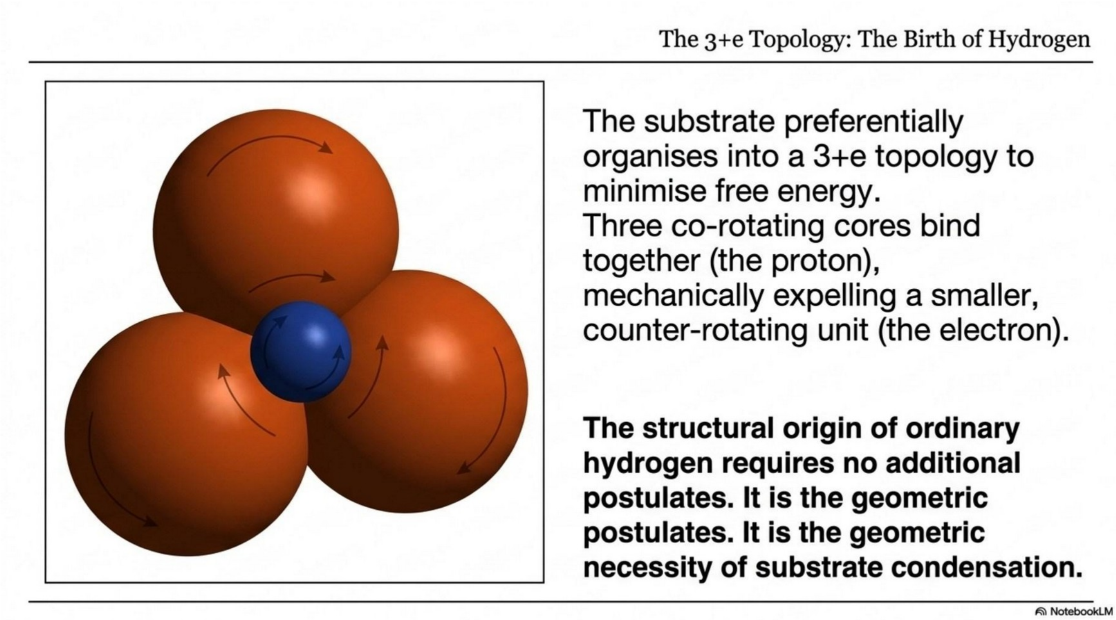

Figure 21. Formation of stable matter through the 3+e condensation topology.

The DDR equation, together with the DME equation for organised rotating and stacked regimes, and every other result of this paper descend from a single, fully covariant carrier field equation for the substrate perturbation delta_Psi, denoted F1-cov:

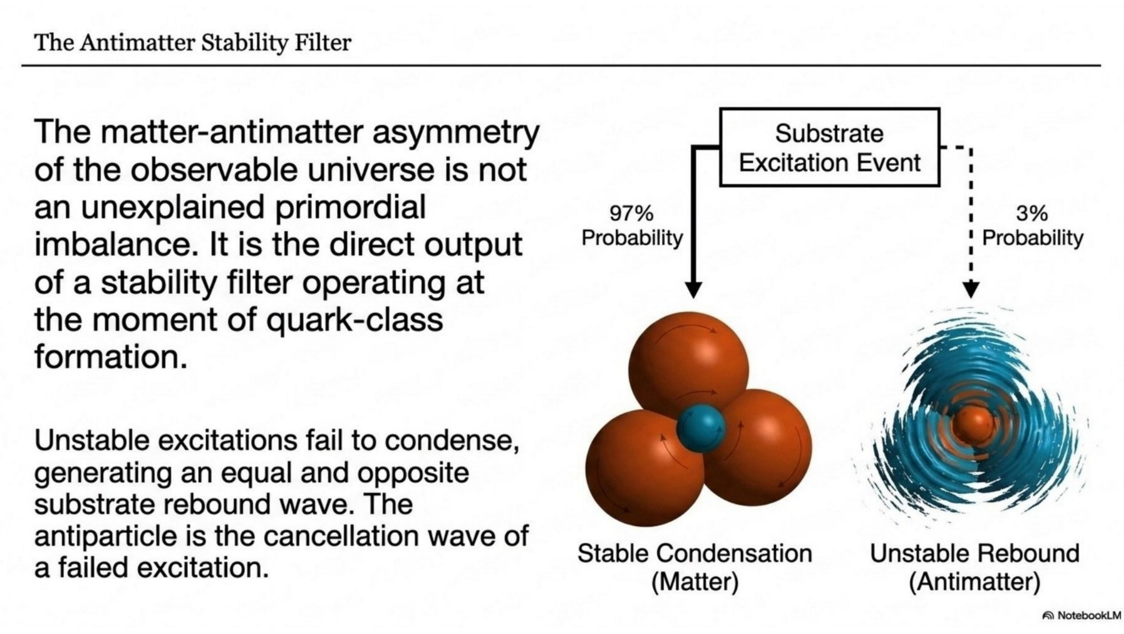

Figure 22. BFUT explanation of matter-antimatter asymmetry through differential condensation stability.

Every coefficient in F1-cov is fixed from first principles: ρ_s from the intrinsic equilibrium substrate density, c from the Spaticle medium propagation speed, and the source coupling from the Paper 17 Lagrangian coupling structure, leaving no free parameters. In settled regimes the equation reduces exactly to standard general relativity; in rapid-transition regimes its non-trivial dynamics produce the finite-response carrier dynamics for transient gravitational disturbances. The DDR domain equation below is the static, weak-field limit of F1-cov.

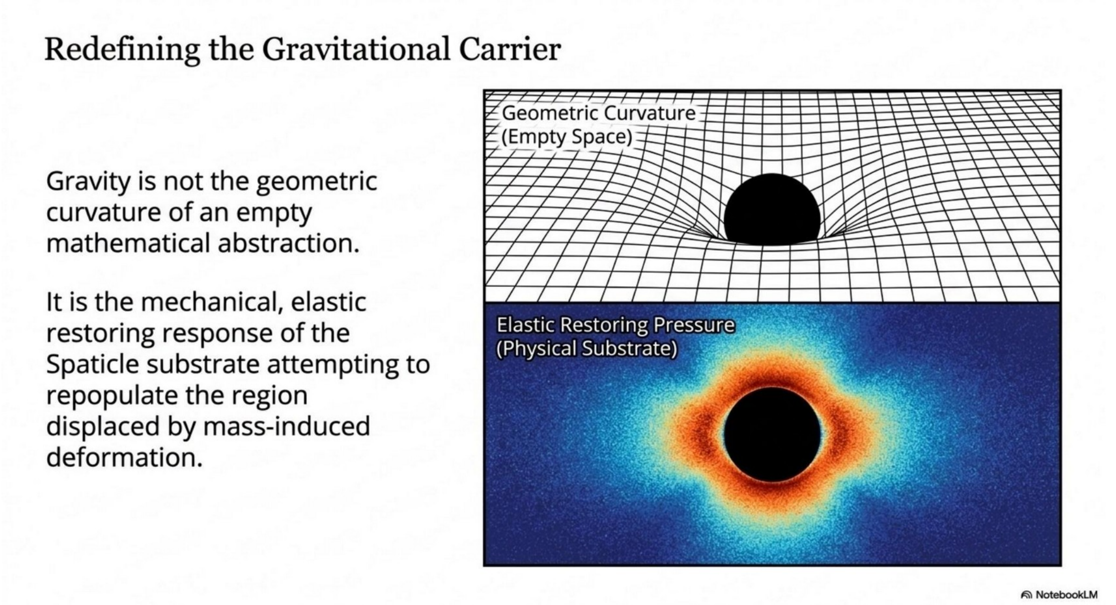

Figure 23. Gravity as substrate deformation compared with the geometric interpretation of General Relativity.

Paper 18 derives a finite-domain gravitational equation, the DDR relation, replacing general relativity's gravitational influence extending to infinity with a domain that terminates at a finite radius set by the substrate density:

$$R_d = (3 \times M / (8\pi\rho s))\text{\^{}}(1/3)$$

with a rotationally enhanced effective domain radius R_eff = $R_d \times (1 + v_{rot}^2/c^2)$^(1/3). The DME equation, $v^2(R) = v_b^2(R)[1 + a_s R / v_b^2(R)]$^(1/2) with $a_s = c(G\rho s/3)$^(1/2) = 1.20840317×10^{-10} m/s², is the operative law that reproduces observed rotation and lensing profiles: using $\rho s = 7.3 \times 10^{-27}$ kg/m³ and no per-galaxy or per-sample free parameter, it reproduces 175 SPARC galaxy rotation curves with a chi-squared of 1.31 (against 1.47 for MOND) and the KiDS-1000 weak gravitational lensing convergence with a chi-squared of 0.007-0.067, against 5.77-6.57 for an NFW dark matter halo fit over the same data.

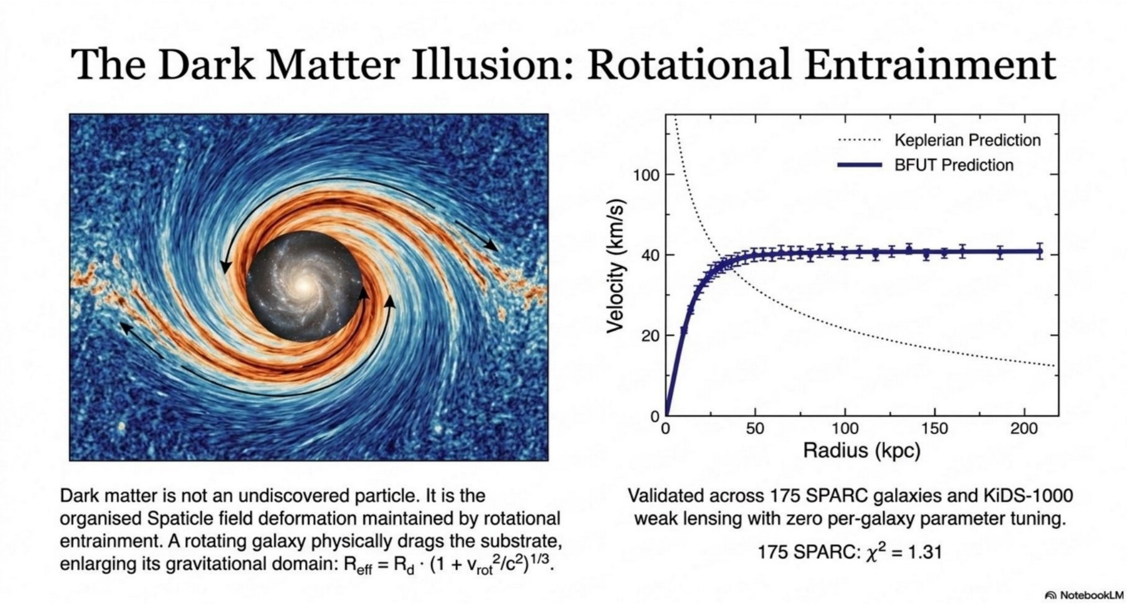

Figure 24. BFUT explanation of flat galactic rotation curves through substrate dynamics without dark matter.

The paper closes by identifying the Spaticle field directly as the physical mechanism behind the dark matter observational programme: the same DDR equation governs both the finite gravitational dominance domain of any astrophysical structure and the rotational enhancement of that domain, accounting for the full body of dark-matter evidence without a separate particle species. P19 derives $m\_Z\_vss = \pi^4 mp = 91.396$ GeV/c² and $m\_W\_vss = 256(mp/3) = 80.066$ GeV/c² independently from the P16 condensation structure. The mixing quantity is then $\sin^2\theta\_W\_vss = 1 - (m\_W\_vss/m\_Z\_vss)^2 = 1 - 256^2/(9\pi^8) = 0.23257$. The H-class radial resonance uses $\lambda\_H\_vss = 2\,A\,R_0 / \pi^2$, $v\_vss = 6E\_unit/\alpha\_vss$, and $m\_H\_vss = v\_vss\sqrt{(2\lambda\_H\_vss)} = 124.75$ GeV/c².
The complete Paper 18 formula derivations are given in P18 and the related validation results in P25 and P78.

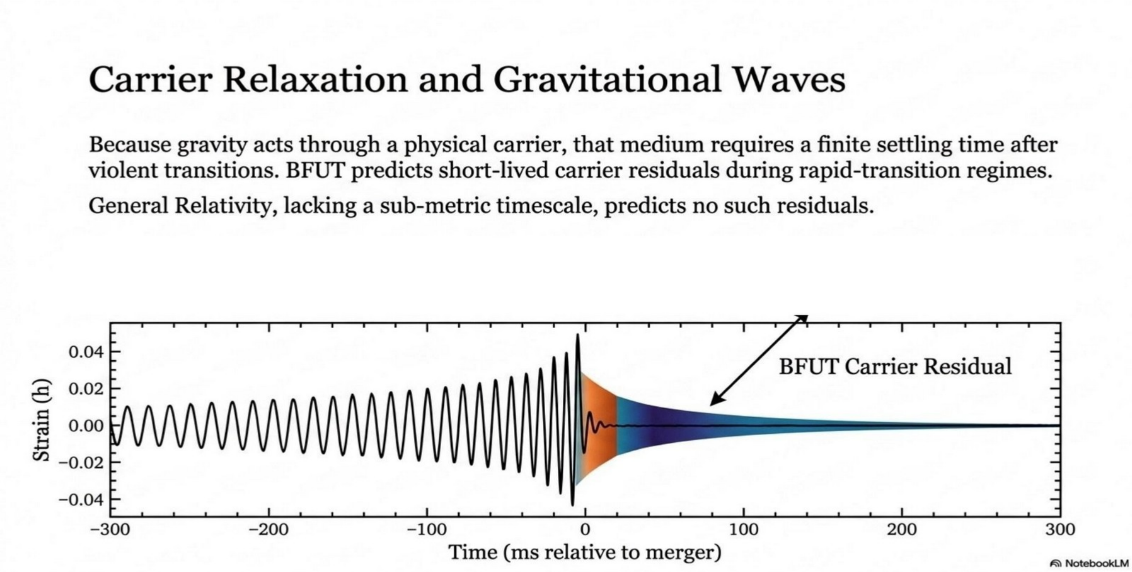

Figure 25. Substrate relaxation following gravitational-wave events and its observational implications.

The settled carrier potential gives $\Psi(r)=-(GM/r)\exp(-r/R\_eff)$, so $g/g\_N=\exp(-r/R\_eff)(1+r/R\_eff)$. The equilibrium carrier scales are L_nat=45.17 AU and τ_nat=6.26 h.
F1-cov is the common covariant carrier equation: $g^{\mu\nu}\nabla\_\mu\nabla\_\nu(\delta\Psi)-3\rho sc^2\delta\Psi=(1/c^2)g^{\mu\nu}\nabla\_\mu\nabla\_\nu\Psi\_matter$. Its static weak-field domain relation is $R_d=[3M/(8\pi\rho s)]^{(1/3)}$, with $R\_eff=R_d(1+v_{rot}^2/c^2)^{(1/3)}$. The organised rotation law is $v^2=v_b^2[1+a_sR/v_b^2]^{(1/2)}$, where $a_s=c\sqrt{(G\rho s/3)}$.

15. Paper 19 [P19]: Unification of Particle Physics

The H-class resonance follows from the P19 radial condensation invariant: $\lambda\_H\_vss = 2\,A\,R_0 / \pi^2$, $v\_vss = 6E\_unit/\alpha\_vss$, and $m\_H\_vss = v\_vss\sqrt{(2\lambda\_H\_vss)} = 124.75$ GeV/c².

The P19 H-class result is the radial resonance of the single Spaticle field, with $\lambda\_H\_vss = 2\,A\,R_0 / \pi^2$, $v\_vss = 6E\_unit/\alpha\_vss$, and $m\_H\_vss = 124.75$ GeV/c².

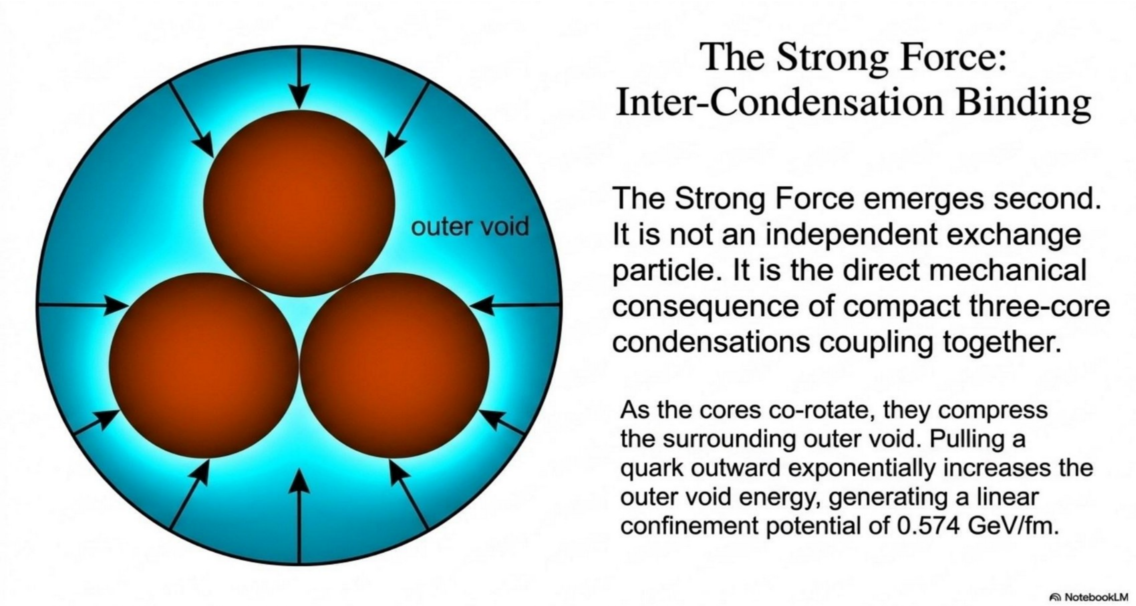

Figure 26. Emergence of the strong interaction from inter-condensation binding within the Spaticle substrate.

The full derivation of the strong coupling constant and the fine structure constant from the shared A, B, C, D coefficients of the Paper 16 condensation functional is given in P19.
The density-derived constants used in the particle-sector synthesis trace to ρ_s. The carrier response time τ_c is a local density-dependent quantity, while the equilibrium natural scale is τ_nat ≈ 6.26 h.

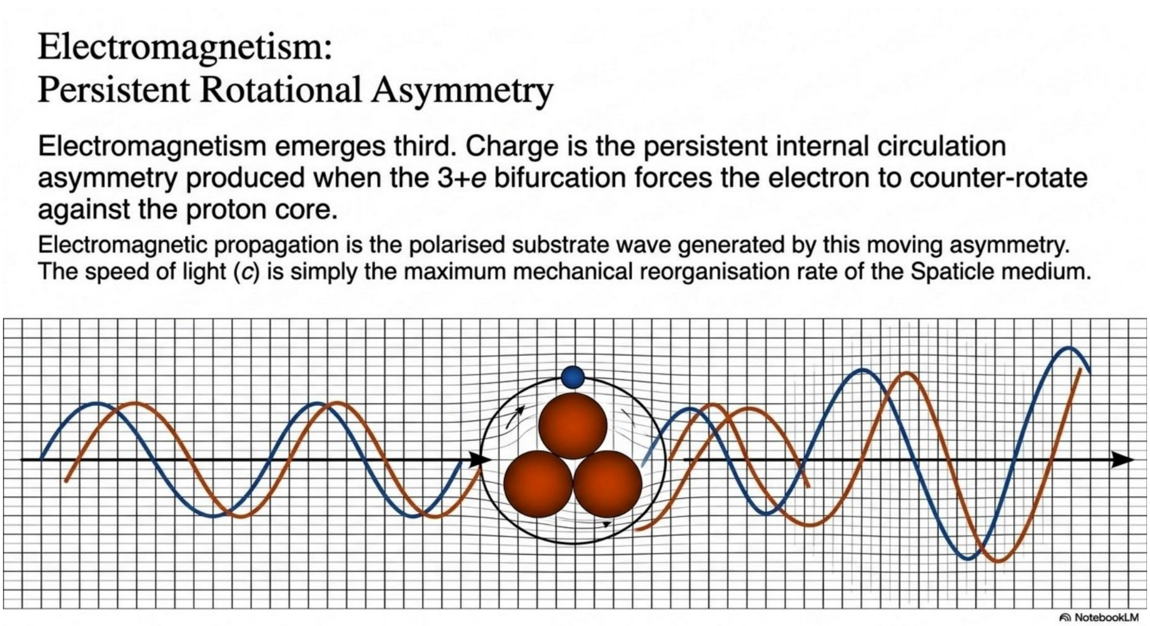

Figure 27. Emergence of electromagnetism from rotational asymmetry within the condensation structure.

The paper further establishes that the metric tensor itself is an emergent description of substrate propagation relations: two events are separated by a given interval when a signal propagating through the substrate connects them, unifying special-relativistic time dilation, gravitational time dilation, the finite speed of light, and the finite speed of gravity as four faces of the same underlying propagation structure. A worked first empirical calibration of the finite gravitational domain equation is carried out for isolated bodies, fixing the dimensional closure constant $k = G/c^2$ directly. Angular momentum quantisation is derived directly from F1-cov: since delta_Psi must be single-valued at every point in space, a logical requirement, the minimum non-trivial circulation state is n=1, and substituting into F1-cov in the Coulomb potential gives the hydrogen radial equation exactly, with bound states existing only at $r_N = N^2 a_0$. Scanning every radius outward from the proton surface, the ratio $L/\hbar$ grows continuously from 0.004 at the proton surface to exactly 1.000 at the Bohr radius a_0 = 52,918 fm, with no integer value occurring at any radius in between, making the Bohr radius the first and only stable orbit outside the proton. The spin-statistics theorem and the Schrödinger kinetic operator are recovered the same way from substrate topology, extended in full in Paper 27 and Paper 19A [5].

The independent R_0 reconstruction is $R_0=4\varepsilon_0 mpc^2 rp\alpha/e^2$. The same consistency chain gives $c^2=e^2R_0/(4\varepsilon_0 mprp\alpha)$, providing the independent numerical reconstruction of c.

The H-class resonance follows from the P19 radial condensation invariant: λ_H_vss = 2 A R_0 / π², v_vss = 6E_unit/α_vss, and m_H_vss = v_vss√(2λ_H_vss) = 124.75 GeV/c².

16. Paper 19A [P19A]: Unifying Quantum Mechanics with Gravity

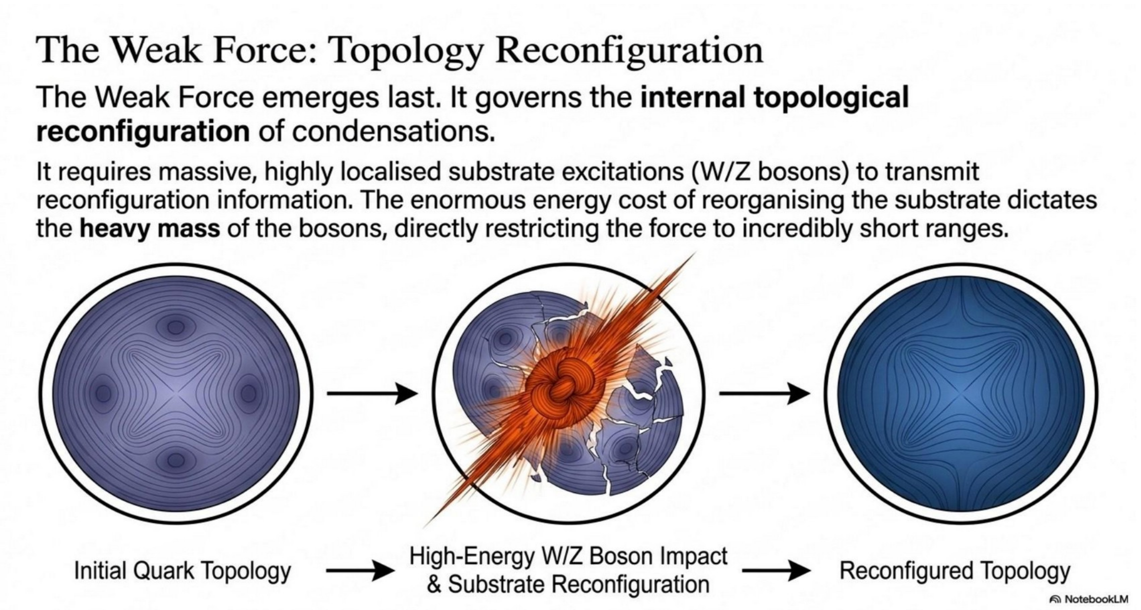

Figure 28. Emergence of the weak interaction through topological reconfiguration of condensations.

Paper 19A extends the substrate framework to demystify twenty separate quantum and gravitational phenomena usually treated as foundational and unexplained, organised in two parts: core derivations, and the BFUT account of major physical interpretations. The Heisenberg uncertainty principle is recovered directly from the same A/R^2 localisation term that prevents matter from collapsing to a point in the Paper 16 condensation functional:

$$\text{Delta}(x) \times \text{Delta}(p) >= \hbar$$

establishing that the uncertainty bound and the stability of matter against collapse are the same underlying energy balance applied to two physical situations, not two separate facts about nature. Quantum tunnelling, the de Broglie wavelength, and the quantum harmonic oscillator energy levels are each given an explicit substrate form by substituting the BFUT ħ directly into their standard formulas:

$$\lambda = mp \cdot c \cdot rp / (\pi \times R_0 \times p)$$

The Born rule's squared-amplitude probability structure, half-integer fermionic spin, the Pauli exclusion principle, wavefunction collapse, superposition, and entanglement are each given a physical mechanism rooted in substrate dynamics; gauge symmetry itself is reinterpreted as local circulation invariance of substrate condensations.

P16A develops the Shankar and BFUT configuration resonances at 776.5 MeV and 1403.7 MeV from the 2+2 and 4+0 excitation gaps. The DDR domain equation of Paper 18 is tabulated for specific physical objects, giving a domain radius of 0.301 m for both the proton and the hydrogen atom (proton mass dominates in both cases), 4.87 light-years for Earth, 337 light-years for the Sun, and 872 kiloparsecs for the Milky Way. The paper closes with an explicit bridge to the consciousness framework of Papers 20 and 21, identifying the same substrate decoherence floor that resolves the quantum-gravity incompatibility as the physical boundary condition underlying the observer problem in quantum mechanics [6].

Cross-Check: Consistency Between the R_0, α, c, and ħ Derivations

The P16 derivation of ħ = mp c rp / (π R_0) and the P19 derivation of α from internal circulation geometry are independent derivation chains, but they share R_0 as a common parameter [P16, P19]. Substituting the BFUT ħ formula into the standard electromagnetic definition $\alpha = e^2/(4\pi\,\varepsilon 0\,\hbar\,c)$ and solving for R_0 gives:

$$R_0 = 4\,\varepsilon 0\,mp\,c^2\,rp\,\alpha / e^2$$

Substituting $e = 1.602 \times 10^{-19}$ C, $\varepsilon 0 = 8.854 \times 10^{-12}$ F/m, $mp = 1.6726 \times 10^{-27}$ kg, $c = 2.99792458 \times 10^8$ m/s, rp = 0.8414 fm (CODATA 2018), and $\alpha = 1/137.036$ gives $R_0 = 1.27348831$. This agrees with the derived $R_0 = 1.27348$ to 0.00048% [P19].

The two derivation chains are mutually consistent. Both ħ and α depend on R_0 through the same proportionality structure. With $R_0 = 1.27348$ fixed from the P16 condensation minimum, the ħ derivation of P16 and the α derivation of P19 converge to their physical values.

The 0.00048% agreement between $R_0 = 1.27348$, derived from condensation geometry alone, and $R_0 = 1.27348831$, extracted from six independently measured physical constants, constitutes a two-way mutual validation. The condensation functional is confirmed as a real physical structure because an empirical route, using only pre-existing measured values, arrives at the same condensation scale [P19].

This cross-check also yields a structural expression for c. Solving the consistency relation for c gives:

This expresses c in terms of R0, e, ε0, mp, rp and α. Numerical evaluation gives c_vss = 2.99791740×10^8 m/s, agreeing with the measured value to 0.0003%. The full treatment of this consistency derivation of c is given in Paper 23 Section 2.4 [P23].

The significance of this result is not that it derives c from nothing. Its significance is that it establishes a non-trivial consistency relation between independently meaningful physical quantities. R_0 emerges from the P16 free-energy minimum without reference to c or ħ, while α, e, ε0, mp, and rp enter through independently established electromagnetic and matter-sector measurements. The resulting agreement shows that the condensation scale, the electromagnetic coupling structure, and the speed-limit structure of the substrate are not separate facts but mutually constraining expressions of the same physical organisation.

Result	Formula	Agreement / Status
ħ derivation	$\hbar = mp\,c\,rp / (\pi\,R_0)$	0.00048% [P16]
R_0 cross-check from α	$R_0 = 4\,\varepsilon 0\,mp\,c^2\,rp\,\alpha / e^2$	$R_0 = 1.27348831$, agreement 0.00048% [P19]
c consistency relation	$c^2 = e^2R_0/(4\varepsilon_0 mprp\alpha)$	c_vss = 2.99791740×10^8 m/s, 0.000239% [P23]
Mutual validation	R_0 from condensation geometry vs. R_0 from measured constants	Two-way agreement; physically meaningful consistency
Physical reading	$c^2 = (e^2/4\varepsilon 0)\,(R_0/mp\,rp)\,(1/\alpha)$	Condensation geometry, electromagnetic coupling, and speed-limit structure are mutually constrained

The paper also connects the DDR domain relation across physical scales and uses the substrate decoherence floor to bridge the quantum and gravitational regimes.

P19A develops quantum-mechanical consequences of the common carrier framework. It gives $\Delta x \Delta p \geq \hbar$, $\lambda = \hbar/p$, angular-momentum quantisation $L = n\hbar$, and substrate-based treatments of tunnelling, harmonic-oscillator levels, the Born rule, half-integer spin, Pauli exclusion, wavefunction collapse, superposition, entanglement and gauge symmetry.

17. Paper 20 [P20]: From Matter and Fundamental Forces to Consciousness

Paper 20 extends the substrate framework past the boundary of physics in the conventional sense, establishing a formal three-condition definition of sensing and the Hierarchical Channel Accessibility (HCA) law. A sensing capability exists in a system if and only if four components are simultaneously present, formalised as a capability equation; the HCA law implies a directly testable Structural Inclusion Principle, demonstrated explicitly across five distinct biological channel types: electromagnetic sensing through photoreception, acoustic sensing through cochlear mechanoreception, immune recognition, interoception, and biomineralization, in each case showing that higher-order sensing capability requires, and is built upon, the lower-order channels. The four fundamental forces derived in Paper 17 are identified as a hierarchy of sensing channels: gravity provides presence sensing, the strong force provides binding, electromagnetism provides identity and distance sensing, and the weak force provides transformation-threshold detection.

Signal emission is placed on a continuous spectrum between fully forced and fully controlled, with structural degradation, the loss of structural components through damage, ageing, or environmental disruption, shown to reduce sensing capability by degrading access to higher-order channels, establishing a quantitative floor of sensing. Evolution itself is reframed as channel expansion under conscious drive, connecting the Hierarchical Channel Accessibility framework directly to Vijay's Law as formally stated in Paper 15. The paper closes by evaluating existing theories of consciousness against the HCA framework: hard emergence theories and standard dualism are shown to be inconsistent with or to have their motivation removed by the HCA results, while Integrated Information Theory, panpsychism, Global Workspace Theory, and embodied cognition are shown to partially converge with, and to be completed by, the same framework [P20].

P20 formalises sensing through Hierarchical Channel Accessibility. Higher-order sensing depends on accessibility to lower-order interaction channels, and the Structural Inclusion Principle is demonstrated across photoreception, mechanoreception, immune recognition, interoception and biomineralisation. Structural degradation reduces access to higher channels, while evolution is treated as expansion of accessible sensing channels under the perpetuation drive.

P20 defines sensing through a capability structure and Hierarchical Channel Accessibility. Higher-order sensing depends on accessibility to lower-order interaction channels, and the Structural Inclusion Principle is demonstrated across photoreception, mechanoreception, immune recognition, interoception and biomineralisation.

18. Paper 21 [P21]: The Consciousness Index

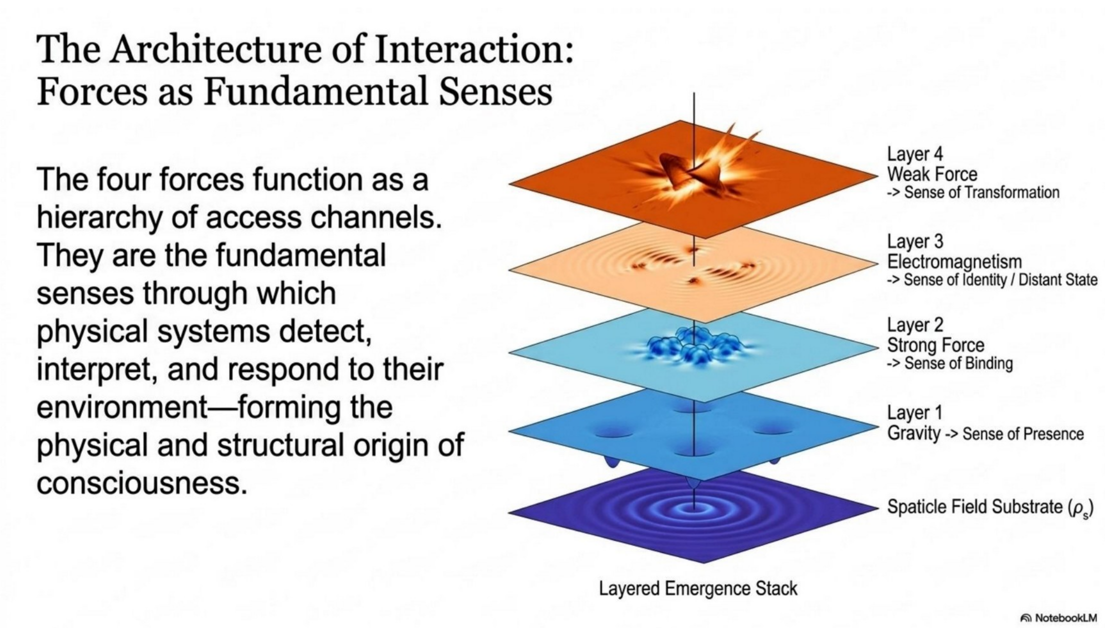

Figure 29. Hierarchical emergence of sensing channels from fundamental interactions leading toward biological consciousness.

Paper 21 develops the Consciousness Index as a physically grounded scalar measure of conscious degree, derived from the channel hierarchy of Paper 20. The intrinsic consciousness index is given by a complete, fully specified formula:

$$CI0 = CI\_floor + C \times Omega(V) \times (1 + 0.38 \times A) \times N^{1.3} \times K^{1.2}$$

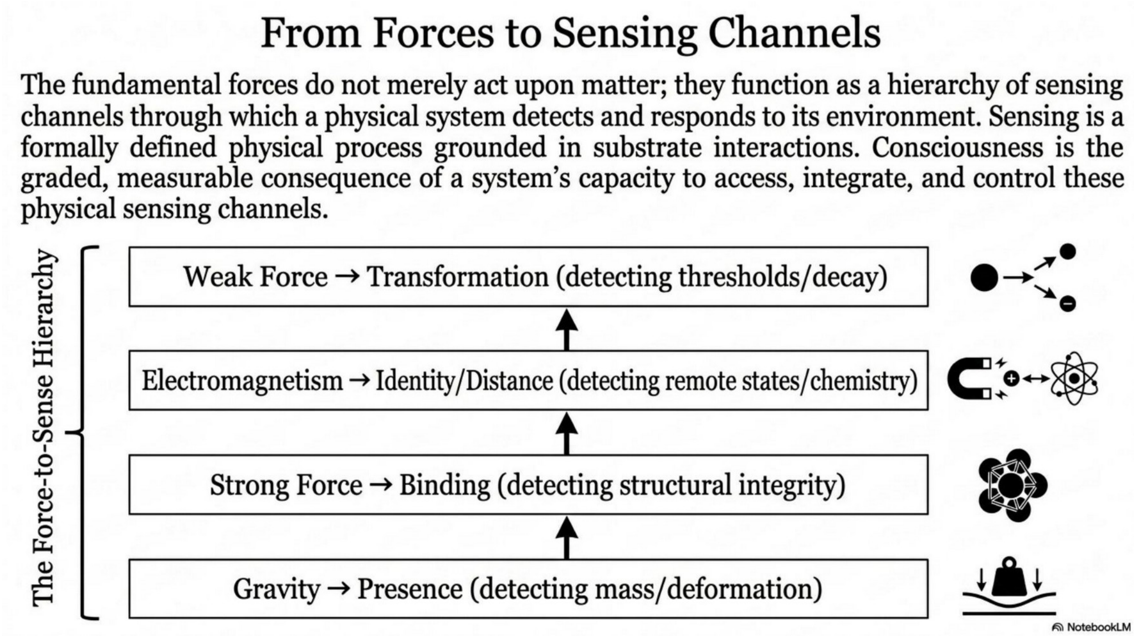

Figure 30. Sequential emergence of the four fundamental forces as progressively richer sensing channels culminating in consciousness.

where CI_floor is a strictly positive constant, grounded in the substrate decoherence floor established in Paper 22, representing the minimum non-zero degree of consciousness of any physical system; Omega(V) is a size factor capturing the non-monotonic relationship between system volume and integration efficiency, since systems that are too large suffer from integration coherence loss; A is channel capacity, the average of five independently scored interaction channels; N is network integration density, a weighted composite of three dimensions; and K is control depth, a weighted composite of three further dimensions. Effective, sustained consciousness separates intrinsic capability from real-world viability:

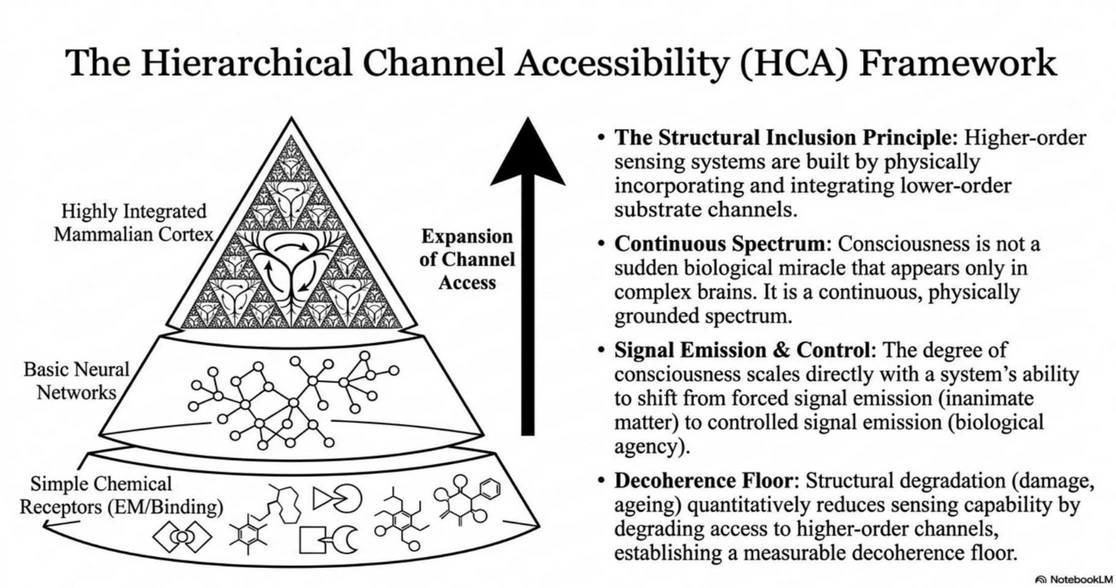

Figure 31. Hierarchical accessibility of sensing channels across physical, biological, and cognitive systems.

$$CI = CI0 \times S$$

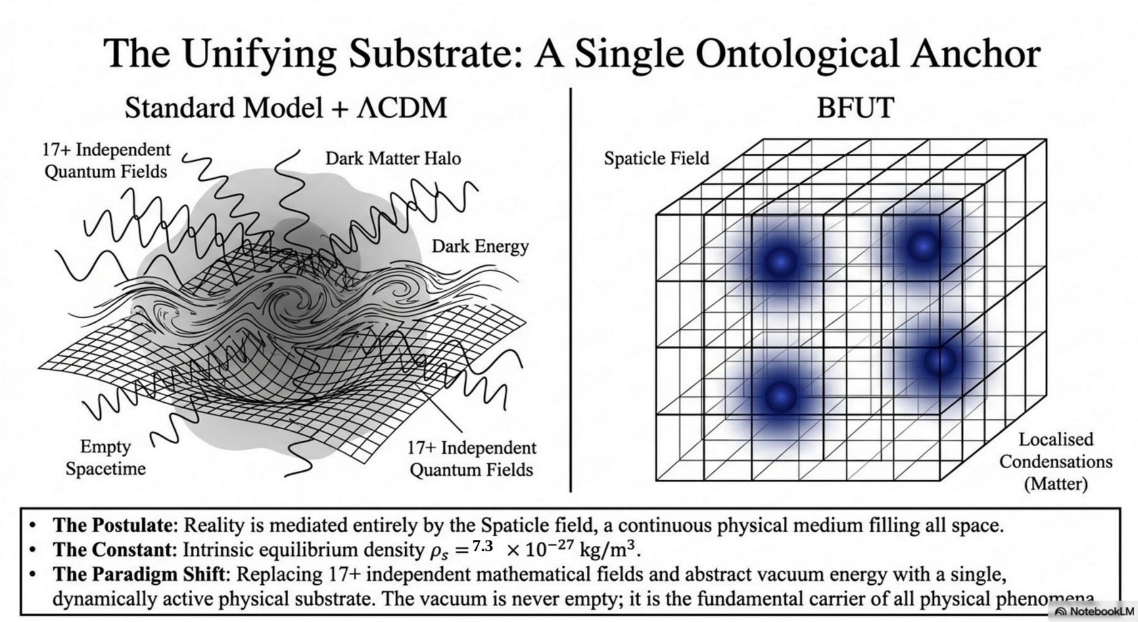

Figure 32. A single physical substrate unifying quantum mechanics, gravity, matter, forces, and consciousness.

where S is a survival factor ranging from 0 to 1.0, the multiplicative bridge between intrinsic capability and effective consciousness. A machine-readable dataset spanning approximately 100 species, including calibration points such as an average human (CI0 = 100 by construction), accompanies the paper. Five falsifiable predictions follow directly from the formula's structure: a size optimum prediction, since Omega(V) is non-monotonic; a reinterpretation of network integration density for non-neural systems; independence of the channel-capacity, integration, and control-depth components from one another; independence of the survival factor from intrinsic capability; and a biological ceiling on achievable CI0 within current biological constraints [P21].

P21 defines CI_0=CI_floor+CΩ(V)(1+0.38A)N^1.3K^1.2 and CI=CI_0S. CI_floor is the positive decoherence floor, Ω(V) is the size factor, A is channel capacity, N is network integration density, K is control depth and S is the survival factor. A machine-readable dataset covering approximately 100 species accompanies the index, together with five falsifiable structural predictions.
P21 separates intrinsic capability from effective sustained consciousness: CI_0=CI_floor+CΩ(V)(1+0.38A)N^1.3K^1.2 and CI=CI_0S. CI_floor is the positive decoherence floor, Ω(V) is the size factor, A is channel capacity, N is network integration density, K is control depth and S is survival or sustained viability.

19. Paper 22 [P22]: Time, Identifying the Cause and Effects

Paper 22 identifies time as the accumulated evolution of substrate states. A clock measures the amount of physical substrate evolution occurring within its own structure; the local rate of that accumulation is set by the local propagation efficiency of the substrate:

eta = d(τ)/dt = c_s/c_0

Identifying time with accumulated substrate evolution produces a direct temporal proof that a true gravitational singularity cannot exist: since gravitational time dilation is itself a substrate effect, an infinite-density point would require time itself to stop accumulating entirely at a single point, which is shown to be incompatible with the substrate's own dynamics. Combining the finite deformation domain of Paper 18 with the finite maximum compression density of Paper 26 produces a result with no analogue in standard general relativity: gravitational time dilation must possess a finite maximum, a directly falsifiable prediction for precision timing experiments near compact objects [P22].

P22 identifies time with accumulated evolution of states in the matter substrate. The local clock-rate relation is η=dτ/dt=c_s/c_0 and the propagation budget is c²=v_spatial²+v_internal²+v_grav². Combining this with finite-domain and finite-density results gives a finite maximum gravitational time-dilation effect.
P22 also gives η(r)=√{1−[2GM/(rc²)]f(r,R_d)} as a weak-field gravitational efficiency relation, connecting local gravitational conditions to the propagation-efficiency variable.

20. Paper 23 [P23]: Light, Photons, and the Universal Speed Limit

Paper 23 expresses the speed of light as the substrate propagation speed, $c = \sqrt{K_s/\rho_s}$, where K_s is the substrate's stiffness; as stated, this relation fixes K_s once c and ρ_s are known. A separate, genuinely independent consistency relation expresses c directly in terms of quantities established elsewhere in the BFUT programme, with no value of c on the right-hand side; this relation and its connection to the P16 ħ and P19 α derivations are given in the cross-check immediately following the Paper 19 section below. A photon has no condensation to maintain, so its entire propagation budget is available for travel; gravitational waves travel at the same speed for the same reason, removing the need for a separate coincidence to explain the equality. Massive particles cannot reach c because part of their propagation budget is permanently committed to maintaining their own condensation; rest mass itself is identified as condensation energy.

Electric fields, magnetic fields, and photons are unified as one substrate phenomenon under different boundary conditions: electric fields are bound radial substrate waves, magnetic fields are bound circulating substrate waves, and photons are the same kind of excitation after detachment from the source, propagating freely. This bound/free distinction produces a specific falsifiable prediction for what happens when an electromagnetic source is switched off, termed the Jacuzzi test: the bound field does not collapse instantaneously everywhere but releases as an outward-propagating substrate disturbance at a finite speed, exactly as a real water jacuzzi continues to show fading circulation after the pump is switched off.

Neutrinos are identified as nearly massless substrate ripples; the speed deficit from c for a neutrino of mass m_nu and energy E is derived quantitatively, and the three neutrino flavours are identified as substrate ripples produced in association with the three charged-lepton generation reactions established in Paper 16. Cosmic redshift is identified as Doppler motion under BFUT gravitational sorting dynamics, removing the need for an expansion parameter.

P23 discusses a finite persistence domain for propagating photons, but the specific numerical threshold a specific numerical E_min threshold is not independently verified in the paper and is not asserted there as an established quantitative prediction.

$$L_{persist} = L_{rlx} \times (E/E_{min})^2 \text{ for } E > E_{min}$$

$$L_{persist} = L_{rlx} \times (E/E_{min})^4 \text{ for } E < E_{min}$$

with $L_{rlx} = c\tau_c$; the local carrier response time τ_c is density-dependent, while the equilibrium natural scale is $L_{nat} \approx 45.17$ AU and $\tau_{nat} \approx 6.26$ h. Above E_min, the photon persists as a self-sustaining soliton; below E_min, no soliton forms, and the substrate disturbance dissolves over a much shorter distance set by the substrate's own vacuum fluctuation energy density. This is checked against six independent observational cases, including the farthest confirmed gamma-ray blazar at redshift 4.72 and GRB 221009A's 18 TeV photon, both consistent with the persistence domain at those energies vastly exceeding the travel distance involved [P23].

The specific piecewise numerical persistence laws involving a specific numerical E_min threshold are not retained here as established P23 results. P23 treats the quantitative threshold as requiring independent verification.

P23 gives $c=\sqrt{K_s/\rho s}$ and $K_s=\rho s c^2$, together with the independent c reconstruction from R_0, e, ε_0, mp, rp and α. It treats photons as freely propagating substrate excitations, unifies electric, magnetic and photon states as different boundary conditions, and proposes the finite-speed "Jacuzzi test".

21. Paper 24 [P24]: Quantum Computing and the Missing Physics Causing Delays and Overspend

Paper 24 applies the substrate framework established in Papers 16 through 19A directly to quantum computing hardware, developing seven novel predictions distinguishing BFUT from the standard treatment of quantum computational phenomena, including substrate-grounded reinterpretations of decoherence, qubit topology, and the photon persistence domain described in Paper 23 as it applies specifically to quantum hardware, drawing directly on the gate-operation formula developed in Paper 27. The full derivations, the complete set of predictions, and the specific experimental proposals developed in this paper contain insights and predictions of direct commercial relevance to the quantum computing industry. The author has elected to pursue patent protection for this material before public disclosure; the detailed content of Paper 24 is therefore withheld pending the publication of that patent application, beyond what is stated in this summary [P24].

P24 applies the substrate framework to quantum-computing hardware, including substrate-grounded decoherence, qubit topology, gate-operation physics, photon persistence and hardware-level constraints. Its detailed quantitative programme is associated with protected technical material.

22. Paper 25 [P25]: Dark Matter

Paper 25 consolidates the dark matter case across the ten cross-sectors on the same equilibrium density ρs = 7.3×10^{-27} kg/m³, with results including particle and electroweak structure, galaxy rotation curves, weak gravitational lensing, hydrogen atomic stability, the matter-stability condition, the substrate vacuum-energy relation, and the H-class mass relation. Galaxy cluster dynamics and related systems provide additional observational consistency checks. The gravitational anomalies the dark matter programme has attempted to explain with an undiscovered particle species are, within this framework, the gravitational signature of the Spaticle field itself, governed by the DDR domain equation of Paper 18. The hydrogen ground-state energy and Bohr radius follow from the substrate-derived ħ and electron mass with no fitted parameter, reproducing the measured values to the accuracy reported in the relevant paper.

The paper validates the framework against every major class of dark matter evidence directly. The Bullet Cluster offset between the visible gas and the gravitational lensing centre is explained because the Spaticle field is non-baryonic and non-electromagnetic in interaction: cluster gas is decelerated by ram pressure during the collision, while the substrate deformation, being purely gravitational in origin, passes through largely undisturbed, separating from the visible gas exactly as observed. The cosmic web's filament-node-void structure, cited as primary evidence for dark matter's gravitational scaffolding role, follows from the same substrate dynamics established in Paper 8. The original 1933 evidence for dark matter itself, Zwicky's measurement of galaxy velocity dispersion in the Coma Cluster far exceeding what visible mass could gravitationally bind, is addressed directly by the same DDR domain equation applied at cluster scale. The CMB temperature, acoustic peak structure, and BAO feature, the Sunyaev-Zel'dovich effect, the integrated Sachs-Wolfe effect, the Lyman-α forest, the S8 tension, and Big Bang nucleosynthesis light-element abundances are each shown to be consistent with the same substrate framework, drawing on the cosmological results of Papers 7 and 10 through 13 [P25]. A code deposit accompanying the paper implements the cross-sector density derivation and the SPARC rotation-curve validation across all 175 galaxies [P25].

P25 also treats cluster-scale observations, low-dark-matter galaxies and the observational classes developed in P7 and P10-P13, connecting them to the same substrate density and acceleration scale.

P25 consolidates the dark-matter interpretation across gravitational and observational sectors while drawing on the same Spaticle ontology used in the particle sector.

23. Paper 26 [P26]: Singularity

Paper 26 derives a finite maximum compression density for any collapsing compact object, replacing general relativity's prediction of infinite density at r equals zero. The restoring pressure from the substrate's quartic stabilisation term, the higher-order repulsion from the sextic term, and the gradient term together balance the inward collapse pressure at relativistic densities:

For a finite-mass object, the causal compactness condition is $R\_max = GM/c^2$, giving the mean-density bound $\bar{\rho}\_max = 3c^6/(4\pi G^3M^2)$. P26 does not supply a separate numerical local maximum density from a restoring-force expression.

a finite value for any non-zero stabilisation coefficient C and substrate density ρ_s. The resulting replacement object is a finite organised compression structure with four physically distinct internal regions, reached through a five-stage collapse evolution sequence from an ordinary star to a stable compact structure, determined entirely by the same condensation functional. A rotational sustenance principle is derived, giving a quantitative seed dissipation timescale governing which of three formation pathways, large-scale rotational aggregation, stellar collapse, or explosive release, leads to a self-sustaining structure. Quantitative evidence from galaxy enhancement fractions, the ratio of the substrate's rotational contribution to the observed rotation velocity, supports rotational entrainment saturation directly from the validated DDR results of Paper 18. The paper closes with a scientific assessment of nine popular claims about singularities, including that the Big Bang itself was a singularity and that singularities permanently destroy information, finding each inconsistent with a finite, organised compression structure [13].

P26 derives finite compact-object compression from gradient, quartic stabilisation and sextic repulsion. It gives the finite-density model relation and the causal bounds $R\_max=GM/c^2$ and $\bar{\rho}\_max=3c^6/(4\pi G^3M^2)$. The paper develops a four-region compact object and a five-stage collapse sequence, together with rotational sustenance and seed-dissipation behaviour.

P26 combines gradient, quartic stabilisation and sextic repulsion in the finite-compression treatment. Its causal compactness results are $R\_max=GM/c^2$ and $\bar{\rho}\_max=3c^6/(4\pi G^3M^2)$. The paper also derives rotational sustenance and seed-dissipation behaviour.

24. Paper 27 [P27]: The Planck Constant

Paper 27 isolates and develops the ħ derivation introduced in Paper 16 into its own first-principles treatment, reproducing the reduced Planck constant from condensation geometry alone:

$$\hbar = m_p \cdot c \cdot r_p / (\pi \times R_0)$$

to within 0.00048% of the measured value, with no fitted constant. The physical reading is that the quantum of action is the action associated with one complete circulation of a substrate condensation at the proton's own condensation scale. Substituting this derived ħ directly into every standard formula that contains it produces an explicit substrate form for each quantity: the Compton wavelength hierarchy, the de Broglie wavelength, the quantum harmonic oscillator energy levels, the quantum tunnelling decay constant, and the unitary time-evolution operator $U(t) = \exp(-iHt/\hbar)$ governing quantum gate operations, providing the direct mathematical link to the quantum computing predictions of Paper 24. Angular momentum quantisation is derived as a winding-number condition on substrate circulation, and the spin-statistics theorem is recovered from the same substrate topology, connecting the half-integer spin result of Paper 19A to a single underlying mechanism. The paper closes with a diagnosis of the standard QFT vacuum energy discrepancy and its relation to the ΛCDM cosmological constant, reshaping the interpretation of ħ from a free constant of nature into a derived geometric quantity that fixes the scale of quantum mechanics throughout the rest of the programme [P27].

P27 develops $\hbar = m_p c\ r_p/(\pi R_0)$ as a first-principles geometric result and carries it through the Compton wavelength, de Broglie wavelength, harmonic oscillator, tunnelling and unitary quantum-evolution formulas. It also develops angular-momentum quantisation and spin-statistics from substrate topology and provides the R_0 cross-check.

25. Paper 28 [P28]: Black Holes Demystified

Paper 28 identifies what are conventionally called black holes as vortical compact objects within the Spaticle substrate, governed by a Universal Centrality Rule: the vortical compression core of every settled-state host system is located at the exact dynamical centre of that system, confirmed across galaxies from dwarf irregulars to giant ellipticals at every redshift where spatial resolution is sufficient, with apparent exceptions arising only from wandering cores in unsettled post-merger systems. The rotational hierarchy established across this and the cosmic-rotation results of Paper 9 is connected directly to the observed M-σ relation between central compact object mass and host galaxy velocity dispersion. Building on the finite-core result of Paper 26, the compact object has a four-region internal architecture and a coherence boundary that is explicitly distinguished from a true event horizon.

A five-premise analysis is presented arguing that Hawking radiation, as conventionally derived, does not exist: each of the five foundational premises of the 1974-1975 Hawking derivation, including the existence of a medium-free geometric vacuum, a true Killing event horizon, and a genuine singularity, is shown to describe a configuration inconsistent with the finite, substrate-occupied structure established across Papers 18 and 26. What replaces the Hawking mechanism is carrier relaxation; the Bekenstein-Hawking entropy relation $S = A/4$ is reinterpreted without requiring either an event horizon or a singularity, as a measure of substrate deformation complexity, the number of distinguishable organised deformation states at a given energy. The paper closes with a scientific assessment of nine further popular claims about black holes, including that they are featureless objects characterised only by mass, spin, and charge, and that primordial black holes formed during the Big Bang, finding each inconsistent with the finite-core, centrally-located, rotationally-sustained structure established across this paper and its companions [P28].

P28 develops the gravitational-vortex model and Universal Centrality Rule, specifies a four-region internal structure and distinguishes the coherence boundary from a true event horizon. It analyses the premises of the conventional Hawking-radiation mechanism, replaces thermal pair production with carrier relaxation, and interprets black-hole entropy as substrate deformation complexity.

P28 connects finite-core compact objects with the Universal Centrality Rule and the host-galaxy M−σ relation. Its four-region structure distinguishes the coherence boundary from an event horizon, and its treatment of Hawking radiation replaces thermal pair production with finite carrier relaxation.

26. Paper 29 [P29]: The Three Fermion Generations (Restricted, ongoing work)

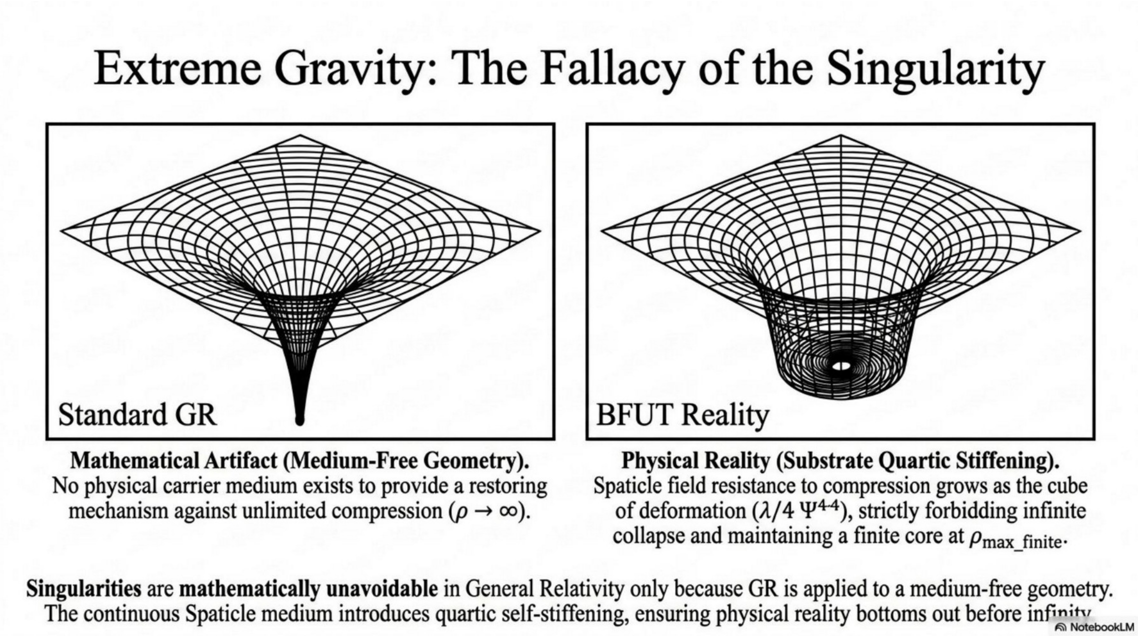

Figure 33. BFUT explanation of gravitational collapse showing why physical singularities cannot form.

Paper 29 is a restricted publication containing ongoing work on the proposed origin of the three fermion generations within the 3+e condensation established in Paper 16. The work has progressed beyond the results described here. The publicly presented BFUT framework identifies the three-generation structure with excitation sectors of the 3+e condensation and establishes a geometric connection with the charged-lepton Koide relation. Subsequent mathematical analysis has further resolved the exact symmetry constraints and identified the remaining dynamical conditions required to derive the complete fermion mass hierarchy. These additional results are presently restricted and will be made available when the corresponding work is unrestricted. Layer 1 therefore records P29 as an active area of BFUT development and does not present the restricted results as part of the public synthesis.

$$M = m_p/3;\ n = 4;\ n^2 = 16;\ m\_W\_vss = (n^2)^2 M = 256M = (256/3)m_p.$$

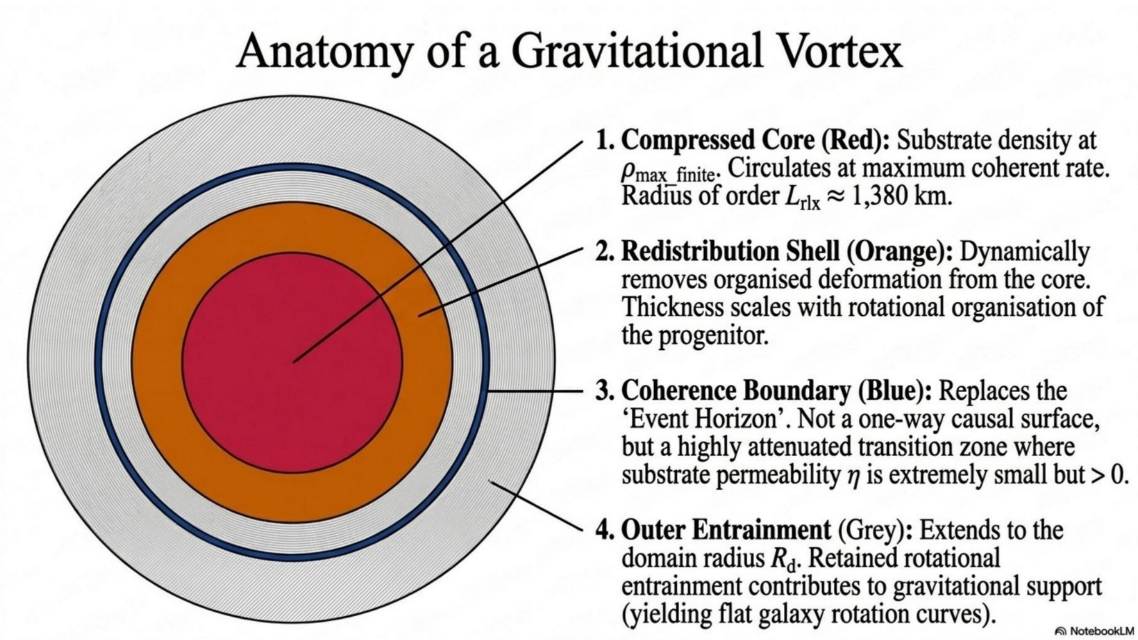

Figure 34. Internal structure and dynamics of a BFUT gravitational vortex replacing the conventional black hole model.

where $256 = (n^2)^2 = 16^2$, from the $n = 4$ threshold identified in Paper 16. This specific relation, and the geometric symmetry argument recovering the Koide relation, are established results; deriving the full fermion

mass hierarchy from the same geometric origin is the subject of continuing work [P29].
P29 is a restricted publication on the proposed origin of the three fermion generations as resonance sectors of the 3+e condensation. This synthesis records the public scope of the work without reproducing its restricted mathematical results. The public description identifies exact symmetry constraints, Koide geometry and the dynamical problem of deriving the full fermion mass hierarchy.

27. Master Symbol and Formula List

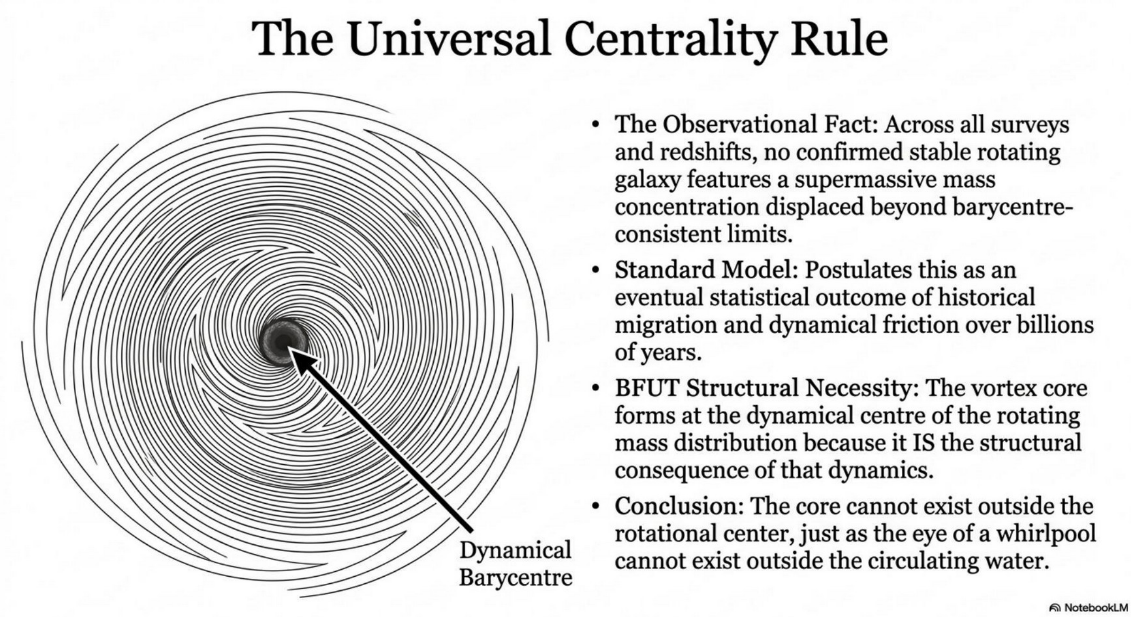

Figure 35. The Universal Centrality Rule showing why every observer naturally appears near the centre of their observable universe.

The following table collects the principal symbols and formulas introduced across Papers 16 through 29, organised by paper and topic. This is a subset of the full master symbol guide maintained alongside the BFUT programme; the complete reference, including the cosmological symbols of Papers 1 through 13, is available as a separate companion document.

Shared Physical Constants

Symbol	Definition	Value
ρ_s	Spaticle field equilibrium density	7.3×10^{-27} kg/m³
G	Gravitational constant	6.674×10^{-11} m³ kg⁻¹ s⁻²
c	Speed of light / substrate propagation speed	2.99792458×10^{8} m/s
ħ	Reduced Planck constant	= mp × c × rp/(π × R_0); 0.00048% agreement
m_p	Proton mass	938.272 MeV/c²
m_e	Electron mass	= $m_p/(6 \times \pi^5)$; 0.002% agreement
r_p	Proton charge radius	0.8414 fm

Paper 16 [P16]: Condensation Functional

Symbol	Definition	Value / Formula
E(n)	Total condensation energy for n units	Full four-term functional
R_0	Dimensionless condensation minimum	= 1.27349
E_unit	Fundamental energy unit	= $m_p \times c^2/\pi$ = 298.661 MeV
V_{gap}/V_q	Interstitial volume fraction	= 0.0770
F_conf	Derived confinement force	0.574 GeV/fm (64% of

		measured)

Paper 18 [P18]: Gravitational Domain Structure (DDR)

Symbol	Definition	Value / Formula
R_d	Intrinsic deformation-domain radius	$= (3M/8\pi\rho_s)$^(1/3)
R_eff	Effective domain radius with rotation	$= R_d \times (1 + v_{rot}^2/c^2)$^(1/3)
F1-cov	Fully covariant carrier field equation	Master equation; GR recovered in settled limit
DeltaSigma(r)	Excess surface density (lensing)	KiDS-1000 validated

Papers 17 and 19: Coupling Constants and Masses

Symbol	Definition	Value / Formula
α	Fine structure constant	1/137.036; BFUT 1/137.1 (0.05%)
α_s	Strong coupling constant	0.118; BFUT 0.120 (1.8%)
$\sin^2\theta$_W_vss	BFUT electroweak mixing quantity	$1 - (\text{m\_W\_vss}/\text{m\_Z\_vss})^2 = 0.23257$
m_W_vss, m_Z_vss	Independent W and Z resonance masses	80.066 GeV/c^2; 91.396 GeV/c^2
m_H_vss	H-class radial resonance mass	λ_H_vss = 2 A R_0 / π^2; v_vss = 6E_unit/α_vss; m_H_vss = v_vss√(2λ_H_vss) = 124.75 GeV/c^2
λ_SI	Universal SI quartic self-coupling	$= \rho_s/4 = 1.8257354 \times 10^{-27}$ kg/m³
R_0 (cross-check)	R_0 from α and measured constants	$= 4 \times \varepsilon_0 \times mp \times c^2 \times rp \times \alpha/e^2 = 1.27348831$; agrees with condensation R_0 = 1.27348 to 0.00048%
c (consistency relation)	Speed of light, independent of K_s/ρ_s	$c^2 = e^2R_0/(4\varepsilon_0 mprp\alpha)$; c_vss = 2.99791740×10^8 m/s

Paper 19A [P19A]: Named Resonances

Resonance	Formula	Mass (GeV)
Shankar	m_Shankar c^2 = [E(2+2) − E(3+1)]E_unit = 2.60E_unit	0.7765
BFUT	m_BFUT c^2 = [E(4+0) − E(3+1)]E_unit = 4.70E_unit	1.4037

Paper 22 [P22]: Time and Propagation Budget

Symbol	Definition	Value / Formula
eta	Propagation efficiency	η = dτ/dt = c_s/c_0
v_spatial, v_internal	Propagation budget components	v_spatial² + v_internal² = c²
d(τ)/dt	Proper time rate	= eta; what clocks measure

Paper 23 [P23]: Photon Propagation

Symbol	Definition	Value / Formula
K_s	Substrate stiffness	$6.56355667 \times 10^{-10}$ Pa (= J/m³)
E_min	Minimum coherent photon energy	= 2.25 meV
L_persist	Photon soliton persistence length	L_persist = L_rlx × (E_photon/E_min)² for E > E_min
u_vac	Substrate vacuum energy density	u_vac = $\rho_s c^2 = 6.56355667 \times 10^{-10}$ J/m³

Paper 24 [P24]: Quantum Computing

Symbol	Definition	Value / Formula
U(t)	Quantum gate unitary evolution operator	$= \exp(-iHt/\hbar)$
CHSH	Bell inequality parameter	

Paper 26 [P26]: Anti-Singularity

Symbol	Definition	Value / Formula
P_restore	Substrate restoring pressure	Derived restoring-pressure term from the P26 stabilisation sector; see P26 constitutive equation.
ρ_max	Maximum finite collapse density	finite by substrate physics
J_entrain	Outward entrainment flux during collapse	proportional to gradient(rho - ρ_s)

Paper 27 [P27]: Planck Constant Consequences

Symbol	Definition	Value / Formula
λ_C	Reduced Compton wavelength (BFUT form)	$= \hbar/(m \times c)$; universal, with BFUT ħ agreement 0.00048%
λ_dB	de Broglie wavelength (BFUT form)	$= mp \times c \times rp/(\pi \times R_0 \times p)$
E_n (harmonic oscillator)	Energy levels	$= (n+1/2) \times \hbar \times \omega$
l_P, m_P, t_P	Planck length, mass, time (BFUT form)	each 0.0003% agreement (inherits ħ^(1/2) scaling)

Paper 21 [P21]: Consciousness Index

Symbol	Definition	Value / Formula
CI0	Intrinsic Consciousness Index	= CI_floor + C × Omega(V) × (1+0.38A) × $N^{1.3} \times K^{1.2}$
CI	Effective Consciousness Index	= CI0 × S
A, N, K	Channel capacity, integration, control depth	each independently measurable
S	Survival factor	0 to 1.0

28. Simulation Codes, Datasets, and Deposits

The companion papers summarised throughout this paper are accompanied by code and data deposits, each independently archived on Zenodo with its own DOI, listed in the Code and Data Deposits section of the References. These include the proof-of-concept simulation suite [CD1], the CMB dynamic thermal equilibrium simulation [CD2], the CMB acoustic peak and BAO reinterpretation code [CD3], the cosmic rotation simulation [CD4], the Sunyaev-Zel'dovich substrate interaction code [CD5], the Lyman-α forest absorption percolation simulation [CD6], the Integrated Sachs-Wolfe effect simulation [CD7], the weak gravitational lensing and S8 tension code [CD8], the full numerical implementation of the Paper 16 condensation functional [CD9], the Paper 17-18-19 master validation suite [CD10], the DDR field equation numerical simulations [CD12], the KiDS-1000 weak gravitational lensing validation pipeline [CD13], the companion visualisation suite spanning the substrate physics from particle to cosmological scale [CD14], the machine-readable Consciousness Index dataset [CD15], the published biological data underlying the Consciousness Index [CD16], and the executable verification codebase for the full derivation chain from the condensation functional to the particle, gravitational and observational results [CD21].

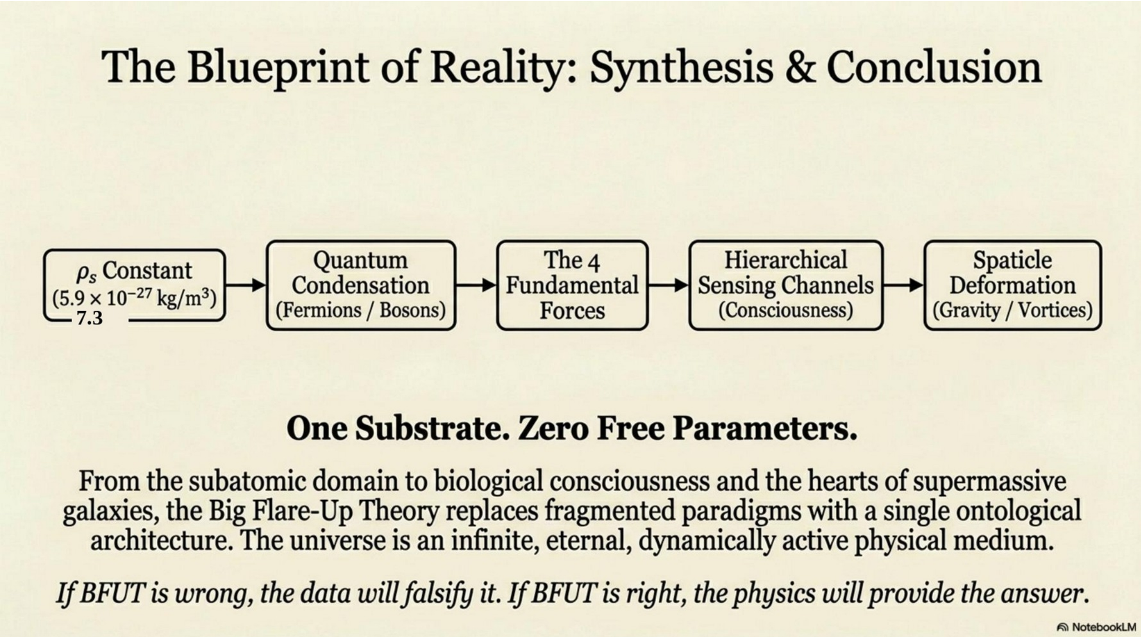

Figure 36. Blueprint of Reality: the complete BFUT framework showing the emergence of matter, forces, life, consciousness, and cosmology from the unified Spaticle substrate.

29. Conclusion

Layer 1 is the architectural statement of the BFUT programme. The companion papers supply the detailed derivations, numerical implementations, observational analyses and specialised physical arguments. The synthesis connects them into one mathematical and physical chain so that the reader can follow the framework from its condensation origin through its particle, quantum, gravitational and cosmological consequences.

The observational programme carries the same derived quantities into galaxy rotation, weak lensing and cosmological observables. The consolidated prediction programme in Appendix B and the consolidated ΛCDM tension-resolution programme in Appendix C provide the cross-domain map of these consequences.

The matter-formation mechanism includes a quantitative stability filter. The 3+e configuration dominates the reported parameter-space scans, while unstable configurations supply the proposed antimatter rebound pathway. Particle-sector relations extend from the proton-electron hierarchy and proton radius to the H-class radial resonance and the configuration resonance masses. Extreme compression is treated through finite substrate dynamics and a finite causal mean-density bound.

The carrier formulation connects microscopic condensation to gravitational response. F1-cov supplies the common field description, while the finite deformation-domain relation and DME equation provide the gravitational and galactic regimes. The strong, electromagnetic and weak interactions are developed as successive organisational regimes of the same condensed substrate. The quantum programme carries the carrier description into the Schrödinger, Born-rule, spin, exclusion, collapse, superposition and entanglement results. Light and gravitational waves share the same substrate propagation limit, while the time formulation assigns relativistic clock-rate changes to the allocation of propagation capacity.

The mathematical chain begins with the condensation functional and its physically derived coefficients. Its stable dimensionless minimum R_0 provides the geometric reference from which the particle and substrate relations are developed. The independent reconstruction of R_0 provides a cross-check from the particle-sector constants. The same chain produces the equilibrium substrate density $\rho s = 7.3 \times 10^{-27}$ kg/m³ and connects it to the reduced Planck constant, fine-structure relation, propagation speed, substrate stiffness, carrier scale and universal acceleration scale.

The Big Flare-Up Theory presents one connected physical architecture in which the matter substrate, which the Big Flare-Up Theory calls the Spaticle Field, supplies the common physical basis for matter, interactions, gravitation, quantum phenomena, light, time and the large-scale structure of the universe.

30. References

External Literature

[1] Abbott, B. P., et al. (LIGO Scientific Collaboration and Virgo Collaboration). (2016). Observation of gravitational waves from a binary black hole merger. Physical Review Letters, 116(6), 061102.

[2] Ashtekar, A., & Singh, P. (2011). Loop quantum cosmology: A status report. Classical and Quantum Gravity, 28(21), 213001.

[3] ATLAS Collaboration. (2012). Observation of a new boson at a mass of 125 GeV with the ATLAS detector at the LHC. Physics Letters B, 716(1), 1-29.

[4] Bethe, H. A. (1939). Energy production in stars. Physical Review, 55(5), 434-456.

[5] Benisty, D., et al. (2026). Hubble-constant and mass determination of Centaurus A and M83 from tip-of-red-giant-branch distances. Astronomy & Astrophysics, 705, A283. https://doi.org/10.1051/0004-6361/202556283

[6] Bojowald, M. (2001). Absence of a singularity in loop quantum cosmology. Physical Review Letters, 86(23), 5227-5230.

[7] Boylan-Kolchin, M. (2023). Stress testing ΛCDM with high-redshift galaxy candidates. Nature Astronomy, 7, 731-735.

[8] Colin, J., Mohayaee, R., Rameez, M., & Sarkar, S. (2019). Evidence for anisotropy of cosmic acceleration. Astronomy & Astrophysics, 631, L13. https://doi.org/10.1051/0004-6361/201936373

[9] CMS Collaboration. (2012). Observation of a new boson at a mass of 125 GeV with the CMS experiment at the LHC. Physics Letters B, 716(1), 30-61.

[10] Curtis-Lake, E., et al. (2023). Spectroscopic confirmation of four metal-poor galaxies at z = 10.3-13.2. Nature Astronomy, 7(5), 622-632. https://doi.org/10.1038/s41550-023-01918-w

[11] Davis, T. M., & Lineweaver, C. H. (2004). Expanding confusion: Common misconceptions of cosmological horizons and the superluminal expansion of the universe. Publications of the Astronomical Society of Australia, 21(1), 97-109.

[12] Einstein, A. (1916). Die Grundlage der allgemeinen Relativitätstheorie. Annalen der Physik, 49(7), 769-822.

[13] Einstein, A. (1917). Kosmologische Betrachtungen zur allgemeinen Relativitätstheorie. Sitzungsberichte der Königlich Preussischen Akademie der Wissenschaften, 142-152.

[14] Fields, B. D. (2011). The primordial lithium problem. Annual Review of Nuclear and Particle Science, 61, 47-68.

[15] Gamow, G. (1928). Zur Quantentheorie des Atomkernes. Zeitschrift für Physik, 51(3-4), 204-212.

[16] Gamow, G. (1970). My world line: An informal autobiography. Viking Press.

[17] Guth, A. H. (1981). Inflationary universe: A possible solution to the horizon and flatness problems. Physical Review D, 23(2), 347-356.

[18] Hawking, S. W. (1992). Chronology protection conjecture. Physical Review D, 46(2), 603-611.

[19] Hawking, S. W., & Ellis, G. F. R. (1973). The large scale structure of space-time. Cambridge University Press.

[20] Hoyle, F., Bondi, H., & Gold, T. (1948). A new model for the expanding universe. Monthly Notices of the Royal Astronomical Society, 108(5), 372-382.

[21] Hubble, E. (1929). A relation between distance and radial velocity among extra-galactic nebulae. Proceedings of the National Academy of Sciences, 15(3), 168-173.

[22] Kerr, R. P. (1963). Gravitational field of a spinning mass as an example of algebraically special metrics. Physical Review Letters, 11(5), 237-238.

[23] Labbé, I., et al. (2023). A population of red candidate massive galaxies ~600 Myr after the Big Bang. Nature, 616, 266-269.

[24] Milgrom, M. (1983). A modification of the Newtonian dynamics as a possible alternative to the hidden mass hypothesis. Astrophysical Journal, 270, 365-370.

[25] Perlmutter, S., et al. (1999). Measurements of Ω and Λ from 42 high-redshift supernovae. Astrophysical Journal, 517(2), 565-586.

[26] Planck Collaboration. (2020). Planck 2018 results. VI. Cosmological parameters. Astronomy & Astrophysics, 641, A6. https://doi.org/10.1051/0004-6361/201833910

[27] Popper, K. R. (1959). The logic of scientific discovery. Hutchinson.

[28] Riess, A. G., et al. (1998). Observational evidence from supernovae for an accelerating universe and a cosmological constant. Astronomical Journal, 116(3), 1009-1038.

[29] Riess, A. G., et al. (2019). Large Magellanic Cloud Cepheid standards provide a 1% foundation for the

determination of the Hubble constant. Astrophysical Journal, 876(1), 85.
[30] Rovelli, C. (2004). Quantum gravity. Cambridge University Press.
[31] Rubin, V. C. (1980). Dark matter in spiral galaxies. Scientific American, 248(6), 96-108.
[32] Steinhardt, P. J., et al. (2016). Planck 2015 results challenge the simplest inflationary models. Physical Review Letters, 117(26), 261302.
[33] Verde, L., Treu, T., & Riess, A. G. (2019). Tensions between the early and late universe. Nature Astronomy, 3, 891-895.
[34] Wagner, J., Benisty, D., & Karachentsev, I. D. (2026). The binary ballet: Mapping local expansion around M 81 and M 82. Astronomy & Astrophysics, 706, A92. https://doi.org/10.1051/0004-6361/202557876
[35] Workman, R. L., et al. (Particle Data Group). (2022). Review of Particle Physics. Progress of Theoretical and Experimental Physics, 2022(8), 083C01. https://doi.org/10.1093/ptep/ptac097
[36] Zwicky, F. (1937). On the masses of nebulae and of clusters of nebulae. Astrophysical Journal, 86, 217-246.

[37] Lelli, F., McGaugh, S. S., & Schombert, J. M. (2016). SPARC: Mass Models for 175 Disk Galaxies with Spitzer Photometry and Accurate Rotation Curves. Astronomical Journal, 152, 157.
BFUT Companion Papers
[P1] Sharma, V. S. (2026). Gravitational Sorting as an Alternative Mechanism for the Hubble Relationship. Zenodo. DOI: 10.5281/zenodo.19226423
[P2] Sharma, V. S. (2026). Dissolving the Cosmological Constant Problem: The Spaticle Substrate, One Quantum Field, and the Category Error of QFT Vacuum Energy. Zenodo. DOI: 10.5281/zenodo.19242083
[P3] Sharma, V. S. (2026). A Steady-State Nucleosynthesis Resolution of the Cosmological Lithium Problem. Zenodo. DOI: 10.5281/zenodo.19205920
[P4] Sharma, V. S. (2026). Observer Bulk Flow as an Alternative Explanation for Apparent Cosmic Acceleration. Zenodo. DOI: 10.5281/zenodo.19228065
[P5] Sharma, V. S. (2026). The Universe Has No Boundary: Logical, Derivational, and Observational Arguments for Spatial Infinitude. Zenodo. DOI: 10.5281/zenodo.19242759
[P6] Sharma, V. S. (2026). Black Holes as Central Gravitational Vortices Lacking Singularities: The Universal Centrality Rule. Zenodo. DOI: 10.5281/zenodo.19300874
[P7] Sharma, V. S. (2026). Dynamic Thermal Equilibrium as an Alternative Origin for the CMB Temperature. Zenodo. DOI: 10.5281/zenodo.19302025
[P7A] Sharma, V. S. (2026). A Living-Universe Reinterpretation of the CMB Acoustic Peak Pattern and BAO Scale. Zenodo. DOI: 10.5281/zenodo.19303398
[P8] Sharma, V. S. (2026). Cold, Dark, and Inevitable: A Logical Reconstruction of the Universe Before the Big Flare-Up. Zenodo. DOI: 10.5281/zenodo.19323579
[P9] Sharma, V. S. (2026). Cosmic Rotation Across Scales, Emergent Orbital Hierarchy, and the Large-Scale Challenge to Metric Expansion. Zenodo. DOI: 10.5281/zenodo.19341549
[P10] Sharma, V. S. (2026). The Sunyaev-Zel'dovich Effect as Local Substrate Interaction: A Big Flare-Up Theory Reinterpretation. Zenodo. DOI: 10.5281/zenodo.19377396
[P11] Sharma, V. S. (2026). The Lyman-Alpha Forest in the Big Flare-Up Theory: Absorption Percolation Threshold and Interpretive Non-Uniqueness of the Gunn-Peterson Opacity Rise. Zenodo. DOI: 10.5281/zenodo.19383804
[P12] Sharma, V. S. (2026). The Integrated Sachs-Wolfe Effect in BFUT: Local Spaticle Field Temperature Variations as an Alternative to Decaying Gravitational Potentials in an Accelerating Universe. Zenodo. DOI: 10.5281/zenodo.19391470
[P13] Sharma, V. S. (2026). Weak Gravitational Lensing and the S8 Tension in BFUT: Why Late-Time Clustering Inference Is Not a Unique Test of Lambda-CDM. Zenodo. DOI: 10.5281/zenodo.19392597
[P14] Sharma, V. S. (2026). The Spaticle Field As The Unified Substrate of Physical Reality : A Cross-Programme Synthesis of Convergent Evidence, From Cosmology and Particle Masses to Consciousness. Zenodo. DOI: 10.5281/zenodo.19394064
[P15] Sharma, V. S. (2026). What Existed Before Matter and the Spaticle Field: The Origin of Space, Time, and the Physical Substrate of Reality in an Infinite Universe. Zenodo. DOI: 10.5281/zenodo.19811691
[P16] Sharma, V. S. (2026). The Origin of Matter, Antimatter, and Fundamental Forces: How Protons, Electrons, and Hydrogen Formed. Zenodo. DOI: 10.5281/zenodo.19908216
[P16A] Sharma, V. S. (2026). Antimatter, Annihilation, and the Stability Filter: Predictions for the CERN Antihydrogen Programme. Zenodo. DOI: 10.5281/zenodo.20201014
[P17] Sharma, V. S. (2026). The Emergence of Forces and Fundamental Senses: How the Spaticle Field Gave

Rise to Gravity and All Other Forces. Zenodo. DOI: 10.5281/zenodo.19976408
[P18] Sharma, V. S. (2026). Beyond General Relativity: A Unified Gravitation Equation Across Quantum, Classical, Galactic, and Rapid-Transition Regimes. Zenodo. DOI: 10.5281/zenodo.20145506
[P19] Sharma, V. S. (2026). Unification of Particle Physics: Deriving Fine Structure and Coupling Constants, W, Z, and Higgs Boson Masses, Redefining and Unifying Gravity and Time. Zenodo. DOI: 10.5281/zenodo.20145567
[P19A] Sharma, V. S. (2026). Unifying Quantum Mechanics with Gravity, Demystifying Twenty Quantum Phenomena Including Half-Integer Spin, the Born Rule, Wave Function Collapse, and Higgs Physics. Zenodo. DOI: 10.5281/zenodo.20145695
[P20] Sharma, V. S. (2026). From Matter and Fundamental Forces to Consciousness: A Unified Framework of Sensing Channels, Control, and Evolution. Zenodo. DOI: 10.5281/zenodo.19992457
[P21] Sharma, V. S. (2026). The Consciousness Index (CI): A Physically Grounded Scalar Measure of Conscious Degree, Structure, and Evolutionary Potential. Zenodo. DOI: 10.5281/zenodo.20025739
[P22] Sharma, V. S. (2026). Time: Identifying the Cause and Effects and Unifying General and Special Relativity. Zenodo. DOI: 10.5281/zenodo.20556908
[P23] Sharma, V. S. (2026). Light, Photons, and the Universal Speed Limit: A First-Principles Derivation of c from Substrate Condensation Dynamics. Zenodo. DOI: 10.5281/zenodo.20577935
[P24] Sharma, V. S. (2026). Quantum Computing and the Missing Physics Causing Delays and Overspend: Real Unknown Constraints, Critical Predictions, and a Blueprint for Progress. Zenodo. DOI: 10.5281/zenodo.20620192
[P25] Sharma, V. S. (2026). Dark Matter: Connecting Galaxy Clusters, Galaxy Rotations, W and Z Boson Masses, and Atomic Structure Through One Physical Constant. Zenodo. DOI: 10.5281/zenodo.20535295
[P26] Sharma, V. S. (2026). Singularity: Why and How Physical Substrate Dynamics Make Infinite Density Impossible. Zenodo. DOI: 10.5281/zenodo.20557070
[P27] Sharma, V. S. (2026). The Planck Constant: A First-Principles Derivation of ħ and How It Reshapes the Interpretation of Quantum Mechanics. Zenodo. DOI: 10.5281/zenodo.20620283
[P28] Sharma, V. S. (2026). Black Holes Demystified: What They Actually Are, the Universal Centrality Rule, Why Singularities Cannot Form, and Why Hawking Radiation Doesn't Exist. Zenodo. DOI: 10.5281/zenodo.20740461

Code and Data Deposits
[P29] Sharma, V. S. (2026). The Three Fermion Generations as Resonances of the 3+e Condensation: Exact Koide Geometry, Symmetry Constraints and the Remaining Dynamical Problem. BFUT P29. 11 September 2026.
[CD1] Sharma, V. S. (2026). BFUT Simulation Suite: Proof-of-Concept Interactive Simulations. Zenodo. DOI: 10.5281/zenodo.19124509
[CD2] Sharma, V. S. (2026). CMB Dynamic Thermal Equilibrium: Simulation Code. Zenodo. DOI: 10.5281/zenodo.19299978
[CD3] Sharma, V. S. (2026). CMB Acoustic Peak and BAO Reinterpretation: Simulation Code. Zenodo. DOI: 10.5281/zenodo.19124364
[CD4] Sharma, V. S. (2026). Cosmic Rotation Across Scales: Simulation Code. Zenodo. DOI: 10.5281/zenodo.19329540
[CD5] Sharma, V. S. (2026). Sunyaev-Zel'dovich Effect Substrate Interaction: Simulation Code. Zenodo. DOI: 10.5281/zenodo.19376665
[CD6] Sharma, V. S. (2026). Lyman-Alpha Forest Absorption Percolation: Simulation Code. Zenodo. DOI: 10.5281/zenodo.19378026
[CD7] Sharma, V. S. (2026). Integrated Sachs-Wolfe Effect in BFUT: Simulation Code. Zenodo. DOI: 10.5281/zenodo.19391144
[CD8] Sharma, V. S. (2026). Weak Gravitational Lensing and S8 Tension: Simulation Code. Zenodo. DOI: 10.5281/zenodo.19391808
[CD9] Sharma, V. S. (2026). BFUT Full Functional Code Deposit. Zenodo. DOI: 10.5281/zenodo.20517866
[CD10] Sharma, V. S. (2026). BFUT P17-18-19 Master Validation Suite. Zenodo. DOI: 10.5281/zenodo.20156714
[CD12] Sharma, V. S. (2026). BFUT Numerical Simulations: DDR Field Equations etc. Zenodo. DOI: 10.5281/zenodo.20208030
[CD13] Sharma, V. S. (2026). BFUT Weak Gravitational Lensing Validation: KIDS-1000. Zenodo. DOI:

10.5281/zenodo.20155983
[CD14] Sharma, V. S. (2026). Companion Simulations: Substrate Physics Visualised. Zenodo. DOI: 10.5281/zenodo.20554084
[CD15] Sharma, V. S. (2026). Consciousness Index Dataset: Machine-Readable 100-Species. Zenodo. DOI: 10.5281/zenodo.20025538
[CD16] Sharma, V. S. (2026). P21: Published Biological Data Underlying the Consciousness Index. Zenodo. DOI: 10.5281/zenodo.20720053
[CD21] Sharma, V. S. (2026). Python Calculation and Validation Codebase: An Executable Verification Framework for the Big Flare-Up Theory (V1). Zenodo. DOI: 10.5281/zenodo.22864191

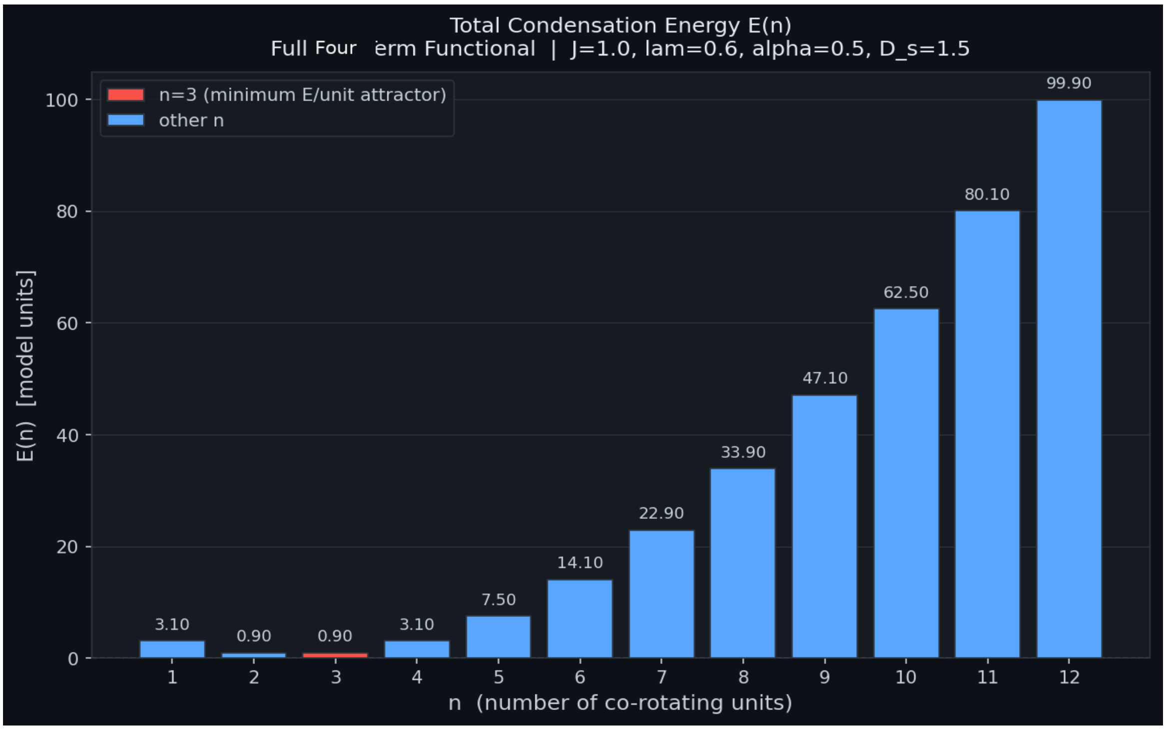

Figure 37. Total condensation energy E(n) for n=1 to 12. n=3 highlighted.

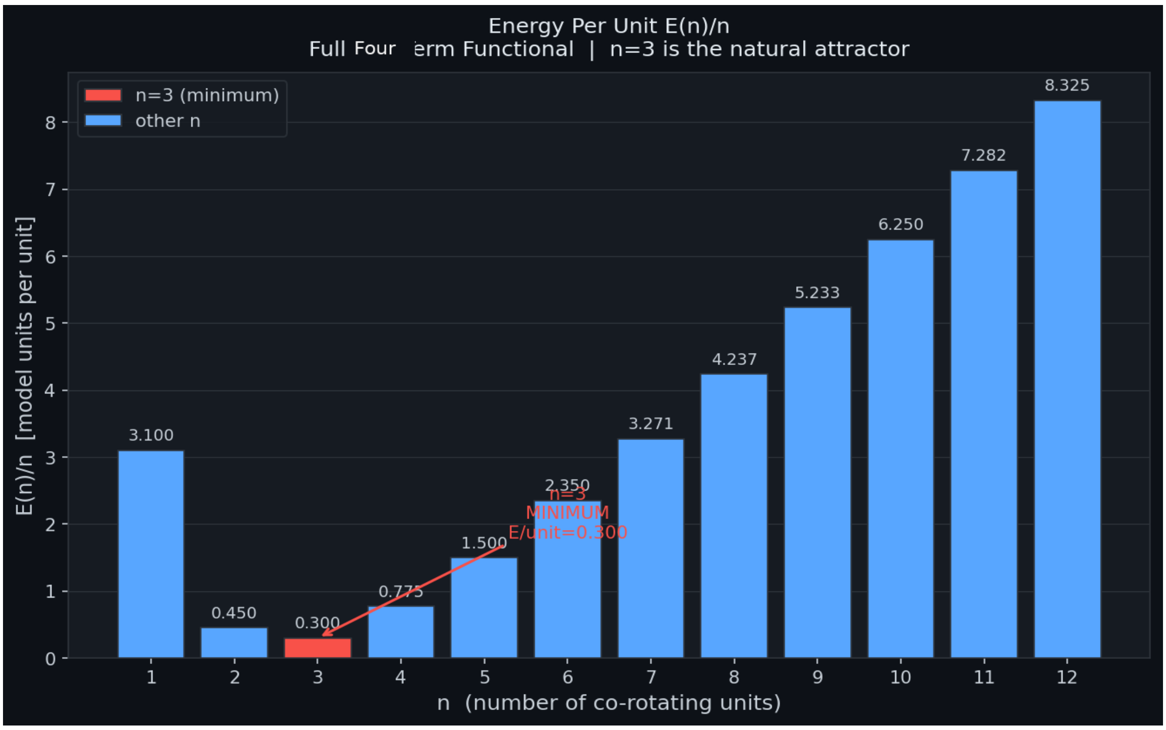

Figure 38. Energy per unit E(n)/n for n=1 to 12. n=3 is the unambiguous minimum.

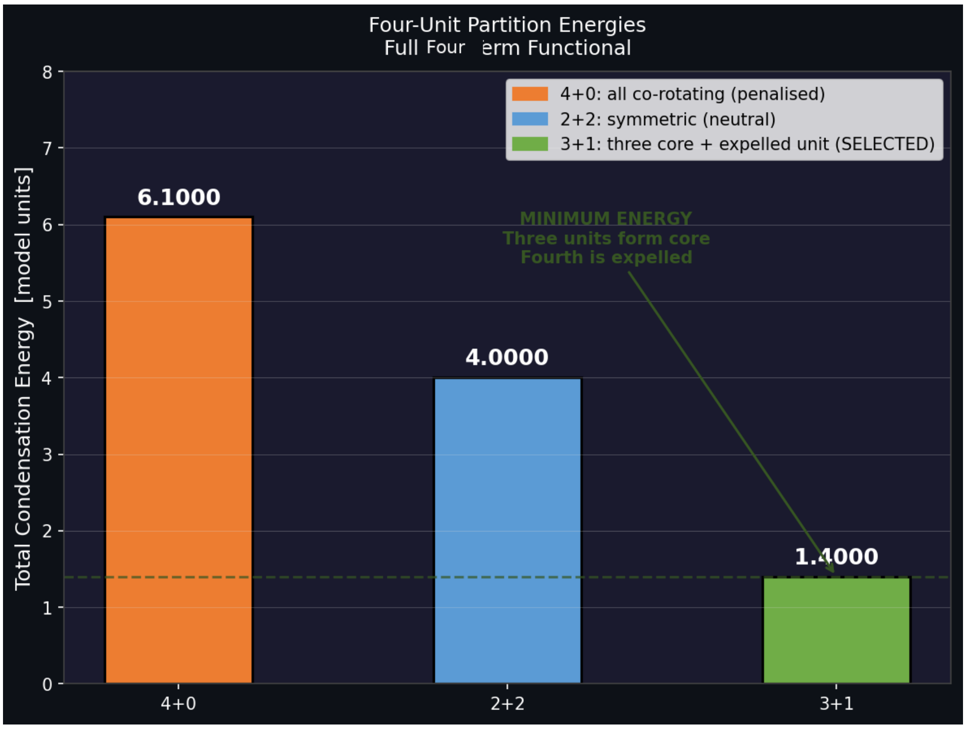

Figure 39. Four-unit partition energies. 3+1 is the clear minimum.

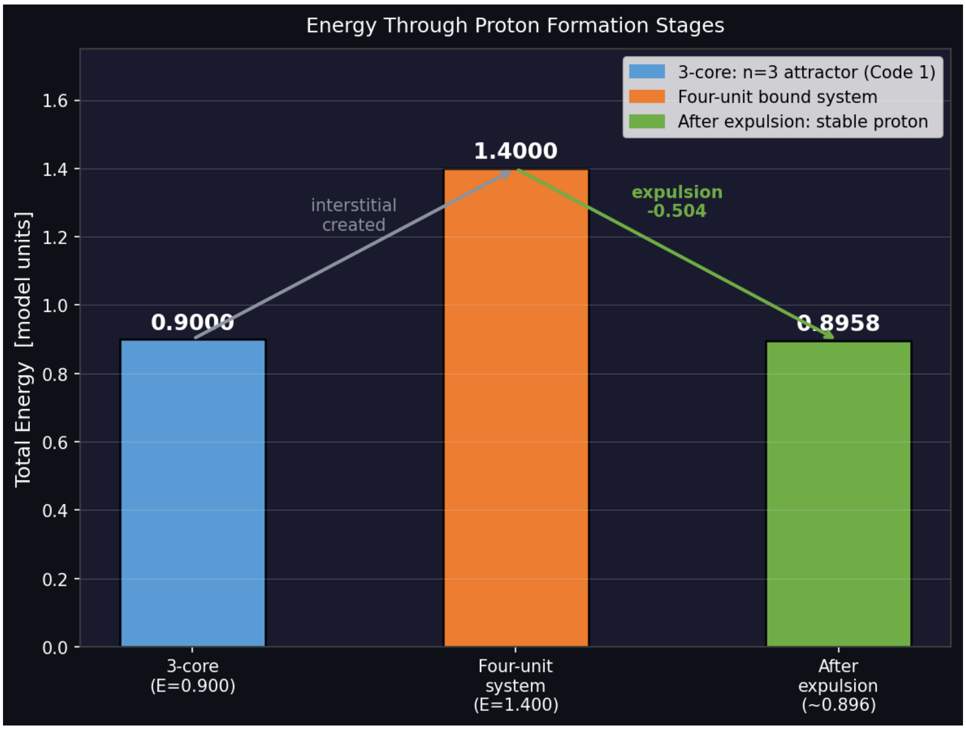

Figure 40. Energy through the three stages of proton formation.

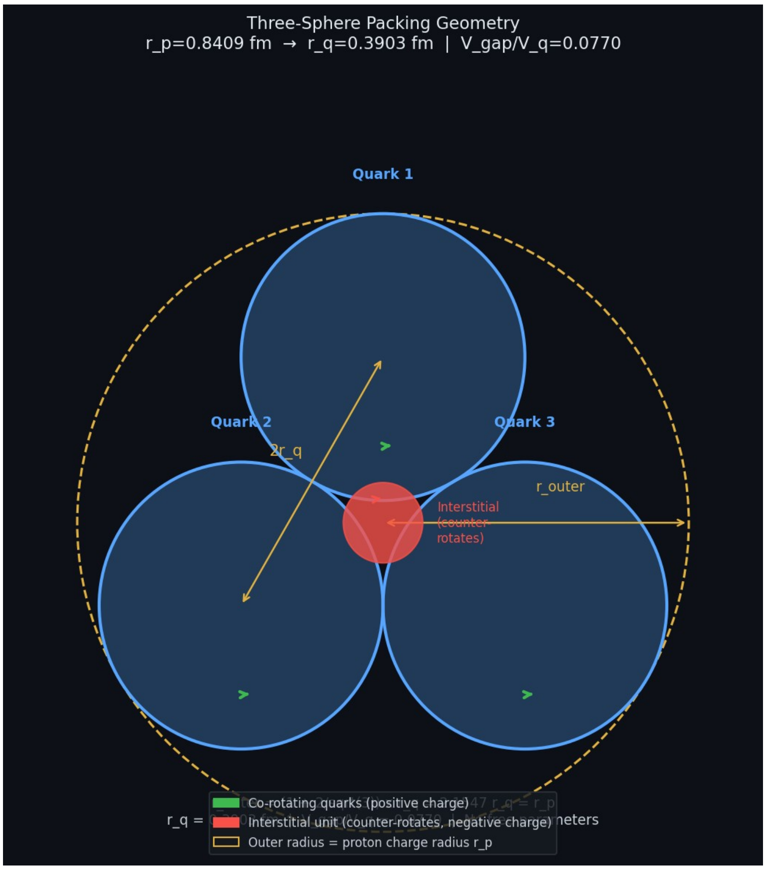

Figure 41. Three-sphere packing geometry. Green arrows: co-rotating quarks. Red: interstitial unit (counter-rotates). Yellow dashed: outer radius = rp.

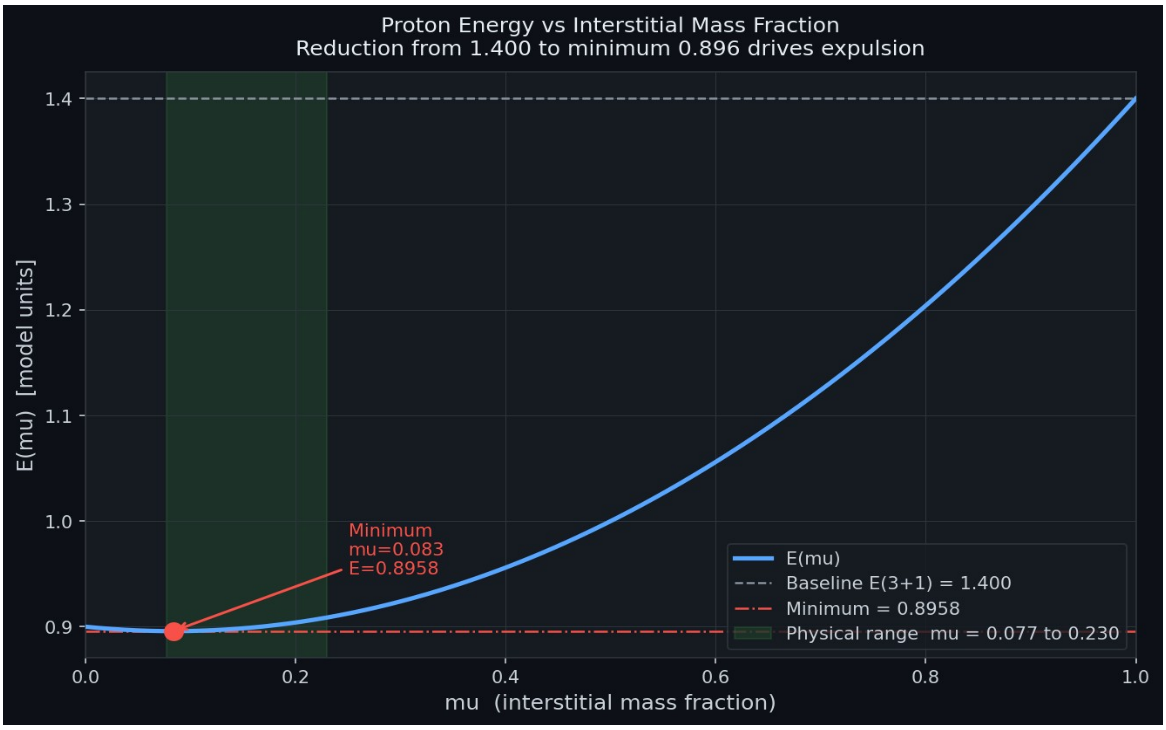

Figure 42. E(mu) vs mu across the full range 0 to 1. Minimum at mu=0.083. Green band: physical range.

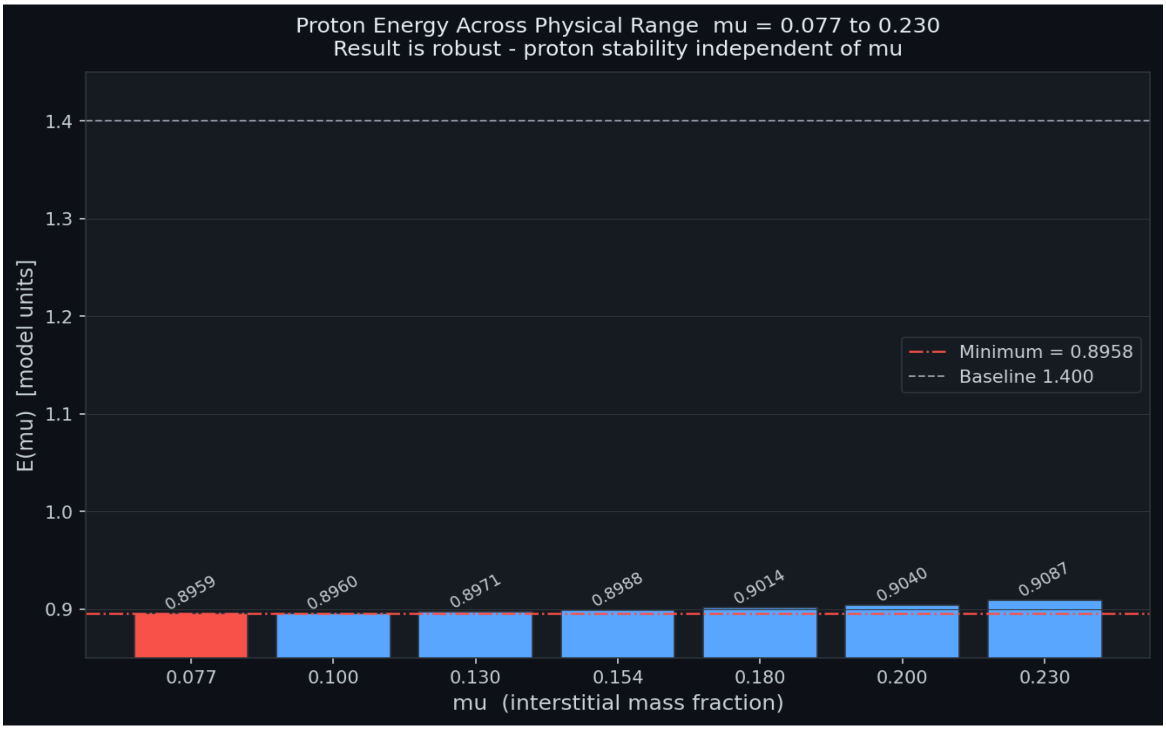

Figure 43. Proton energy across the physical range mu=0.077 to 0.230. Result is robust.

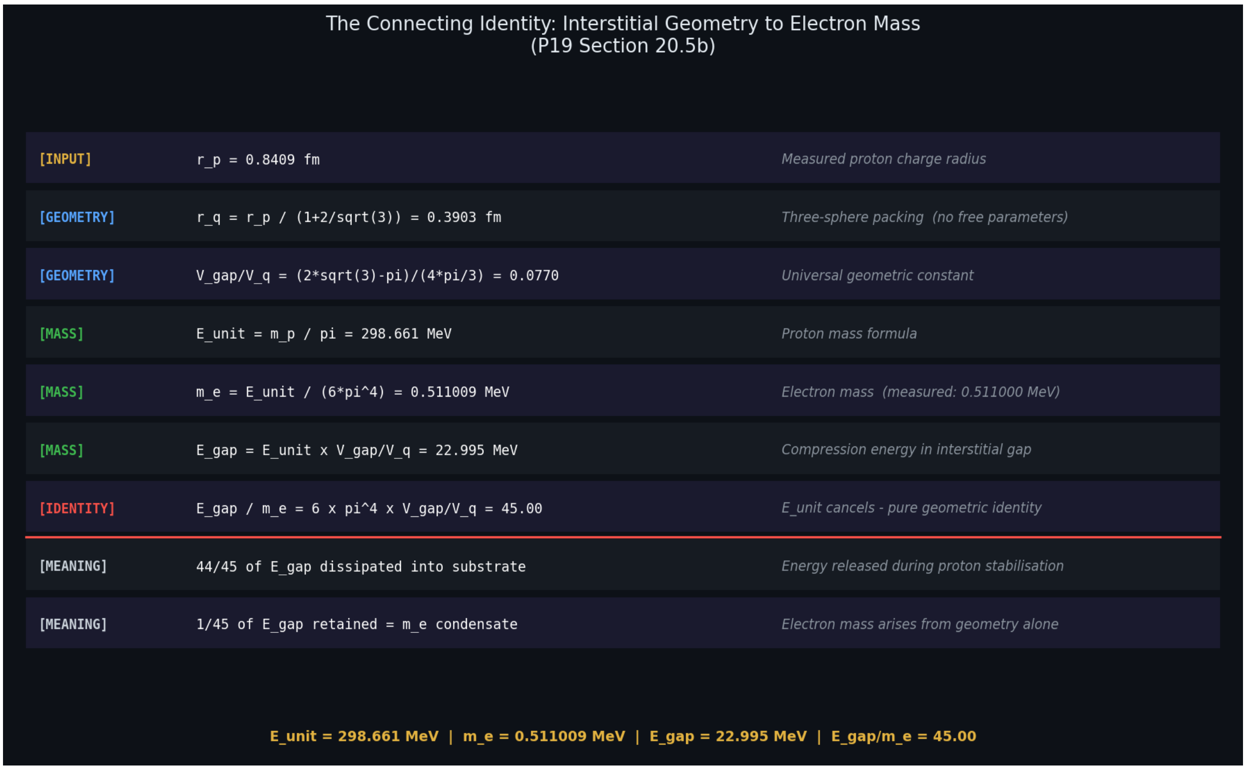

Figure 44. The connecting identity chain from measured rp to m_e. E_unit cancels at the IDENTITY step.

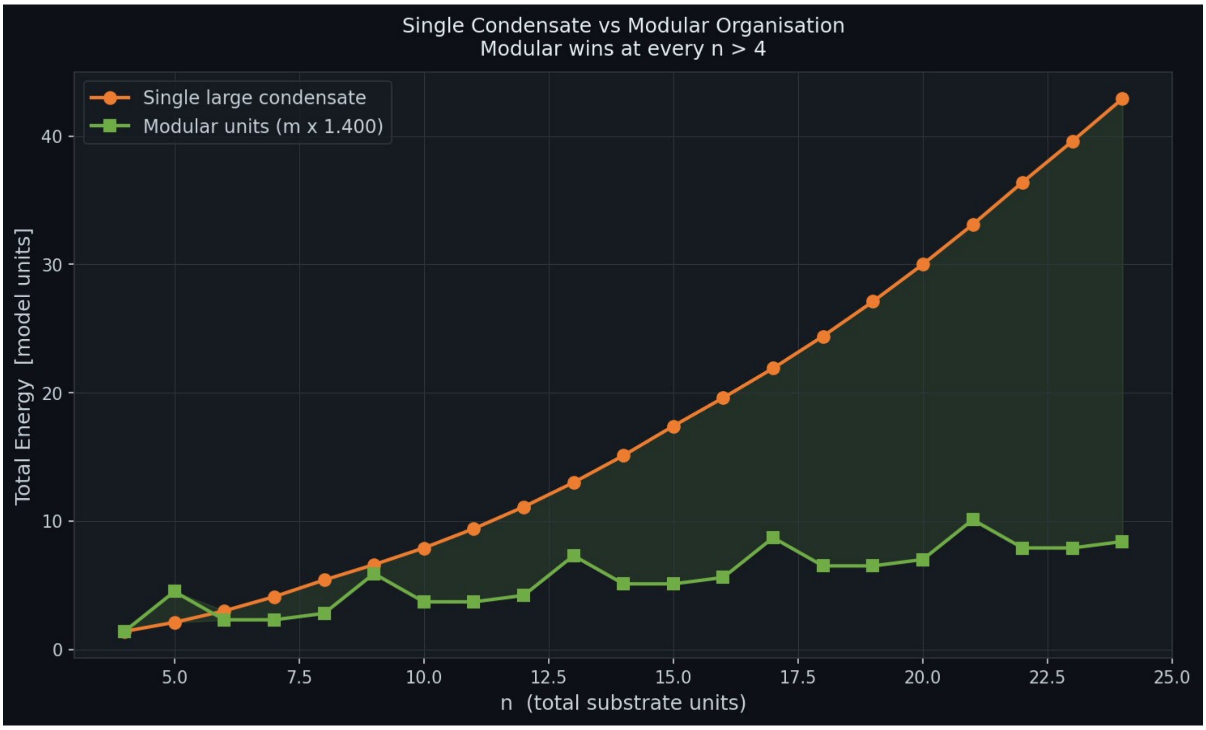

Figure 45. Total energy: single condensate vs modular units for n=4 to 24.

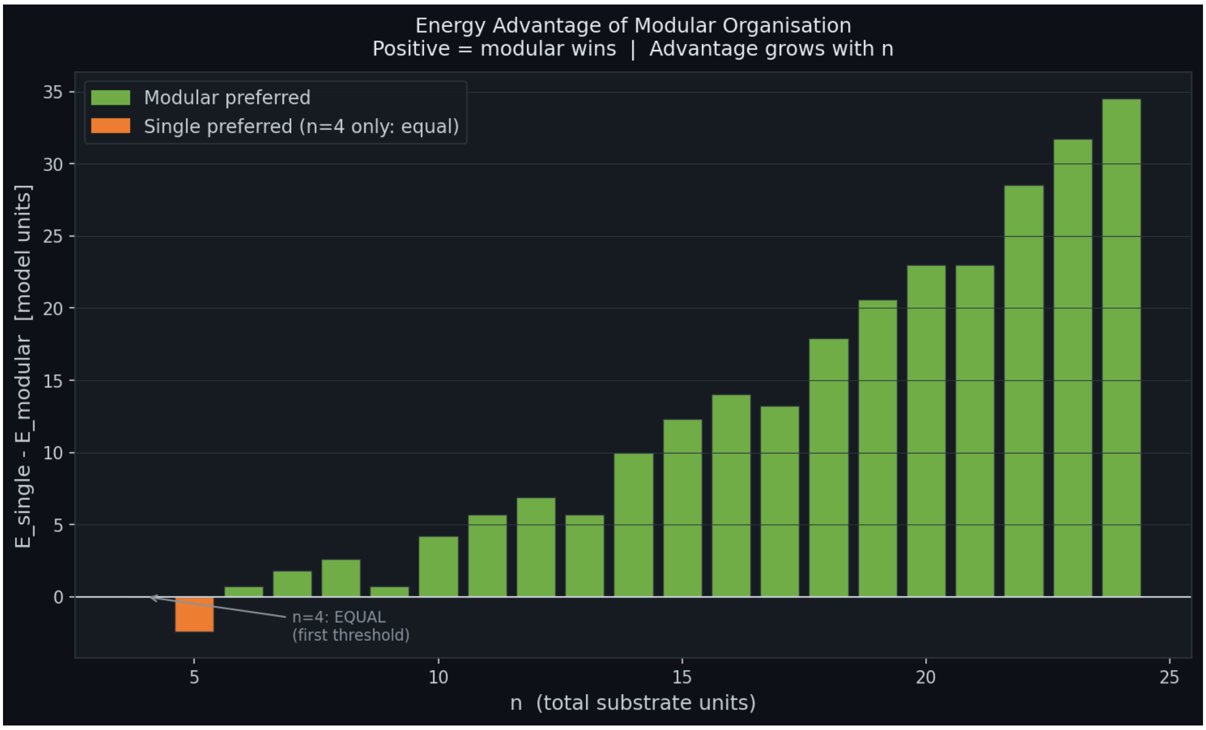

Figure 46. Energy advantage of modular organisation. Positive = modular wins. Gap grows with n.

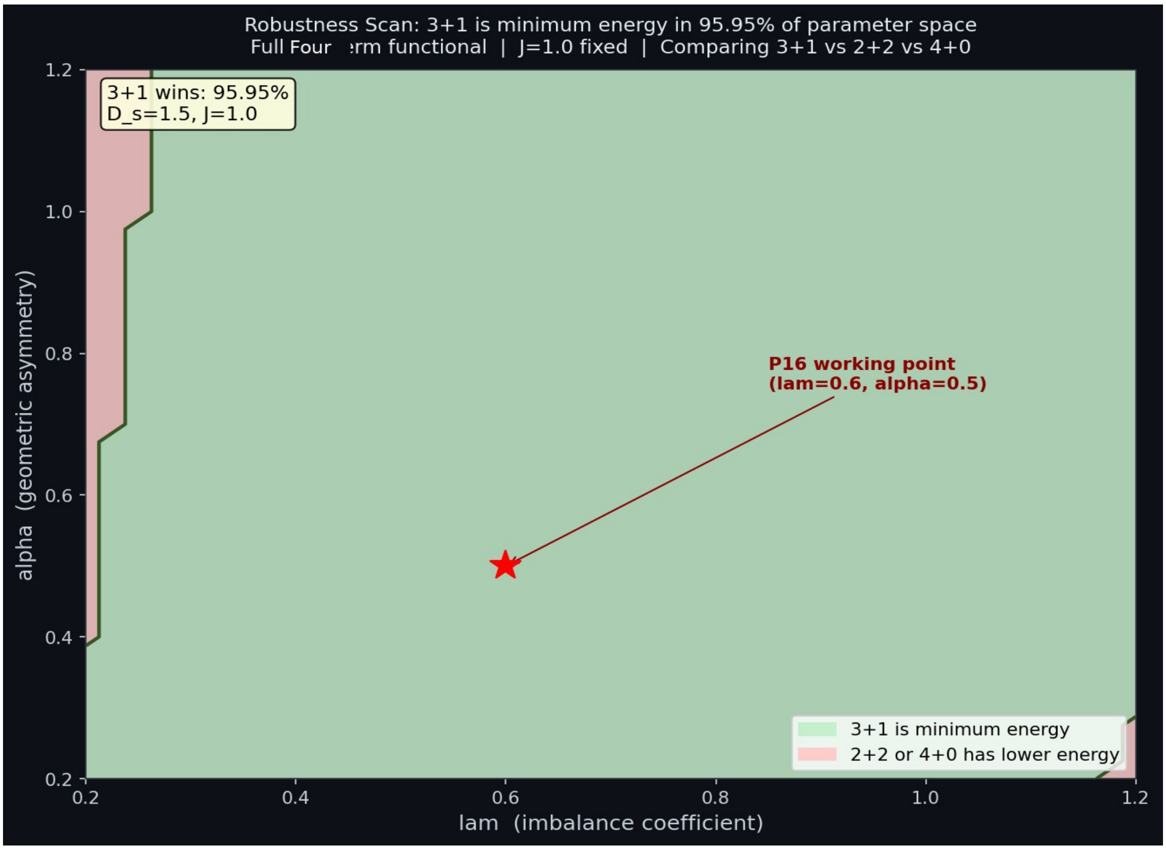

Figure 47. Parameter space map. Green: 3+1 is minimum energy. Red: other configuration wins. P16 working point marked.

This appendix lists independently meaningful physical applications, derived results, predictions, and observational applications that have a direct derivational or physical chain to the Spaticle Field or its derived density. Intermediate mathematical calculations are not listed as separate applications.

Appendix A. Applications and Derived Results of the Matter Substrate

This appendix lists independently meaningful physical applications, derived results, predictions, and observational applications that have a direct derivational or physical chain to the Spaticle Field or its derived density. Intermediate mathematical calculations are not listed as separate applications.

SN	Application / Derived Result	Physical result or BFUT application	BFUT source
1	Spaticle-field equilibrium density	Intrinsic substrate density $\rho_s = 7.3 \times 10^{-27}$ kg/m³, obtained from the condensation framework and used as the common physical substrate parameter.	P16; P25; P78
2	Matter creation from the Spaticle Field	Matter condenses from the physical Spaticle Field and remains embedded in it. This provides the substrate basis for the particle and matter structures developed throughout BFUT.	P14; P16; P17
3	Propagation of forces and physical disturbances through the Spaticle Field	Forces and physical disturbances propagate through the Spaticle Field. This supplies the common physical carrier underlying the electromagnetic, gravitational, weak, and strong interaction descriptions.	P14; P17; P18; P23
4	Stable condensation equilibrium	The condensation functional produces a finite non-zero equilibrium condensation scale R_0 for stable matter structures.	P16
5	Proton condensation structure	The three-core condensation architecture produces the structural basis for proton formation.	P16
6	3+e proton structure	The stable 3+e organisation supplies the particle architecture used in the proton and electron formation chain.	P16; P17
7	Electron mass	The BFUT particle chain derives electron mass from the proton-scale condensation construction.	P16; P19
8	Matter-antimatter structure and annihilation	Matter and antimatter are treated as corresponding substrate condensation configurations, with annihilation arising from cancellation of opposing organised excitations and release of condensation energy.	P16; P16A
9	Antihydrogen structure and CERN comparison	The BFUT antimatter construction gives a mirror configuration for antihydrogen and provides a framework for comparison with CERN antihydrogen measurements.	P16A
10	Stability filter for matter and antimatter	The stability filter identifies which condensation configurations can persist as stable matter or antimatter structures.	P16; P16A
11	Emergence of the fundamental forces	Gravity, strong, electromagnetic, and weak interactions are derived as distinct physical disturbance or organisation channels associated with the substrate and 3+e matter structure.	P17
12	Gravity as substrate deformation and restoring response	Gravitational attraction is described as the restoring response of the Spaticle Field to matter-induced deformation.	P17; P18
13	Covariant carrier-field equation	F1-cov provides the covariant substrate equation governing gravitational deformation and propagation.	P18
14	Density-derived carrier scale	The substrate density fixes the carrier scale μ_s and its associated propagation/screening scales.	P18
15	Finite gravitational deformation domain	For source mass M, BFUT gives a finite deformation-domain radius $R_d = [3M/(8\pi\rho_s)]^{(1/3)}$.	P18; P22; P26
16	Rotationally enlarged deformation domain	The effective deformation domain incorporates the rotational correction defined by the BFUT carrier model.	P18
17	Carrier relaxation length and timescale	The carrier framework supplies finite response and relaxation scales for substrate deformation.	P18; P26
18	Cosmological screening length	The density-derived carrier mass establishes a finite cosmological screening scale for the static carrier field.	P18
19	BFUT gravitational acceleration scale	The characteristic acceleration a_s is derived from the substrate density, G, and c.	P18; P78
20	Finite-domain gravity across physical regimes	The finite deformation-domain carrier is formulated for quantum, classical, galactic, and rapid-transition regimes, providing a common and testable gravitational description across those scales.	P18
21	Dark Matter Effects interpretation	The gravitational effect conventionally attributed to dark matter is represented in BFUT by organised or entrained Spaticle-field structure.	P18; P25; P78
22	Dark Matter Effects equation	The DME relation derives the additional rotational contribution from the baryonic distribution and the substrate-derived acceleration scale without modifying Newtonian gravity.	P18; P25; P78
23	SPARC rotation-curve validation	DME is applied to the 175-galaxy SPARC sample using the same substrate-derived acceleration scale and published baryonic inputs.	P25; P78
24	KiDS-1000 weak-lensing validation	DME is applied to the KiDS-1000 stacked weak-lensing mass bins using the same substrate-derived acceleration scale.	P25; P78
25	Additional galaxy-system tests	DME is tested against additional named systems, including low-dark-matter and ultra-diffuse systems in the observational programme.	P25; P78
26	Merger morphology and substrate entrainment	Merger systems are interpreted through the redistribution and entrainment of substrate-associated mass during interaction.	P78
27	Low-rotation systems	Systems with negligible organised rotation provide a regime in which the substrate contribution predicted by the rotational DME mechanism	P25; P78

SN	Application / Derived Result	Physical result or BFUT application	BFUT source
		is correspondingly reduced.	
28	Sunyaev-Zel'dovich effect	P10 gives a Spaticle-field interpretation of the SZ effect through interaction of propagating substrate modes with the thermal electron population.	P10; P25
29	Lyman-alpha forest	P11 interprets the Lyman-alpha absorption forest through the interaction of propagating structures with the substrate and the absorption-percolation threshold.	P11; P25
30	Integrated Sachs-Wolfe effect	P12 attributes the ISW temperature contribution to variations in Spaticle-field density encountered by photons along their path.	P12; P25
31	Weak-lensing S8 application	P13 connects the weak-lensing S8 result and suppressed late-time structure growth to the physical substrate and its domain dynamics.	P13; P25
32	CMB acoustic peaks	The BFUT cosmological substrate framework models acoustic structure through ongoing shell processes in the physical substrate and reproduces CMB-like peak structure in the reported proof-of-principle treatment.	P12; P25
33	BAO-like feature	The same cosmological substrate treatment produces a BAO-like feature in the reported proof-of-principle simulation.	P12; P25
34	Fine-structure constant	The fine-structure constant α_vss is derived from the BFUT condensation and electromagnetic circulation structure.	P19; P27
35	Strong coupling constant	The strong coupling α_s_vss is derived from the P16 condensation parameters and evaluated at the Z-boson mass scale.	P19
36	Weak mixing angle	The BFUT electroweak mixing quantity is read from the independently derived resonance masses: $\sin^2\theta$_W_vss = 1 − (m_W_vss/m_Z_vss)² = 0.23257.	P19
37	W-boson mass	The charged W resonance is the n=4 coherent reconfiguration: m_W_vss = 256M = (256/3)m_p = 80.066 GeV/c². No mixing angle enters this mass relation.	P19; P25
38	Z-boson mass	The neutral Z core-stay resonance follows from the proton-scale condensation chain: m_Z_vss = $\pi^4 m_p$ = 91.396 GeV/c². No mixing angle enters this mass relation.	P19; P25
39	H-class radial resonance mass	The radial H resonance follows from λ_H_vss = $2AR_0/\pi^2$ and v_vss = 6E_unit/α_vss: m_H_vss = v_vss√(2λ_H_vss) = 124.75 GeV/c².	P19
40	H-class state as a radial resonance	The observed H-class state is a radial resonance of the one Spaticle field; BFUT introduces no separate Higgs field.	P19A
41	Shankar and BFUT configuration resonances	The 2+2 and 4+0 excitation gaps give m_Shankar c² = 776.5 MeV and m_BFUT c² = 1403.7 MeV. P16A contains the full derivation and experimental resonance correspondence.	P16A
42	Quark-mass hierarchy	The particle programme derives the quark-mass hierarchy from the condensation and circulation architecture.	P19; P19A
43	Hydrogen Bohr radius	BFUT-derived particle and action quantities are used in the atomic relation for the hydrogen ground-state radius.	P16; P25
44	Hydrogen ground-state binding energy	The BFUT atomic construction gives the hydrogen ground-state binding energy.	P16; P25
45	Atomic stability	The finite condensation structure and substrate density are connected to the persistence of atomic structure.	P25
46	Molecular and chemical stability	P25 derives sensitivity of atomic and molecular structure to the substrate density, including a density threshold associated with disruption of chemical bonding.	P25
47	Electron reference length	The electron reference length is an independently meaningful electromagnetic length scale used in the BFUT particle-sector construction and connected to the substrate-derived particle parameters.	P19; P78
48	Reduced Planck constant	The reduced Planck constant is derived from proton mass, proton charge radius, c, and the condensation minimum R_0: ħ_vss = m_p c $r_p/(\pi R_0)$.	P16; P27
49	Planck constant	Planck's constant follows as h_vss = 2πħ_vss and supplies the action quantum used in BFUT quantum relations.	P16; P27
50	Minimum circulation quantum	The minimum angular-momentum scale ħ_vss/2 is connected to the 720° restoration topology of the matter condensation.	P19A; P27
51	Compton wavelength	The Compton wavelength is expressed using the BFUT action scale and particle parameters.	P27
52	de Broglie wavelength	The de Broglie wavelength is expressed using the BFUT action scale and particle momentum.	P27
53	Harmonic-oscillator energy levels	The harmonic-oscillator spectrum is expressed using the ħ_vss and the corresponding quantum action scale.	P27
54	Planck length	The Planck length is derived from ħ_vss together with G and c.	P27
55	Planck mass	The Planck mass is derived from ħ_vss together with G and c.	P27
56	Planck time	The Planck time is derived from ħ_vss together with G and c.	P27
57	Vacuum energy density	The equilibrium substrate rest-energy density is u_vac = $\rho_s c^2$.	P25; P27
58	Schrödinger equation	The time-dependent Schrödinger equation is derived as the non-relativistic limit of the covariant substrate carrier equation.	P19A; P27

SN	Application / Derived Result	Physical result or BFUT application	BFUT source
59	Born rule	The Born probability $P(x)=\|\psi(x)\|^2$ is given a physical substrate interpretation through deformation-energy density and measurement interaction.	P19A
60	Heisenberg uncertainty principle	The uncertainty scale is connected to the finite localisation and action scale of substrate condensations.	P19A; P27
61	Half-integer spin	Half-integer spin is derived from the 720° restoration topology of the matter condensation.	P19A; P27
62	Spin-statistics relation	The distinction between embedded matter condensations and propagating substrate disturbances supplies the BFUT physical interpretation of fermionic and bosonic statistics.	P19A; P27
63	Pauli exclusion principle	Pauli exclusion is explained through the impossibility of identical fermionic condensations occupying one complete circulation state.	P19A; P27
64	Fermionic mass hierarchy	Fermionic mass structure is connected to organised circulation within the condensation architecture.	P19A
65	Gauge symmetry	U(1), SU(2), and SU(3) gauge structures are interpreted through local circulation invariance of substrate condensations.	P19A
66	Quantum superposition	Superposition is given a physical substrate interpretation as distributed organised excitation before interaction resolves the state.	P19A
67	Wave-function collapse	Wave-function collapse is interpreted as physical state resolution produced by interaction with matter in the substrate.	P19A
68	Entanglement	Entanglement is interpreted through shared coherent substrate structure and correlated physical states.	P19A
69	Quantum tunnelling	Tunnelling is represented through substrate condensation-boundary penetration, with the penetration scale determined by the BFUT action and barrier parameters.	P19A; P27
70	Decoherence	Decoherence is interpreted as loss of coherent substrate organisation through environmental interaction.	P19A
71	Quantum measurement	Measurement is treated as physical interaction between a quantum excitation and detector matter, providing the mechanism for state resolution.	P19A
72	Quantum gravity unification	Quantum behaviour and gravitation are placed within one substrate framework through the common carrier field and physical substrate.	P18; P19A
73	Quantum gate evolution	Quantum-gate unitary evolution is expressed using the BFUT-derived action scale, linking phase accumulation to substrate action.	P24; P27
74	Quantum-gate minimum time	The minimum controlled gate time is connected to the BFUT action scale and control-field energy.	P24; P27
75	Quantum-computing substrate memory	The P24 substrate-memory timescale is connected to the same substrate density that fixes the BFUT action scale.	P24; P27
76	Bell correlation	The Bell correlation function is connected to the Born rule and BFUT spin topology in the quantum-computing treatment.	P24
77	CHSH quantum bound	The BFUT quantum-computing treatment incorporates the quantum CHSH bound within its substrate interpretation of quantum correlations.	P24
78	Time as accumulated substrate evolution	Time is defined as accumulated evolution of physical states in the Spaticle substrate.	P22
79	Special-relativistic time dilation	Kinematic time dilation is derived from the finite propagation budget shared between spatial motion and internal evolution.	P22
80	Gravitational time dilation	Gravitational time dilation is derived from reduced local substrate propagation efficiency caused by gravitational deformation.	P22
81	Unified time-dilation relation	Kinematic and gravitational effects are combined through the common propagation-budget framework.	P22
82	Length contraction	Length contraction is derived as a second consequence of the same propagation-budget constraint.	P22
83	Twin paradox	The twin paradox is resolved through the different substrate propagation histories of the two clocks.	P22
84	Clock universality	All physical clocks slow by the same factor because physical clocks are substrate processes subject to the same propagation budget.	P22
85	Photon proper time	A photon assigns its full propagation budget to spatial propagation, giving zero proper time in the BFUT formulation.	P22; P23
86	Arrow of time	The direction of time is linked to irreversible outward substrate propagation and accumulated state change.	P22
87	Simultaneity and causality	Finite substrate propagation speed supplies the physical basis for causal ordering and simultaneity relations.	P22; P23
88	Past and future asymmetry	The substrate evolution framework provides a physical account of the distinction between completed and not-yet-completed state evolution.	P22
89	Quantum time evolution	Quantum time evolution is placed within the same physical substrate evolution that defines time macroscopically.	P22; P19A
90	Equivalence principles	The weak, Einstein, and strong equivalence principles are examined within the BFUT substrate framework.	P22
91	Temporal singularity limit	Finite substrate propagation capacity supplies a temporal argument	P22; P26

SN	Application / Derived Result	Physical result or BFUT application	BFUT source
		against physically reaching an infinite-density singularity.	
92	Universal speed limit	c is identified as the maximum rate at which the Spaticle substrate can reorganise and propagate a disturbance.	P23
93	Speed of light from substrate stiffness and density	The propagation speed is derived as $c\_vss = \sqrt{(K\_s/\rho_s)}$.	P23
94	Independent reconstruction of c	The speed of light is reconstructed as c_vss, as a consistency relation of the ħ identity, from e, R_0, ε_0, m_p, r_p, and α_vss.	P19; P23; P27
95	Massive-particle velocity deficit	A massive condensation devotes part of its physical energy budget to internal structure, leaving less capacity for spatial propagation.	P23
96	Equality of light and gravitational-wave speeds	Light and gravitational waves are disturbances of the same substrate and therefore share the same limiting propagation speed.	P23
97	Singularity impossibility	Finite substrate density and restoring dynamics prevent physical infinite density.	P26
98	Finite-density causal bound	The causal bound $\bar{\rho}\_max = 3c^6/(4\pi G^3M^2)$ gives a finite mean-density limit for compact collapse.	P26
99	Finite gravitational compression	The substrate restoring mechanisms oppose unlimited gravitational compression.	P26; P28
100	Black holes as finite gravitational vortices	Black holes are represented as finite-density gravitational vortex structures without a physical infinite-density singularity.	P6; P26; P28
101	Black-hole finite core and surrounding structure	The BFUT black-hole model specifies a finite compressed core together with surrounding redistribution, coherence, and entrainment regions.	P28
102	Black-hole redistribution and entrainment	Organised deformation is redistributed from the compressed core into the surrounding shell and deformation domain.	P28
103	Black-hole deformation domain	The finite deformation-domain relation defines the outer extent of organised substrate deformation around a compact mass.	P18; P26; P28
104	Rotational sustenance of gravitational structure	Sustained rotation is treated as the dynamical condition supporting organised gravitational-vortex structure and continued compression.	P26; P28
105	Black-hole seed dissipation	The substrate relaxation framework supplies a characteristic dissipation timescale for transient deformation.	P26
106	Hawking-radiation interpretation	Within the finite-substrate black-hole structure, BFUT argues that Hawking radiation has no physical realisation.	P28

Appendix B. Mathematical and Non-Mathematical Predictions

The Big Flare-Up Theory (BFUT) calls the matter substrate the Spaticle Field. The equilibrium density is $\rho_s = 7.3 \times 10^{-27}$ kg/m³.

1. Mathematical Predictions

No.	Mathematical prediction	Equation / quantitative result	Source
1	Condensation minimum	$E(R)=A/R^2+BR^2+CR+D/R$; $R_0=1.27348221$	P16
2	Void-filling asymmetry	$\delta_d=2\delta_u$ from the three-sphere geometry	P16
3	Void correction	$A_{void}/6$ as the geometric void correction	P16
4	Electron/proton mass ratio	$m_{e\_vss}=m_p/(6\pi^5)$	P19
5	Reduced Planck constant	$\hbar_{vss}=m_p c r_p/(\pi R_0)$, with $h_{vss}=2\pi\hbar_{vss}$	P16/P19
6	Fine-structure constant	$\alpha_{vss}=e^2/(4\pi\varepsilon_0\hbar_{vss}\, c)$ within the BFUT derivation chain	P19
7	R_0 cross-check	$R_0=4\varepsilon_0 m_p c^2 r_p \alpha_{vss}/e^2$	P19; internal consistency
8	Independent c reconstruction	$c_{vss}^2=e^2R_0/(4\varepsilon_0 m_p r_p \alpha_{vss})$	P23/P19
9	Substrate stiffness	$K_s=\rho_s c^2$	P23
10	Universal acceleration scale	$a_s=c\sqrt{G\rho_s/3}$	P18/P78
11	Finite deformation-domain radius	$R_d=[3M/(8\pi\rho_s)]^{(1/3)}$	P18
12	Rotationally enlarged domain	$R_{eff}=R_d(1+v_{rot}^2/c^2)^{(1/3)}$	P18
13	DME rotation law	$v^2=v_b^2[1+a_sR/v_b^2]^{(1/2)}$	P18/P25/P78
14	Deep-regime baryonic Tully-Fisher law	$v^4\approx GMa_s$	DME low-acceleration limit
15	Mass-velocity scaling	$v\propto M^{(1/4)}$ in the deep DME regime at fixed ρ_s	Derived from P18 DME
16	Fixed BTFR coefficient	$v/M^{(1/4)}=[G\, c\sqrt{G\rho_s/3}]^{(1/4)}$	Derived from P18
17	DME transition radius	$R_t=\sqrt{GM/a_s}$ when $a_sR/v_b^2=1$	Derived from P18 DME
18	DME acceleration asymptotes	$g_{DME}=\sqrt{g_b(g_b+a_s)}$; high-g: $g\approx g_b+a_s/2$; low-g: $g\approx\sqrt{a_s g_b}$	Derived from P18
19	Domain mass scaling	$R_d\propto M^{(1/3)}$ at fixed ρ_s	Derived from P18 DDR
20	DDR mean-density relation	Mean density inside R_d is $2\rho_s$	Derived from P18 DDR
21	DDR boundary acceleration	$g_d=GM/R_d^2=GM^{(1/3)}(8\pi\rho_s/3)^{(2/3)}$	Derived from P18 DDR
22	Equilibrium carrier relaxation scale	$L_{nat}=\lambda_u/\sqrt{3\rho_s}=45.17$ AU; $\tau_{nat}=L_{nat}/c=6.26$ h	P18 with current ρ_s
23	Carrier inverse length	$\mu_s^2=3G\rho_s/c^2$	P18
24	Cross-scale carrier identity	$a_sL_s=c^2/3$, where $L_s=1/\mu_s$	Derived from P18
25	Spatial carrier attenuation	$g/g_N=e^{(-r/R_{eff})}(1+r/R_{eff})$ for the settled exponential carrier component	P18 displayed potential
26	Newtonian-limit correction	$(g-g_N)/g_N\approx-\frac{1}{2}(r/R_{eff})^2$ for $r\ll R_{eff}$	Derived from P18 potential
27	Asymptotic attenuation slope	$d\ln(g/g_N)/dr\rightarrow-1/R_{eff}$ for $r\gg R_{eff}$	Derived from P18 potential
28	Carrier-component rotation profile	$v^2=(GM/r)e^{(-r/R_{eff})}(1+r/R_{eff})$	Derived from P18 potential; carrier component only
29	Photon coherence threshold	$E_{min}=2.25$ meV	P23
30	Photon persistence above threshold	$L_{persist}=L_{rlx}(E/E_{min})^2$	P23
31	Photon persistence below threshold	$L_{persist}=L_{rlx}(E/E_{min})^4$	P23
32	Photon log-slope prediction	$d\ln L_{persist}/d\ln E=2$ above E_{min} and 4 below E_{min}	Derived from P23
33	Finite causal mean-density bound	$\bar{\rho}_{max}=3c^6/(4\pi G^3M^2)$	P26
34	Causal limiting radius	$R_{max}=GM/c^2$	P26
35	Universal compactness relation	$R_{max}/M=G/c^2$	Derived from P26
36	Compact-object area scaling	$A\propto M^{(2/3)}$, hence BFUT organised-deformation entropy scaling $S\propto M^{(2/3)}$	P26
37	Vacuum energy density	$u_{vac}=\rho_s c^2$	P2/P14/P23
38	H-class radial resonance mass	$\lambda_{H\_vss}=2AR_0/\pi^2$; $v_{vss}=6E_{unit}/\alpha_{vss}$; $m_{H\_vss}=v_{vss}\sqrt{2\lambda_{H\_vss}}=124.75$ GeV/c²	P19
39	Strong-coupling geometric relation	$\alpha_{s\_vss}\propto BR_0^4/A$	P19
40	Electromagnetic geometric invariant	$\omega_c^2R_0^2/c^2$	P19
41	Periastron residual statistic	$R_{peri}=\Sigma$(peri-window power)/Σ(off-peri power)	P18 test formulation
42	Pulsar phase-window statistic	$T_{PSR}=\Sigma W_p R_i/\sqrt{\Sigma W_p^2\sigma_i^2}$	P18 test formulation
43	S8 rotational suppression	Proof-of-concept rotational collapse gives S8=0.7805 versus 0.832 radial, a 6.2% deficit	P13
44	Neutral Z resonance	$m_{Z\_vss}=\pi^4 m_p=91.396$ GeV/c²	P19
45	Charged W resonance	$m_{W\_vss}=256M=80.066$ GeV/c²	P19
46	Electroweak mixing output	$\sin^2\theta_{W\_vss}=1-(m_{W\_vss}/m_{Z\_vss})^2=0.23257$	P19
47	Shankar configuration resonance	$m_{Shankar}\, c^2 = [E(2+2) - E(3+1)]E_{unit} = 2.60E_{unit} = 776.5$ MeV	P16A
48	BFUT configuration resonance	$m_{BFUT}\, c^2 = [E(4+0) - E(3+1)]E_{unit} = 4.70E_{unit} = 1403.7$ MeV	P16A

2. Non-Mathematical Predictions

No.	Non-mathematical prediction	Expected observational or physical consequence	Source
1	Universal Centrality Rule	Every settled galaxy should possess a primary black hole or dominant gravitational vortex at its dynamical centre. A settled	P6/P28

No.	Non-mathematical prediction	Expected observational or physical consequence	Source
		galaxy lacking the primary central object would falsify the hypothesis.	
2	Rotational entrainment saturation	DDR enhancement should saturate with galaxy or cluster rotation.	P26
3	Large-system enhancement floor	Large coherent systems should retain a non-zero enhancement floor, approximately 14–20% in the P26 analysis.	P26
4	Low-baryonic-support enhancement	Low-baryonic-support systems should show substantially larger Spaticle field enhancement, reaching about 50–60% in the P26 sample.	P26
5	Cluster-versus-field differential floor	Mass-matched galaxies embedded in rich clusters should show a higher enhancement floor than comparable isolated field galaxies if nested-domain reinforcement operates.	P26
6	Rotational sustenance threshold	Compact seed cores formed through collapse or explosive release should persist only when surrounding matter provides sufficient rotational coherence.	P26
7	Isolated seed dissipation		P26
8	Antihydrogen gravitational behaviour	Antihydrogen should fall under gravity identically to ordinary hydrogen.	P16A
9	Stable antimatter-domain prediction	Ordinary formation conditions should not produce macroscopic stable antimatter domains.	P16A
10	Complete matter-antimatter cancellation	Matter and antimatter configurations should annihilate through cancellation of the opposing substrate topologies.	P16/P16A
11	Maintained CMB equilibrium	The CMB should be continuously maintained as a thermal-equilibrium radiation field, not require a relic origin from a finite-age event.	P7
12	Cosmic redshift without substrate expansion	Cosmic redshift should be explainable through source-observer dynamics and photon propagation through a static substrate.	P1/P23
13	Observer-bulk-flow signature	Apparent cosmic acceleration should correlate with observer motion and directional sampling effects without requiring a separate dark-energy component.	P4
14	Lyman-alpha interpretation	The rise in Gunn-Peterson/Lyman-alpha opacity should admit a substrate absorption/percolation interpretation without uniquely requiring an expanding-universe interpretation.	P11
15	ISW interpretation	Observed ISW temperature correlations should admit local Spaticle field temperature variations as a physical contribution.	P12
16	S8 redshift trend	Rotational suppression should be stronger at low redshift and diminish toward high redshift in the P13 proof-of-concept framework.	P13
17	S8 analysis sensitivity	Recovered S8 should vary materially under defensible choices of scale cuts, tomography, covariance, intrinsic-alignment model, and sky coverage, even for the same underlying synthetic shear field.	P13
18	Finite-core compact objects	Compact objects should possess finite organised compression cores, with the macroscopic mapping testable by future observations.	P26/P28
19	No physical singularity	Observations of compact objects should not require a physically realised infinite-density singularity.	P6/P26
20	Information retained in compact objects	BFUT compact-object dynamics should retain information in organised substrate deformation and permit outward carrier relaxation.	P26/P28
21	No separate dark-matter particle requirement	Galaxy and lensing anomalies should be reproducible through organised Spaticle field deformation without introducing a dark-matter particle.	P18/P25/ P78
22	Merger-morphology test	In interacting systems, substrate-associated gravitational effects should track the organised motion of the dominant galactic matter and respond to redistribution during the merger.	P78
23	Low-dark-matter galaxy behaviour	Systems such as DF2, DF4 and FCC224 should remain compatible with the stellar-mass-dominated line under the BFUT interpretation.	P78
24	Cosmic-scale continuity	The same Spaticle field should support a continuous hierarchy from microscopic condensations through galactic and cosmological structures.	P14/P16/ P18

Appendix C. Mathematical and Non-Mathematical Resolutions of ΛCDM Tensions

The Big Flare-Up Theory (BFUT) calls the matter substrate the Spaticle Field. The equilibrium density is $\rho_s = 7.3 \times 10^{-27}$ kg/m³.

1. Mathematical Resolutions of ΛCDM Tensions

No.	Tension	BFUT mathematical treatment	Source
1	Cosmological constant problem	$u_{vac}=\rho_s c^2$, with empty substrate modes contributing no physical	P2

No.	Tension	BFUT mathematical treatment	Source
		condensation energy.	
2	QFT vacuum-energy discrepancy	One physical substrate replaces the multiple independent vacuum-field contributions used in the conventional sum, while unexcited modes carry no condensation energy.	P2
3	Seeliger paradox / divergent summed gravity	$g\_total=\Sigma\_i\ g\_i\ \exp(-r/R_{d}omain,i)$, giving finite contributions from finite deformation domains.	P18
4	Infinite gravitational range	$R_d=[3M/(8\pi\rho_s)]^{(1/3)}$ gives every source a finite deformation domain.	P18
5	Galaxy missing gravity	DME introduces the substrate-derived acceleration scale $a_s=c\sqrt{(G\rho_s/3)}$.	P18/P25/P78
6	Deep-galaxy mass-velocity relation	$v^4\approx GMa_s$ follows from the low-acceleration DME limit.	P18/P25/P78
7	Weak-lensing excess	The same DME and substrate scale are applied to the KiDS-1000 stacked lensing data.	P25/P78
8	Dark-matter particle requirement	The additional gravitational response is represented by substrate deformation and entrainment, with no dark-matter particle parameter.	P18/P25/P78
9	Proton-electron hierarchy	$m\_e\_vss=m_p/(6\pi^5)$ provides a geometric mass relation.	P19
10	Planck-constant origin	$\hbar\_vss=m_p c r_p/(\pi R_0)$ connects the BFUT-derived $\hbar\_vss$ to the condensation geometry.	P16/P19
11	Fine-structure constant	α_vss is linked to the BFUT condensation and $\hbar\_vss$ derivation chain.	P19
12	Strong-coupling geometric scale	α_s_vss is related to condensation geometry through $\alpha_s\_vss\propto BR_0^4/A$.	P19
13	Universal speed-limit origin	$c\_vss=\sqrt{(K_s/\rho_s)}$, with $K_s=\rho_s c\_vss^2$, identifies c_vss with the substrate reorganisation limit.	P23
14	GW/photon speed equality	Both are substrate disturbances and share the same maximum propagation rate c.	P22/P23
15	Relativistic time-dilation structure	$c^2=v\_internal^2+v\_grav^2+v\_spatial^2$ and $\eta=d\tau/dt= c\_s/c_0$ provide a common propagation-budget description.	P22
16	Singularity divergence	The causal limit gives finite $R\_max=GM/c^2$ and $\bar{\rho}\_max=3c^6/(4\pi G^3M^2)$, while the condensation functional excludes zero-radius condensation.	P16/P26
17	Quantum/classical regime connection	The carrier-field formulation supplies a common substrate description whose settled limits reproduce the classical gravitational regime.	P18
18	S8 tension	Rotational-collapse suppression gives a 6.2% S8 deficit in the P13 proof-of-concept simulation.	P13
19	Hubble tension	BFUT replaces a single universal expansion interpretation with gravitational sorting and observer-dependent sampling; P1 reports r=0.675 for the sorting model.	P1/P14
20	Early-structure timing problem	An eternal substrate removes the finite-age formation constraint used in a finite-origin cosmology.	P8/P14
21	Horizon problem	An infinite, eternal substrate removes the requirement that all observed regions were once in causal contact after a finite beginning.	P5/P14
22	Flatness problem	Spatial infinitude removes the finite-origin curvature-dilution requirement associated with inflation.	P5/P14
23	CMB temperature origin	$T=(u\_CMB\ c/(4\sigma))^{(1/4)}$ gives 2.725 K from the measured CMB energy density.	P7
24	Cosmological acceleration / dark-energy interpretation	Observer bulk flow and gravitational sorting supply a mathematical route to apparent acceleration without a separate dark-energy term.	P4
25	Lyman-alpha opacity rise		P11
26	ISW anomaly interpretation	Local Spaticle field temperature variations supply a mathematical contribution to the observed ISW signal.	P12
27	Galaxy-scale lensing and rotation consistency	The same a_s and substrate framework are used across SPARC rotation curves and KiDS-1000 lensing.	P25/P78
28	Finite-range correction to Newtonian gravity	The exponential carrier solution gives $g/g\_N=e^{(-x)}(1+x)$, with $x=r/R\_eff$, and approaches Newtonian gravity as $x\to 0$.	P18

2. Non-Mathematical Resolutions of ΛCDM Tensions

No.	Tension	BFUT non-mathematical treatment	Source
1	Dark matter as a particle	BFUT interprets the additional gravitational effect as organised substrate deformation and entrainment. The question becomes a gravitational-response problem, not a requirement for a new particle.	P18/P25/P78
2	Dark-energy requirement	BFUT interprets apparent acceleration through observer bulk flow and gravitational sorting, without introducing a separate dark-energy component.	P4/P14
3	Hubble tension	The observed Hubble relation is treated as an emergent statistical property of gravitationally sorted matter. Different sampled populations can produce different inferred slopes.	P1/P14
4	Horizon problem	An infinite and eternal substrate does not require a finite-origin epoch in which distant regions were brought into causal contact.	P5/P8
5	Flatness problem	Spatial infinitude removes the need for inflationary curvature dilution to explain a globally near-flat observable geometry.	P5
6	Early galaxy formation timing	Structure can develop in an eternal universe with no fixed finite age measured from a Big Bang origin.	P8

No.	Tension	BFUT non-mathematical treatment	Source
7	CMB relic interpretation	The CMB is treated as dynamically maintained thermal equilibrium radiation continuously supplied by stellar processes.	P7
8	Lithium problem	Steady-state nucleosynthesis in an ongoing stellar-processing universe supplies an alternative account of primordial lithium abundance.	P3
9	S8 tension	Rotational support during structure formation reduces inferred clustering amplitude, while the lensing inference pipeline itself is shown to be model-sensitive.	P13
10	Low-redshift versus CMB growth mismatch	BFUT attributes the low-redshift suppression pattern to rotational structure dynamics and questions whether a single ΛCDM growth history is the unique interpretation.	P13
11	S8 methodological sensitivity	The P13 simulations show that defensible analysis choices can shift or broaden recovered S8 while holding the underlying synthetic shear field fixed.	P13
12	Weak-lensing excess	BFUT uses the same substrate-derived gravitational response that fits galaxy dynamics to interpret weak-lensing observations.	P25/P78
13	Ultra-diffuse and low-dark-matter galaxies	These systems are treated as tests of the substrate-response model, including cases where the observed dynamics are close to the stellar component alone.	P25/P78
14	Merger mass-distribution interpretation	Merger morphology is interpreted through redistribution and entrainment of substrate-associated gravitational response, allowing lensing and visible matter to be compared directly during interaction.	P78
15	Cosmic redshift interpretation	Redshift is treated as a Doppler/gravitational-sorting effect through a static substrate, so photon propagation does not require stretching of the substrate itself.	P1/P23
16	CMB and large-scale structure as separate relic epochs	BFUT places them in one continuously existing substrate, with the CMB maintained dynamically and large-scale structures forming within the same persistent environment.	P7/P8
17	Black-hole singularity problem	BFUT retains the observed compact-object phenomena while interpreting the interior as finite organised substrate compression.	P6/P26/P28
18	Black-hole information problem	The finite-core, permeable-boundary picture provides a route for information to remain encoded in substrate deformation and to relax outward.	P26/P28
19	Hawking-radiation mechanism	BFUT does not use the standard singularity-plus-event-horizon pair-creation mechanism; it substitutes finite carrier relaxation emission from the compressed substrate.	P26/P28
20	Need for inflation as the unique early-universe solution	BFUT's infinite, eternal substrate provides alternative explanations for horizon, flatness and early-structure timing without an inflationary origin event.	P5/P8
21	Universal expansion as the only interpretation of cosmic acceleration	BFUT treats directional observer motion and gravitational sorting as physical alternatives that can generate apparent acceleration.	P4
22	Unique ΛCDM interpretation of low-redshift observables	BFUT argues that SZ, weak lensing, redshift-space distortions, ISW and related observables can have substrate-based interpretations that do not depend on one universal ΛCDM growth narrative.	P10/P12/P13